Cryosphere Monitoring from Satellites and Aircrafts

Nilsson, Johan

Publication date:
2015

Document Version
Publisher's PDF, also known as Version of record

Cryosphere Monitoring from Satellites and Aircrafts

Johan Nilsson
Ph.D Dissertation
January 15, 2015

DTU Space
National Space Institute

Cryosphere Monitoring from Satellites and Aircrafts

Johan Nilsson
DTU Space, National Space Institute, Technical University of Denmark
Ph.D Dissertation, Kgs. Lyngby, January 15, 2015

Supervised by René Forsberg, DTU Space, National Space Institute, Technical University of Denmark,
Louise Sandberg Sørensen, DTU Space, National Space Institute, Technical University of Denmark,

http://www.space.dtu.dk

Dansk resumé

Kryosfæren er en fællesbetegnelse for alle de komponenter der indeholder frosne vand på Jordens overflade. Disse komponenter er meget følsomme over for ændringer i luftens temperatur og nedbør, og derved over for klimaændringerne. De vigtigste komponenter i kryosfæren er indlandsisen, iskapper og gletschere. Den Grønlandske og Antarktiske iskappe står alene for i alt 77 % af verdens ferskvand i frossen tilstand, og har kapacitet til at øge det globale havniveau med 6 og 65 m henholdsvis. Forståelse af iskappernes respons på klimaændringerne er af afgørende betydning at få indsigt i disse systemers mekanismer, og hvordan de påvirker det globale havniveau.

Satellit højdemåling har i de sidste to årtier været anvendt til at overvåge ændringer i verdens iskapper, har vist muligheden for bestemmelse af iskappernes massebalance. I de senere år er denne mulighed blevet udvidet til iskapper og gletschere ved hjælp af både satellit- og luftbåren altimetri vist i studier.

Forskningens emnet for denne Ph.D. afhandling er at undersøge nuværende højdeændringer af de isdækkede jordområder i Arktis og det nordatlantiske område ved brug af forskellige telemålings datasæt, såsom ICESat og CryoSat-2, med særlig fokus på CryoSat-2 mission. En central del af Ph.D.-studiet er udviklingen af software og algoritmer til udnyttelse af CryoSat-2 data over komplekst isdækket terræn. Undersøgelserne har omfattet både udvikling af praktiske metoder til databehandling af ESA niveau-1 produkt (L1b) til vurdering af overfladehøjder og højdeændringer over komplekst isdækket terræn.

De beregnede overfladehøjder og højdeændringer er fuldt valideret ved sammenligning med resultater fra igangværende luftbårne laser-altimetri kampagner over flere forskellige typer af isdækkede områder i den arktiske region. Resultaterne fra denne validering er også sammenholdt med resultater der stammer fra ESA L2 baseline-B produktet for at bedømme kvaliteten af begge produkter. Fra denne indbyrdes sammenligning viste det sig, at den nye databehandlingsprocedure der er udviklet i denne afhandling, klare sig bedre end den nuværende ESA L2 baseline-B behandlingsprocedurer. De procedurer der er udviklet i denne afhandling for CryoSat-2 LRM og SARin-mode viste i gennemsnitlig forbedringer i både nøjagtighed og præcision på henholdsvis 50% og 30%, sammenlignet med den nuværende ESA L2 baseline-B produkt.

Udviklingen af de nye procedurer til bestemmelse af overfladeændringer har givet en hidtil uset dækning af Grønlands indlandsis, en dækning bestående af mere end 17 millioner observationer af overfladehøjder og højdeændringer. De estimerede højdeændringer, valideret ved hjælp af luftbårne laser-altimetri

højdeændringer, viste en korrelation på mere end 0,9. De anslåede højdeændringer, anvendt til at bestemme den samlede volumen ændring af Grønlands indlandsis, resultere i et skøn på -224±25 km^3a^{-1} hvilket er i god overensstemmelse med andre studier. Dette beviser, at med øget databehandling af CryoSat-2 data, kan dataene bruges til både store og små skala masse balance undersøgelser af indlandsisen, iskapper og gletschere. Slutteligt, det arbejde der er skitseret i denne Ph.D. afhandling giver mange muligheder for at forbedre det nuværende ESA L2 produktet til den videnskabelige bruger.

Abstract

The cryosphere is collective term for all the components containing frozen water on the Earth's surface. These components are highly sensitive to changes in the air temperature and precipitation, and hence to climate change. The major components of frozen water in the cryosphere are the ice sheet, ice caps and glaciers. The Greenland and Antarctic ice sheets alone store a total of 77% of the worlds freshwater in a frozen state, and has the capabilities of increasing the global sea-level with 6 and 65 m respectively. Understanding the changes of the ice sheets in response to climate change is of vital importance to gain insight into the behaviour of these systems and how they affect the global sea level.

Satellite altimetry has for the last two decades been used to monitor the changes of the worlds ice sheets, allowing for the determination of their mass balance. In recent years this has been expanded to both ice caps and glaciers using satellite and airborne altimetry.

The research topic of this Ph.D thesis has been to determine and improve the estimation of present-day elevation changes of the ice covered land regions in the Arctic and the North Atlantic by the use of satellite altimetry, such as the ICESat and CryoSat-2 missions, with a specific focus on Cryosat-2. An central part of the Ph.D study has gone into developing software and algorithms for the utilization of CryoSat-2 data. The investigations has included both development of practical methods for data processing of the ESA level-1 product (L1b) for the estimation of surface elevations and elevation changes over both smooth and complex glacial terrain.

The retrieved surface elevations and elevation changes have been fully validated by comparison with airborne results from ongoing airborne laser campaigns over several types of glacial terrain in the Arctic region. The results from this validation study was then inter-compared with results derived from the ESA L2 baseline-B product to judge the quality of both products. From this inter-comparison it was shown that the new processing chains, developed in this thesis, performed better than the current ESA L2 baseline-B processing setup. The processing chains developed in this thesis for the CryoSat-2 LRM and SARin-mode showed and average improvement in both accuracy and precision of 50% and 30% respectively, compared to the current ESA L2 baseline-B product.

The development of new surface elevation change algorithms have provided unprecedented coverage of the Greenland Ice Sheet, consisting of more than 17

million surface elevations and elevation change observations. The estimated elevation changes where validated using airborne laser derived elevation changes which showed a correlation of higher than 0.9. The estimated elevation changes where used to determine the total volume change of the Greenland Ice Sheet, producing an estimate of -224±25 km^3a^{-1} for the period of 2010-2014, which is in good agreement with other studies. This effectively proves that with enhanced processing the CryoSat-2 mission can be used for both large and small scale mass balance studies of ice sheets, ice caps and glaciers. In the end, the work outlined in this thesis provides many possibilities for improving the current ESA L2 product available to the scientific user.

Preface

This thesis is submitted in fulfilment of the requirements for obtaining a Ph.D. degree at DTU Space, National Space Institute, Technical University of Denmark. The research presented here was carried out within the Division of Geodynamics, DTU Space, under supervision of Prof. René Forsberg and Dr. Louise Sandberg Sørensen. The Ph.D. program was partly funded by the Stability and Variations of Arctic Land Ice (SVALI) under the Top-level Research Initiative. This thesis includes two scientific papers detailed in Section 2; (Nilsson et al., 2015b) and (Nilsson et al., 2015a)

I started my Ph.D in Dec. 2011 as part of the SVALI-project. The main goal of the thesis have been to improve the understanding of the current and future melt-rates of land-based ice in the Arctic and North-Atlantic region. The SVALI-project aims to asses and quantify the consequence of decreasing land ice volume on sea level and ocean circulation, to determine the impact on society due current and future glacier variations.

During my Ph.D I have had the opportunity to participated in many conferences and meetings, such as AGU, EGU and NIGS. I have also had the opportunity to take several course and workshops in both Denmark and in Svalbard. I also spent four months at the Geological Survey of Canada (GSC) in Canada, as a part of my external research stay, under the supervisions of Dr. David Burgess and Dr. Laurence Gray. At the GSC I got first hand experience with CryoSat-2 level-1b data processing. I further had the pleasure of doing fieldwork, as a part of the 2012 CryoVEx campaign, for a duration of one week.

The main part of the work presented here in this thesis consist of the development of a new processing chains for the CryoSat-2 mission for the determination of accurate and robust surface elevations over glacial terrain. These have then been used to derive surface elevation changes for the Greenland Ice Sheet for estimation of the volume change between 2010-2014. The paper (Nilsson et al., 2015a) further details the effort made of determining the volume and mass change of the main ice caps and glaciers in the Arctic and North-Atlantic region. The paper (Nilsson et al., 2015b) details the effect of the Greenland 2012 melt event on effect radar altimetry observations.

Johan Nilsson
Kgs. Lyngby, January 2015

Acknowledgement

I am deeply grateful for the people that have been involved in my life during my Ph.D, both family and colleagues. I would first of all like to thank my family for standing by me during my many years in higher education, first as student then as a Ph.D, without their support I would never be where I am today. I would further like to thank my supervisors René Forsberg and Louise Sandberg Sørensen for allowing me this opportunity, and for letting me travel to many amazing places like Greenland and Svalbard during my Ph.D. Their guidance and encouragement have been vital for me to do this work. Special thanks goes to Louise for putting in considerable time and effort in the makings of my articles and to Sebastian for lending me his software and the great altimetry discussions.

Many thanks goes out to David Burgess, Laurence Gray and Luke Copeland for making my external research stay at the Geological Survey of Canada and University of Ottawa a great social and working experience. I enjoyed both the social life and the very fruitful discussion with both Dave and Laurence about CryoSat-2 processing. Without Laurence great patience and help the work done in this thesis would never have happened. I also enjoyed the flights that Luke invited and took me on during my time there. Finally a big thank you to all my Canadian Ph.D-colleges and room-mates (Fiona, Nicole, Wez, Adrienne, Laura and Tyler) for making my time there amazing. I would also like to thank all my friend that I have gained during my time here at DTU-Space and other places; Ole, Jan, Babis, Christian, Jens, Joanna, Tibor, Ioana, Maulik, Peter, Anders and to all my friends and colleagues in the SVALI-project who made every conference a great pleasure.

List of Figures

List of Tables

Contents

1 Introduction

The cryosphere is the collective term for all the components containing frozen water on the Earth's surface. These components are highly sensitive to changes in the air temperature and precipitation, and hence to climate change. The major components of frozen water in the cryosphere are the ice sheets, ice caps and glaciers. The Greenland and Antarctic ice sheets alone store a total of 77% of the worlds freshwater in a frozen state, and has the capabilities of increasing the global sea-level with 6 and 65 m respectively (Bamber and Payne, 2004), if they are completely melted.

The most recent assessments from the Intergovernmental Panel on Climate Change (Vaughan et al., 2013) state that the mass loss from ice sheets and glaciers are a major contributor to the current and future sea-level rise. The rise in global sea-levels has significant and long-lasting impact on the Earth's physical, biological and social systems. The cryosphere is a natural climate change indicator where changes in the major components, such as the ice sheets, are a results of the integrated response to a changing climate. Understanding the changes of these systems are therefore of vital importance to gain insight into the their past, present and future changes.

Satellite altimetry has for the last two decades been used to monitor the changes of the worlds ice sheets, pioneered by studies such as (Zwally et al., 1987), (Wingham et al., 1998) and others, allowing for the determination of the their mass balance. In recent years these methods have been expanded further to ice caps and glaciers, using both satellite and airborne altimetry in studies such as (Abdalati et al., 2004; Arendt et al., 2002; Gardner et al., 2013; Moholdt et al., 2010, 2012).

The mass balance of ice sheets, ice cap and glaciers can be determined using satellite altimetry by measuring the temporal changes of the topography. The change in topography or surface elevation can then be converted into volume and finally mass change. Therefore, the determination of the mass balance is heavily dependent on the quality of the measured surface elevations. Hence, the accuracy of altimeter derived surface elevations is an importance factor in the determination of the ice sheets contribution to current global sea level rise

The research topic of this Ph.D thesis has been to determine and improve the estimation of present-day elevation changes of the ice covered land regions in the Arctic and the North Atlantic by the use of satellite altimetry, such as the ICESat and CryoSat-2 missions, with a specific focus on Cryosat-2.

CryoSat-2 was launched in 2010 and carries a novel Ku-band (13.6 GHz) radar interferometric altimeter system (SIRAL) especially designed for land and sea ice monitoring. However, due to its novelty, there are still large challenges associated with obtaining useful results from the mission, especially over the marginal zones of the ice sheets and the high sloping areas of ice caps and glaciers. Therefore, a central part of the Ph.D study focused on developing software and algorithms for the utilization of CryoSat-2 data, over both smooth and complex glacial terrain, for elevation change studies.

The Ph.D study has been carried out as part of the project **Stability and Variations of Arctic Land Ice** (SVALI) under the **Top-level Research Initiative** which is a major Nordic collaborative venture for studies of climate, energy and the environment. SVALI is a Nordic Centre of Excellence within the TRI sub-programme **Interaction between Climate Change and the Cryosphere** (ICCC), which aims to improve our understanding of stability, variations and dynamics of the cryosphere. The general aims of SVALI are: to quantify the current and future melt-rate of land-based ice in the Arctic and North-Atlantic region, to assess the consequences of decreasing land ice volume on sea level and ocean circulation, and to assess the societal consequences of current and future glacier variations.

1.1 Scientific method and objectives

The main objective for this thesis is to measure ice surface elevations from the CryoSat-2 and ICESat mission. This to improve the understanding of the current rate of change for ice-volume/mass in the Arctic and North Atlantic region, to establish a benchmark for future measurements and input to modelling future ice mass changes and dynamic response.

The main focus of this study has been the development of practical methods for data processing of the ESA level-1 product (L1b) for estimating surface elevations and elevation changes over both smooth and complex glacial terrain. This has detailed development of new and novel approaches for both retracking, filtering and processing of CryoSat-2 data for the estimation of surface elevations and elevation changes. These new processing methods developed for CryoSat-2 is then used to determine and asses the possibility of estimating the current melt-rate of the Greenland Ice Sheet.

The retrieved observations from this study, of both elevation and elevation change, have for the purpose of this study been fully validated by comparison to airborne results, from ongoing airborne laser campaigns, over several types

of glacial terrain in the Arctic region. The results from this study was later inter-compared with results derived from the ESA L2 baseline-B product to judge the quality of both products.

The result of the Greenland study can then be combined with the results obtained by (Nilsson et al., 2015a) for the major ice caps in the Arctic, using ICESat, to gain detailed insight into the current changes in ice-mass/volume of the Arctic and North-Atlantic region.

1.2 Thesis Structure

This thesis consists of several independent sections describing the foundations, design, implementation and validation of satellite altimetry derived observations of surface elevation and elevation change over glacial terrain with a main focus on radar altimetry. The thesis also contains three articles which contents are supplementary but strongly relevant and related to the content of the thesis. These articles are described in short in Section 2.

The structure of the thesis is divided into four main areas; Chapt. 3-6 gives an introduction into the current state of the cryopshere and provides the foundations for measurements from satellite altimetry, with a special focus on the CryoSat-2 mission. Chapt. 7-9 details the design and implementation of two novel CryoSat-2 processors developed during this thesis. It further describes the advanced algorithms developed and implemented in the thesis for elevation change detection and gridding of scattered observations. The results of Chapt. 8,9 is a new surface elevation change product for the Greenland Ice Sheet and a new Digital Elevation Model (DEM) based on CryoSat-2 data from 2010-2014. In Chapt. 10 the total volume change of the Greenland Ice Sheet is estimated using the newly created elevation change product and discussed. Chapt. 11 deals with the validation of the estimated elevation and elevation change from CryoSat-2. Here, airborne laser data is used to validate the measurements and where the quality is then later inter-compared with results derived from the ESA L2 baseline-B product.

In the Chapt. 11 a summary of the work is given which highlights the most important conclusions from the thesis and in Chap. 13 details and ideas about possible future work and improvement are presented.

2 Scientific papers

Supplementary and related work carried out in this Ph.D is detailed in the following scientific papers, which are shortly summarized below and available in appendix.

Mass change of Arctic ice caps and glaciers: implications of regionalizing elevation changes.

J. Nilsson, L. Sandberg Sørensen, V. R. Barletta, and R. Forsberg.*Mass change of arctic ice caps and glaciers: implications of regionalizing elevation changes.* The Cryosphere, 9:1–12, 2014. doi: 10.5194/tc-9-1-2015.
Status: accepted

The mass balance of glaciers and ice caps is sensitive to changing climate conditions. The mass changes derived in this study are determined from elevation changes derived measured by the Ice, Cloud, and land Elevation Satellite (ICESat) for the time period 2003–2009. Four methods, based on interpolation and extrapolation, are used to regionalize these elevation changes to areas without satellite coverage. A constant density assumption is then applied to estimate the mass change by integrating over the entire glaciated region. The main purpose of this study is to investigate the sensitivity of the regional mass balance of Arctic ice caps and glaciers to different regionalization schemes. The sensitivity analysis is based on studying the spread of mass changes and their associated errors, and the suitability of the different regionalization techniques is assessed through crossvalidation. The cross-validation results shows comparable accuracies for all regionalization methods, but the inferred mass change in individual regions, such as Svalbard and Iceland, can vary up to 4 Gt a^{-1}, which exceeds the estimated errors by roughly 50% for these regions. This study further finds that this spread in mass balance is connected to the magnitude of the elevation change variability. This indicates that care should be taken when choosing a regionalization method, especially for areas which exhibit large variability in elevation change.

Greenland 2012 melt event effects on cryosat-2 radar altimetry

J. Nilsson, P. Vallelonga, S. Simonsen, L. Sørensen, R. Forsberg, D. Dahl-Jensen, M. Hirabayashi, K. Goto-Azuma, C. Hvidberg, H. Kjær, and K.

Satow. *Greenland 2012 melt event effects on cryosat-2 radar altimetry.* Geophysical Research Letters, 2015b.
Status: under review

We use CryoSat-2 data to study elevation changes over an area in the interior part of the Greenland Ice Sheet during the extreme melt event in 2012. The penetration of the radar signal into dry snow depends heavily on the snow stratigraphy, and the rapid formation of refrozen ice layers can bias the surface elevations obtained from radar altimetry. We investigate the change in CryoSat-2 waveforms and elevation estimates over the melt event, and interpret the findings by comparing to in-situ surface and snow-pit observations from the North Greenland Eemian Ice Drilling Project camp. The investigation shows a major transition of scattering properties around the area, and an apparent elevation increase of 56±26 cm is observed in the CryoSat-2 data. We conclude that this jump in elevation can be explained by the formation of a refrozen melt layer which raised the reflective surface, seen by CryoSat-2, and introduced a positive elevation bias across the region.

3 State of the cryosphere

The cryosphere can in general terms be defined as all the frozen water and soil on the surface of the Earth. This includes a large and diverse range of different bodies of ice all with varying spatial and temporal characteristics. These components are inherently sensitive to temperature changes over wide ranges of time scales. Hence the Cryosphere is a natural indicator of climate variability and provides many of the most visible signs of climate change.

In this thesis the focuses lies on the land ice component of the cryosphere. Land ice, which comprises of glaciers, ice caps and ice sheets. Combined, these components represents the vast majority of ice on the planet (excluding sea ice). These bodies of ice respond to climate change over time scales stretching from years to millennia.

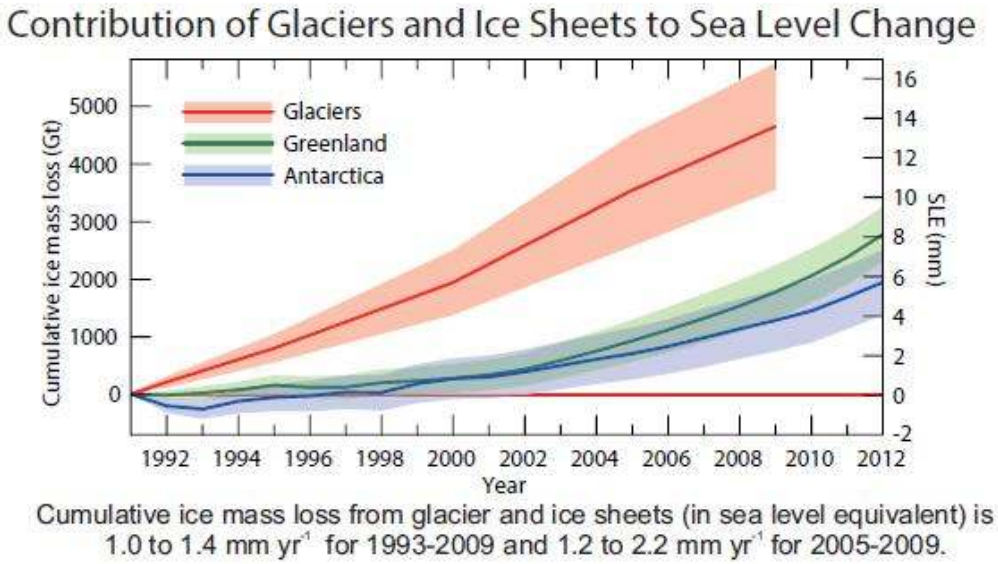

Figure 3.1 The "Intergovernmental Panel on Climate Change" (IPCC) latest estimates of Ice sheets and glaciers contribution to sea level rise from 2013. Image credit (Vaughan et al., 2013)

Recent studies indicate that the ice sheet are reacting dynamically to changes in the Earth's warming climate, where studies have confirmed an acceleration of several large outlet glaciers in Greenland, such as i.e Helheim, Jakobshavn and Kangerdlussuaq (Howat et al., 2007a; Joughin et al., 2008, 2010; Pritchard et al., 2009; Rignot and Kanagaratnam, 2006b; Rignot et al., 2004). The increase in glacier velocity have resulted in increases ice discharge and mass loss of these regions. The unloading of the bedrock, due to ice related mass loss,

have further been observed by permanent GPS (Global Positioning System) stations, such as (Khan et al., 2007, 2010)

Changes in the mass balance of the ice sheet and major ice caps have also been observed using satellite and airborne altimetry, such as (Johannessen et al., 2005; Khvorostovsky, 2012; Pritchard et al., 2009; Sørensen et al., 2011; Wingham et al., 1998; Zwally et al., 2005, 2011; **?**) 2005 and (Krabill et al., 2000, 2004). The altimetric studies show an increased thinning of the peripheral and marginal areas of the ice sheet and major ice caps, in good correspondence to the observed increase in flow velocity (Abdalati et al., 2002; Howat et al., 2007b; Thomas et al., 2008, 2009). The thinning is linked to an increase in both melt and in flow dynamics of these regions.

Arctic sea ice extent have also been declining in the last decades, with a observed decrease between 1979-2012 of 3.5-4.1% per decade with larger losses in the summer and autumn periods. Over the same time period the the extent of the multi year sea ice has also been seen declining at even higher rates of up to 13.5% per decade. This has provided a decrease in the average sea ice thickness of 1.3-2 m between 1980-2008 (Vaughan et al., 2013). An increase in permafrost temperatures of 2°C have also been observed since the early 1980s. In the northern hemisphere the southern most limit of the permafrost line has been migrating north since the the mid-1970s. Decreasing the average the average thickness of the seasonal frozen ground by roughly 32 cm since the 1930s (Vaughan et al., 2013).

The mass budget of land ice is directly linked to the sea-level, as they store or release vast quantities of fresh water. Antarctica and Greenland have the capability to increase the global sea level by around 65 m and 6 m by themselves alone (Bamber and Payne, 2004). However even relatively small imbalances, i.e. caused by anthropogenic warming, will affect global sea levels. Here glaciers, ice caps and ice sheet are believed to contribute with approximately 1.0 - 2.2 mm per year to the rise in sea level (Vaughan et al., 2013).

The uncertainty levels of these estimates are in the order of 0.6 mm per year which corresponds to almost 50% of the total signal. Hence reducing the uncertainty in the estimates is of crucial important to improve our capabilities to model and predict future sea level rise. To solve this a better understanding of the dynamics of the ice sheets is needed in conjunction with improved knowledge of the feedback mechanisms and interactions between the ice sheets and climate.

Presently the largest contributor to present-day sea level rise are smaller

ice masses such as glaciers. Glaciers presently contribute to sea-level approximately 0.76 - 0.83 mm per year at an ever increasing rate (Vaughan et al., 2013), and represents one of the most sensitive parts of the global climate system. Ice sheets are estimated to contribute far less to current sea-level rise, on the order of 0.18 - 0.37 mm per year, but are expected to accelerate during the next century (Vaughan et al., 2013).

New satellite data have during the recent years provided the ability to observe large-scale changes in the cryosphere with relativity good spatial and temporal resolution. However, longer measurement records of the cryosphere are needed to reduce the uncertainties in the long-term trends and to bring insight into the physical processes controlling the the currently observed changes.

One of the most powerful methods used to monitor the changes in the cryosphere is satellite altimetry. Satellite altimetry have provided a continuous record of the changes in the land and sea ice cover for the last two decades. This technique have experienced rapid growth in the last decade, with new satellite mission, such as CryoSat-2, ICESat-1,2 and the Sentinel missions. These mission provides unprecedented capabilities and opportunity to monitor the changes in the cryosphere.

Satellite altimetry and its capabilities for monitoring the changes in land ice of the cryosphere will be explained and discussed in the following chapters of this thesis.

4 Satellite Altimetry

Satellite altimetry is a space-borne technique used to estimated the Earth's topographical relief, by measuring the distance between the satellite and the Earth's surface. For cryospheric monitoring the technique is used to monitor the change in surface height of the land ice as function of time. For the purpose of this study the concept of satellite altimetry can be divided up into two categories (1) laser altimetry and (2) radar altimetry. This as they depend on two independent ranging techniques, with different drawbacks and benefits, such as different ground-footprint size and frequency. In this chapter the fundamentals of satellite altimetry common to both techniques will be covered. Details about the different techniques will be discussed later in the following chapters.

4.1 Basic principles

Altimeters are active sensor system that emits pulses of electromagnetic energy. The surface topography is determined by measuring the two-way travel time t of the transmitted pulse. From the two-way travel time, the range R_0 to the surface can be defined as:

$$R_0 = \frac{c \cdot t}{2} \tag{4.1}$$

where c the speed of light in vacuum. The estimated range R_0 is in reality not the true range to the surface. Because the propagation of the electromagnetic wave is affected by different errors sources, such as instrumental and geophysical errors. These errors are usually expressed in the form of a range correction ΔR_i that needs to be applied to obtain the true range:

$$R = R_0 - \sum_{i=1}^{N} \Delta R_i \tag{4.2}$$

The corrections and error budget are described in more detail in the following sections. The surface height or elevation H can then estimated by differencing the satellites altitude A, above a reference ellipsoid, with the estimated range.

$$H = A - R \tag{4.3}$$

H is usually refereed to as the ellipsoidal height, i.e the surface height above the reference ellipsoid. The altitude A of the satellite is very accurately determined using Earth based tracking systems and signal beacons, refereed to as **precise**

orbit determination (POD) systems. Most common systems used for this are **global positioning satellites** (GPS) receivers on the satellite, and the ground based global beacon network **Doppler orbitography and radiopositioning integrated by satellite data** (DORIS) system.

The basic measurement principles and error source in satellite altimetry can be seen in Fig. 4.1.

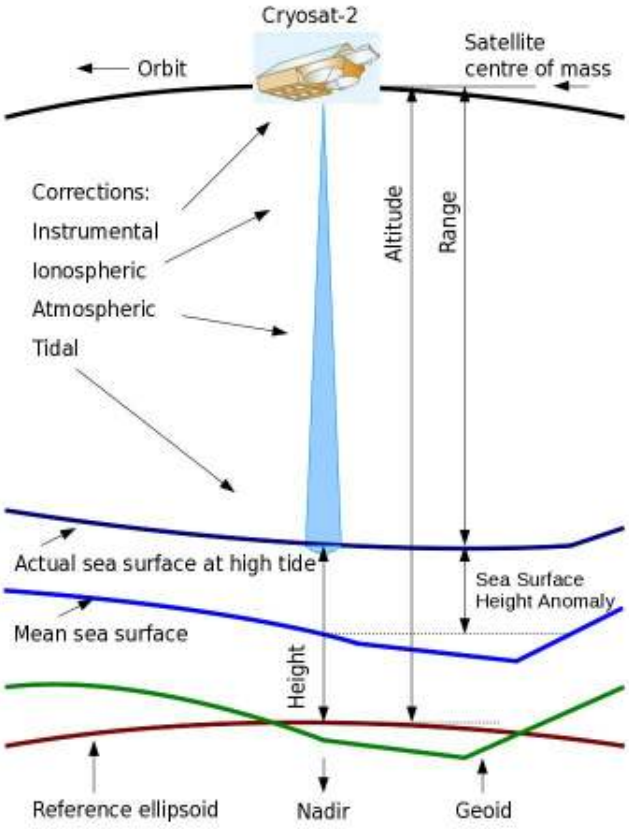

Figure 4.1 Basic CryoSat-2 altimetric terms and corrections over open ocean surfaces. Image credit (Bouzinac, 2014).

4.1.1 Surface echo

Altimeters are for most cases nadir pointing instruments transmitting electromagnetic pulses. The shape of the return signal is known as the waveform and it represents the time evolution of the surface reflected powers magnitude. Using the shape of the waveform one can for e.g radar altimeters also gain information about the physical properties of the measured surface.

Due to design limitations and practicality the altimeter measures only over a narrow set of ranges, usually called the range window. As the difference in range changes over the satellite orbit path, due to change in topography, the range window must be adjusted accordingly. This adjustment is done by an on-board tracker which minimize the risk that large topographical changes will force the altimeter to lose track of the surface. The on-board tracker uses the previously measured echoes to predict the location and height of the next coming echo from the surface. The on-board tracker purpose is to keep the initial rising part, refereed to as the **leading edge**, of the waveforms centred at the mid-point of the range gate window. This as the range to the surface is usually referenced to this location for most altimeters.

The measured return waveform, illustrated in Fig. 4.2, is used to derive the range to the surface and thus the surface height. The waveform is characterized by a initial rise in power (leading edge), as the transmitted pulse first hits the surface at nadir. Once the power has reached its maximum, when the surface is fully illuminated by the pulse, it will start to decrease. This decrease is refereed to as the **trailing edge** of the waveform and represent the return power further away from nadir. Fig. 4.2 illustrates the principle of the a radar waveform as a function of delay time, where a both the leading and trailing edge can be seen.

4.1.2 Geophysical range corrections

In this section the different geophysical errors sources affecting altimeter derived measurement will be presented. However, in depth details of the different models used and theory will not be put forward in this section, instead the reader is refeered to (Fu and Cazenave, 2000) and (Bouzinac, 2014). Some of the parameters will be discussed more thoroughly in Sections 4.2.4 and 4.3.6.

When estimating the range to the surface from spaceborne altimeters several geophysical corrections need to be applied. These corrections are usually applied as a correction to the measured range. For land ice studies there are

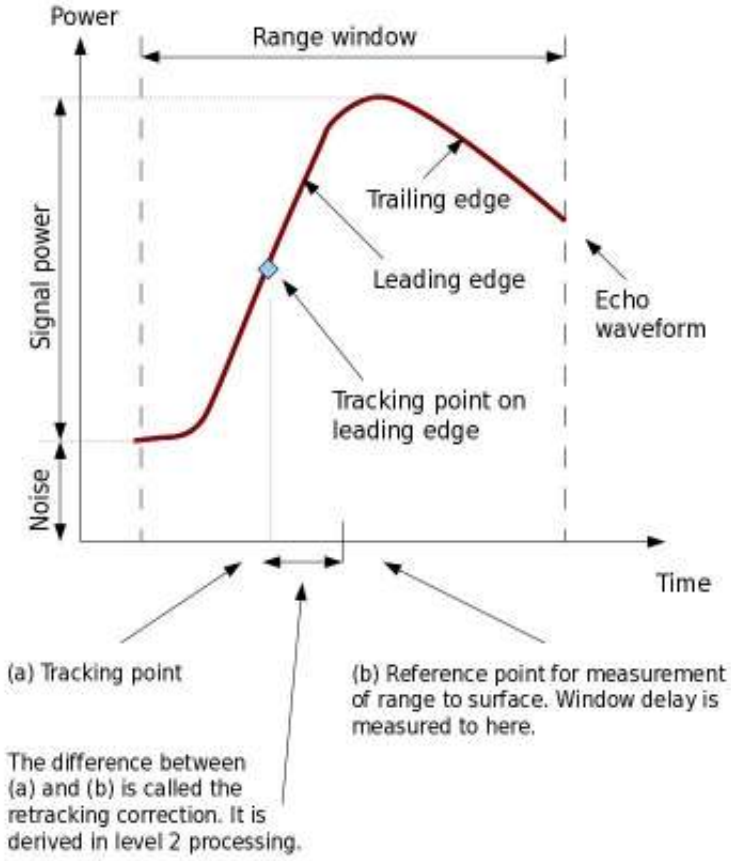

Figure 4.2 Idealized representation of a surface return signal from a radar altimeter over a flat ocean surface. The figures shows the leading and trailing edge of the waveform, and the point on the leading edge corresponding to the estimated range to the surface. Image credit (Bouzinac, 2014).

several important corrections that need to be applied to obtain a good estimate of the range to the measured surface.

- **Ocean Loading Tide:** This correction removes the deformation of the Earth's crust due to weight of the ocean tides. Typical values for this correction lie in the range of -2 to +2 cm.
- **Solid Earth Tide:** This correction removes the deformation of tidal forces from the Sun and the Moon that are acting the Earth's body. This correction lies in the range of - 30 to +30 cm.
- **Geocentric Polar Tide:** This correction removes the long-term distortion of the the Earth's surface due to variations in the centrifugal force,

due to changes in the Earth's rotational axis. This correction has a range of -2 to +2 cm.

- **Dry and wet tropospheric correction:** Compensates for the effect of non-polar gases, such as oxygen and nitrogen and has typical range of 1.7 to 2.5 m. The wet tropospheric correction compensates for the polar-gases, mainly water vapour and has a range of 0 to 50 cm. These will be discusses in more detail in Sections 4.2.4 and 4.3.6.
- **Ionospheric correction:** This correction compensates for the free electrons in the upper atmosphere, which is slowing the (radar)-signal down, due to solar activity. This correction has a typical range of 6 to 12 cm and is discussed more in Section 4.3.6.

As see here the different correction vary in magnitude and have thus different importance for the estimated range. The main parameter that the estimated range needs to be corrected for is the solid Earth tide and the atmospheric corrections, as this sum up to almost 3.5 m. The range of the different corrections have been taken from (Bouzinac, 2014).

4.2 Laser Altimetry

In this section the basic foundation of laser altimetry is presented and discussed thoroughly. This includes the theoretical background of the measurement principle and the expected accuracy of typical laser altimeter systems. Furthermore the procedure of range estimation, typical error sources and surface interaction will be discussed.

4.2.1 Basic principles of laser altimetry

Laser altimetry is an application of the LiDAR (Light Detection And Ranging) technique and is quite straightforward to conceptualise. A short pulse of light is transmitted down to the Earth's surface and is then received some time later by the satellite receiver. The surface height can then be estimated according to Eq.(4.18), as previously described. Satellite-based laser altimeters as the **Ice, Cloud, and land Elevation Satellite** (ICESat), normally operates in the nano-meters wavelengths (532 and 1064 nm for ICESat) emitting pulses with a duration of an order of a few nano-seconds (5 ns for ICESat). The accuracy of laser ranging system can be determined from the rise-time t_r (Rees and Rees, 2012) of the return pulse and the signal-to-noise ratio (SNR). The

timing accuracy of the ranging system is then governed by the ratio between these two parameters:

$$\delta t = \frac{t_r}{SNR} \tag{4.4}$$

where δt is the timing accuracy of the received transmitted pulse. The rise-time of a typical transmitted pulse depended mainly of the roughness and topography of the surface, see Fig 4.4. The SNR depends highly on the reflectivity of the surface and the range to the surface. The ranging accuracy δH of the laser system can be determined according to:

$$\delta R = \frac{v_g t_r}{2 \cdot SNR} \left(\frac{v}{R \cdot B \cdot f_{PRF}} \right) \tag{4.5}$$

where the v_g is the group velocity $v_g \approx c$, v the platform velocity, f_{PRF} the pulse-repetition-frequency, B the system beam-width and H the range to the surface.

The range accuracy is clearly dependent on the pulse-repetition-frequency of the system, hence increasing it would enviably increase the accuracy of the system. However, the PRF can only be increased up to a specific point after which the range measurements will become ambiguous. Because that the receiver can not differentiate the different pulses and resulting returns from each other. To avoid this situation a specific criteria needs to be enforced on the PRF:

$$f_{PRF} < \frac{v_g}{2R} \tag{4.6}$$

Enforcing this condition we can no range ambiguities will arise in the measurements (Rees and Rees, 2012).

4.2.2 Range estimation from laser altimetry

The range to the mean surface illuminated by the transmitted laser pulse is determined by the travel time of the pulse, also taking into account pulse spread. The size of the illuminated footprint of a typical space-borne altimeter is on the order of ∼100 m. The transmitted pulse of laser altimeters has an approximated Gaussian time distribution. The shape of the return waveform mainly depends on the transmitted pulse shape, atmospheric propagation and physical interactions with the surface. This has the effect that if both surface and atmospheric interaction are small the return shape of the waveform also will be Gaussian.

Noting that most waveforms are Gaussian in nature and can approximated very well by a Gaussian function or a sum of overlapping Gaussian pulses with an added noise bias, seen in Fig.4.3. For the purpose of land ice studies mostly single peak return are expected. However, for regions with more complex topography, where multiple surfaces might exist inside the footprint, several or overlapping Gaussian-shaped returns could be expected. Hence a common model used for laser altimetry is the one developed for the ICESat-mission (Zwally et al., 2002), which is based on the summation of Gaussian pulses with a noise bias, according to:

$$P(t) = \varepsilon + \sum_{m=1}^{N_p} A_m \exp\left[-\frac{(t-t_m)^2}{2\sigma_m^2}\right] \quad (4.7)$$

In Eq. 4.7 N_p is the number of peaks in each pulse, ε is the noise bias, A_m is the amplitude, t_m is the temporal center and σ_m is the standard deviation of the m:th Gaussian peak, seen in Fig. 4.3. The model parameters can be solved for using several different least squares techniques, both linear and non-linear. The

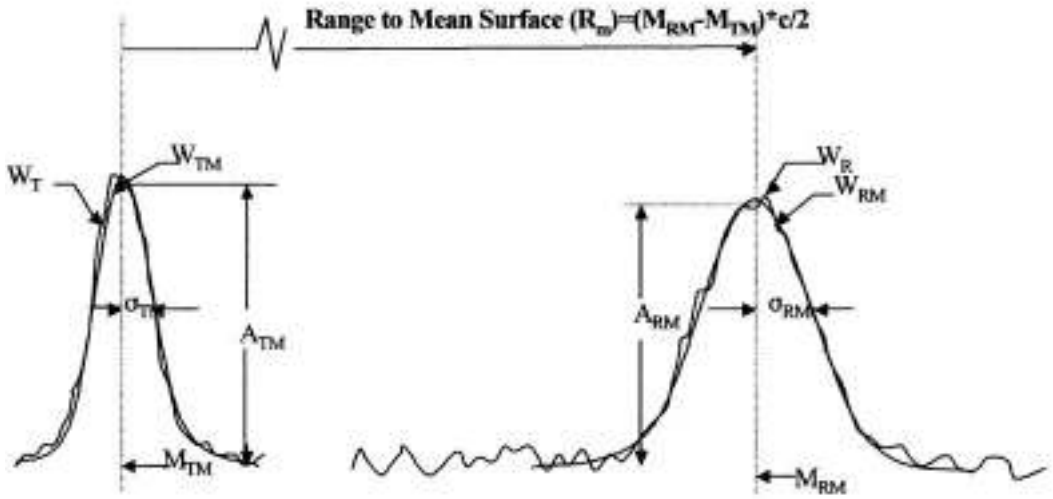

Figure 4.3 Estimation of surface range and elevation distribution from a standard transmitted and received laser pulses. Here (W) represents the pulse or the modelled waveform, T is the transmitted pulse, R the received pulse, subscript M refers to the fitted Gaussian waveform, M referees to the waveforms mid-point and σ is the standard deviation of the waveform. Image credit (Zwally et al., 2002)

range to the surface is then defined as the time difference between the centroid

of the transmitted pulse to the center of the point of the last Gaussian-fitted peak of the return, according to:

$$R = \frac{c \cdot (t_R - t_T)}{2} \tag{4.8}$$

where c is the speed of light in vacuum, t_R is time of the received pulse and t_T is the time of the transmitted pulse. The centroid-to-center approach is applied to reduce the effects of forward atmospheric scattering on the estimated range.

4.2.3 Estimating surface characteristics from laser altimetry

Due to the interaction of the laser pulse with the reflective surface, information can also be extracted of the surface characteristics. As the transmitted pulse is reflected from the surface, the height distribution inside the illuminated footprint affects the pulse shape by broadening it. The magnitude of broadening is a function of the mean surface slope and surface roughness inside the footprint. Monitoring the interaction between small-scale surface roughness and wind patterns is both important for boundary-layer meteorology and determination of the history and magnitudes of surface winds. Measuring the surface roughness component directly is not possible, as it is a combination of both the slope and roughness, see Fig 4.4. The surface roughness can only be separated first when the surface heights, and hence the slopes, have been determined. The estimation of surface roughness is further important to estimate, as it is a limiting factor on the accuracy of the derived surface heights. The surface roughness can be used for example to map areas where surface height extraction might be problematic or used to flag possible bad data.

4.2.4 Error sources in laser altimetry

One of the main error sources in laser altimetry is the pulse propagation due to the atmosphere, which can be divided up into the atmospheric delay correction and atmospheric forward scattering.

Atmospheric delay correction: Determination of the range to the surface depends on the pulse propagation speed, e.g the group velocity. The group velocity speed v_g depends on the wavelength, atmospheric pressure, temperature and vapour content. In general the atmosphere is divided into (1) dry atmosphere (atmospheric gases such as oxygen, nitrogen and carbon dioxide)

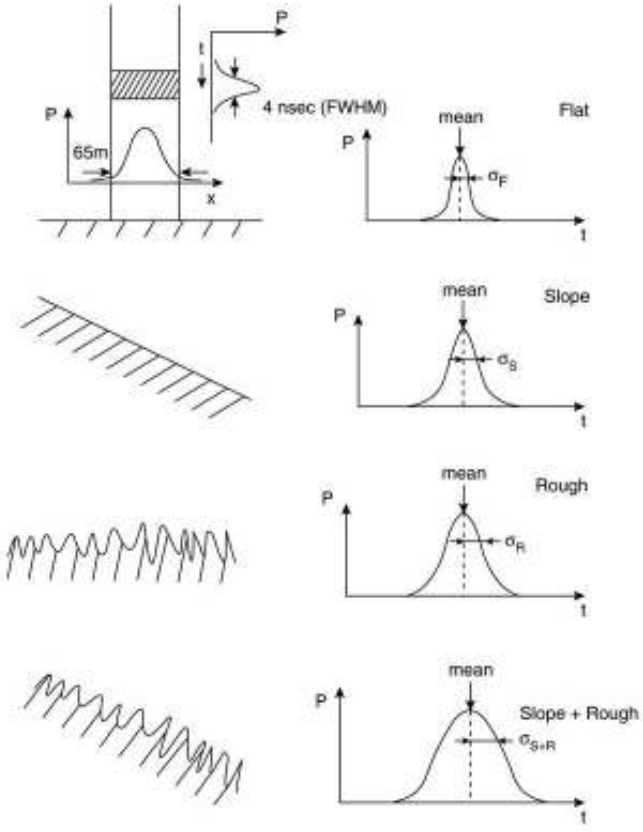

Figure 4.4 Typical effects of surface slope and surface roughness on the transmitted laser pulse. The interaction between the pulse and the surface height distribution inside the illuminated footprint will broaden the transmitted pulse. Image adapted from (Zwally et al., 2002)

and (2) wet atmosphere (water vapour). For spaceborne measurements these parameters are not constant along the path of the propagating pulse and needs to be integrated to find the travel time.

$$t = \int_0^z \frac{1}{v_g} dz' \tag{4.9}$$

where z' is the ray path. This can be re-written as integral of range instead (Rees and Rees, 2012).

$$P = \int_0^z \left(\frac{c}{v_g} - 1 \right) dz' \tag{4.10}$$

This quantity P is useful as it is proportional to the integrated number of molecules along the path. At optical wavelengths the dry component is the

sum of the hydrostatic delay along the ray path, which is a function of surface pressure. The wet component is a function of the total column of integrated water vapour along the path. For surface pressure of roughly 1000 mbar the hydrostatic delay corresponds to approximately 2.4 m. For Arctic regions the wet delay is usually less than 1 mm, due to the low content of water vapour in the atmosphere in these regions (Rees and Rees, 2012).

Atmospheric forward scattering: The high frequency of the laser altimeter forces scattering of the laser beam against aerosols and other molecules in the atmosphere. This scattering attenuates and broadens the return signal and can in cases block all ground returns entirely. Thinner clouds and aerosols will cause forward scattering of the return signal, and distorts the shape and shifts the centroid position of the waveform. Heavy clouds are opaque for laser frequencies, which has the effect that cloud cover will completely attenuate the laser beam and block all ground returns.

4.3 Radar Altimetry

In this section the foundation of radar altimetry will be presented and discussed thoroughly. This includes the theoretical background of the measurement principle and the expected accuracy of typical laser altimeter systems. Different types of radar techniques, common in radar altimetry, is also presented for the purpose of land ice studies. The aspects of range estimation, surface interaction and error sources will also be discussed.

4.3.1 Basic principles of radar altimetry

Radar altimetry is similar in operation to laser altimetry in the sense of that an electromagnetic pulse is transmitted to and reflected from the Earth's surface, and where the round trip time is measured to derive the surface topography. The main difference between the two systems is that radar altimeters operate at much larger wavelengths and have substantial larger ground footprint. Typical spaceborne radar altimeters operate in the Ku-band 12-16 GHz, corresponding to a wavelength of 1.6-2.5 cm and can have a ground footprint of several kilometres in diameter. The monostatic single pulse radar equation is often used to describe the relation between the transmitted P_t and return

power P_r from the illuminated area of the radar footprint.

$$P_r = \frac{\lambda^2 G^2 P_t}{(4\pi)^3 \eta R^4} \sigma_0 A \tag{4.11}$$

where λ the wavelength, G the antenna gain, η the antenna efficiency coefficient, R is the range to the surface, A is the surface scattering area and σ_0 is the backscattering coefficient. For a single pulse the received energy from the surface E_r can be given by the peak power (P_{peak}), the pulse length (τ) and the ratio between the received and transmitted power (Γ) (Sullivan, 2004).

$$E_r = P_{peak} \tau \Gamma \tag{4.12}$$

The signal-to-noise ratio for a single pulse radar system is then given by the received energy divided by the thermal noise of the radar system (kT_s) and bandwidth correction factor C_B (Sullivan, 2004).

$$SNR = \frac{E_r}{kT_s C_B} = \frac{P_{peak} A^2 \eta^2 \sigma \tau}{4\pi \lambda R^4 k T_s C_B L} \tag{4.13}$$

The radar equation is considered to be the fundamental equation in radar design. From Eq. 4.13 one can observe that the SNR in a radar system is governed by several parameters. Most of these parameters that control the SNR have physical or design limitations, and the range accuracy of a single pulse is mainly governed by the length of the transmitted pulse τ. To avoid range ambiguities, the pulse repetition frequency (PRF) of the radar system has to be chosen so that all pulses are uncorrelated. The PRF criterion is defined in the same manner as for laser altimeters in 4.6. The SNR of a radar system can be greatly increased by averaging several pulses together, which is often done.

4.3.2 Beam and pulse limited radars altimeters

Altimeters are commonly categorized into beam and pulse-limited altimeters. Radar altimeters are mostly pulse-limited while laser altimeters are beam-limited. The beam-limited altimeter surface return footprint is governed by beam-width of the antenna, and thus inversely proportional to the antenna diameter. The size D of the beam-limited footprint for a circular antenna is given by:

$$D = 2H \tan\left(\frac{k\lambda}{2d}\right) \tag{4.14}$$

where H is the altitude of the satellite, k antenna specific parameter, λ the wavelength and d the antenna diameter.

The size of the beam-limited footprint depends on the antenna diameter (Eq. 4.14), narrow beams requires a large antenna diameter. This is usually very impractical for spaceborne systems, as large antennas are difficult to deploy and build. Furthermore beam-limited antennas are also highly sensitive to antenna mispointing errors, which affects the range accuracy (Satellite Altimetry, 2001).

The limitations of beam-limited altimeters can be overcome by transmitting a very short pulse from an antenna with a smaller diameter and a wider beamwidth. This is refereed to as a pulse-limited radar altimeter. For a pulse limited radar altimeter the footprint size only depends on the compressed pulse duration, according to:

$$R_p = \sqrt{c\tau H} \tag{4.15}$$

where R_p is the radius of the pulse-limited footprint, c speed of light in vacuum, τ the pulse length and H the satellite altitude (Fu and Cazenave, 2000).

4.3.3 Interferometric Synthetic Aperture Radar

In conventional pulse-limited altimetry the height precision is governed by the pulse length and the amount of averaging available for each measurement. As the pulse length determines the diameter of the pulse-limited footprint only power from within the footprint is used for range estimation. This implies that pulse-limited radars are wasteful of radiated power (Keith Raney, 1998), as the pulse-limited footprint is on average several factors smaller than the beam-limited half power width. Hence, most of the transmitted radiated power falls outside the pulse-limited footprint and is not used in the height estimation. To overcome this issues "Synthetic aperture radar" (SAR), also known as "Delay/-Doppler" radar was introduced by (Keith Raney, 1998). This new type radar produces higher return power, smaller pulse-limited footprint and high speckle reduction from averaging multiple looks.

The SAR scheme takes advantage of the Doppler shift in the pulse frequency, caused by the forward motion of the platform, which allows for an increase of the PRF and sub-division of the illuminated are into discrete Doppler cells. This procedure dramatically improves both the efficiency and precision of the radar. Groups of pulses, refereed to as bursts, are transmitted and reflected from the Earth's surface. The received pulses are then coherently correlated within each burst, which allows for the usage of the full Doppler bandwidth.

The shift in frequency, due to the Doppler effect, is then used to divide the illuminated area into discrete Doppler cells along-track. This is refereed to as Doppler beam formation and results in higher ground track resolution. The focused Doppler beams or cells cover the pulse-limited footprint as rectangular strips, oriented across-track. As the platform move along its path these cells inside the footprint are sensed multiple times. This is refereed to as multi-looking, as each cell is illuminated several times", and these successive burst or looks are then averaged to reduce speckle noise.

As a result of the beam formation and multi-looking the resulting waveform has a very steep leading edge, a fast decaying trailing edge compared to conventional radar altimeters, and a peak power ∼10 dB higher than for conventional altimeter waveforms (Keith Raney, 1998). This is depicted in Fig 4.5. The pulse-Doppler limited area for a SAR footprint can be approximated by a rectangular area. The rectangular area is given by the pulse-limited footprint width across-track and (narrowed) beam-limited area width along-track, as seen in Fig. 4.5. Given that the band of Doppler frequencies is unambiguously sampled by the PRF, the width x_D of the pulse-Doppler limited area becomes:

$$x_D = \frac{h\lambda}{2v}\frac{f_{PRF}}{N_{beams}} \tag{4.16}$$

where h is the altitude of the platform, v is the platform velocity, f_{PRF} is the pulse repetition frequency, N_{beams} is the number of Doppler beams, according to (Bouzinac, 2014).

In ordinary SAR operation only the amplitude of the signal is measured and the phase content is discarded or ignored. However, with the inclusion of a second antenna on the platform interferometric SAR can be performed. Interferometric SAR uses the fact that echoes from off-nadir introduce a phase-shift of the returned signal, which corresponds to the difference in the path length of the signal. The phase difference $\Delta\phi$ is related to the angle of arrival θ in the following way:

$$\sin(\theta - \beta) = \frac{\Delta\phi}{kB} \tag{4.17}$$

where, B is the antenna baseline, k is the wavenumber and β is the roll angle of the platform, according to (Wingham et al., 2006)

By comparing the difference between the transmitted and return phase, the angle of arrival can be determined. Using the angle of arrival in combination with simple geometry, the position of the surface echo can be determined. This allows for highly accurate mapping (depending on the method used) and height

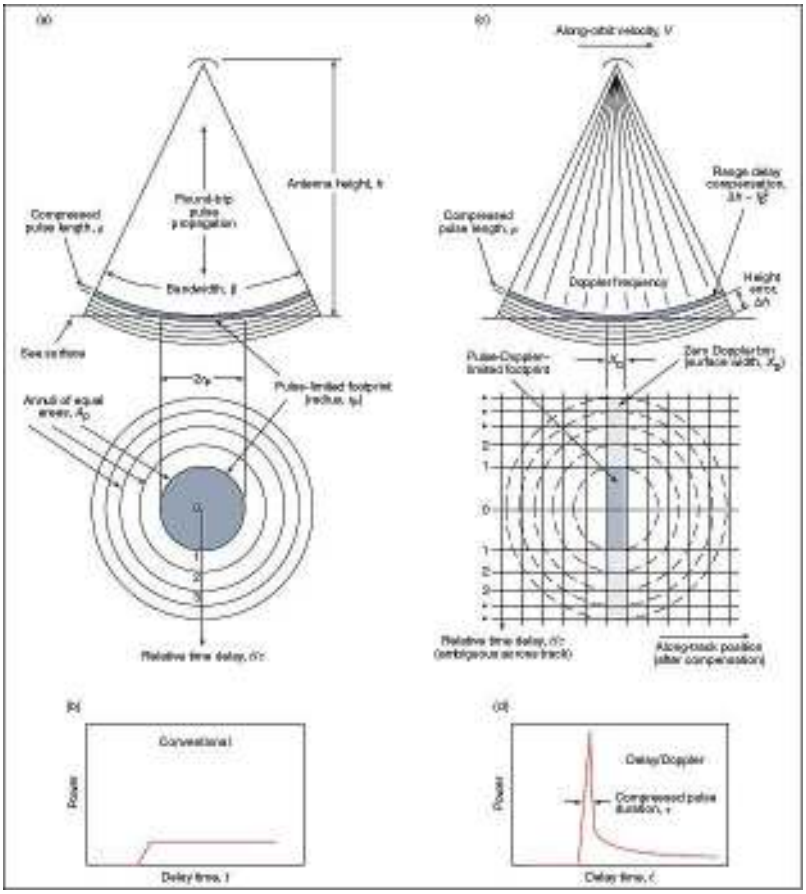

Figure 4.5 Principles of conventional radar (left) versus SAR (right), depicting the difference in illuminated footprint and waveform response. Image credit *Johns Hopkins University/Applied Physics Laboratory* and *ESA*.

determination in areas of rough topography, like the margins of the ice sheets.

4.3.4 Range estimation from radar altimetry

Over non-uniform surfaces the on-board tracker usually fails to keep the waveform centred in the range gate window, as it can not fully compensate for the undulating topography. This introduces an offset between the recorded and physical range to the surface and needs to be corrected to obtain the true surface height. This offset is usually known as the retracking correction and is a range correction that needs to be applied in the post-processing stage. In prac-

tice waveform retracking is performed by identifying the so called retracking point on the leading edge. The retracking point, see Fig 4.2, is then assumed to be representative measure of the mean surface height inside the altimeter illuminated footprint. The retracked range R_{rt} is then used to find the surface height, as follows:

$$H = A - \left(R_{rt} + \sum_{i=1}^{N} \Delta R_i \right) \tag{4.18}$$

Determination of the retracking point on the leading edge to find the surface height will vary according to the method used, introducing a retracker dependent height differences. There are two main families of so called retrackers, used for satellite altimetry: (1) model-based retrackers and (2) statistical retrackers. Model-based retracker fits a predefined physical or empirical model to the waveform, which is based on knowledge of the scattering properties of the measured surface. The statistical retrackers are based on the statistics of the waveform, and are not based on any type of physical or empirical modelling.

Several studies, such as (Davis, 1995), have been performed to determine the impact of different retrackers for the purpose of studying land ice. The result of these studies indicate that the model-based retrackers produce more accurate surface heights (Ferraro and Swift, 1995; Ridley and Partington, 1988), as they are developed to take into account changes in surface scattering properties of land ice. (Davis, 1997a) showed that retrackers based on the statistics of the waveform are preferred for elevation change studies, as they on average produce more robust and repeatable elevations. This was also recently shown by (Helm et al., 2014), when comparing several types of retrackers for CryoSat-2.

4.3.5 Estimating surface properties from radar altimetry

As previously stated in Section 4.3.1 radar altimeters operate at much lower frequency (microwave-band) and has considerably larger footprint than its laser counterpart. This has the effect that the transmitted radiation interacts more with the physical surface than to laser, providing more information about the surface. This can be viewed as both strength and a weakness that and is discussed in more detail in Section 4.3.6 and Section 5.2. The interaction of the transmitted radar signal with the surface has the same affect as with laser altimeter, i.e broadening the pulse, and the interaction with the surface changes changes both the magnitude and shape of the waveform. Radar waveform analysis has been used in previous studies to characterize surface properties over both land and ice. (Papa et al., 2003) used this type of analysis to classify dif-

ferent types of land surfaces, (Alsdorf et al., 2001) used it to study hydrological systems and (Legresy, 1998; Legrésy and Rémy, 1997; Remy et al., 1990, 1996) used it to characterize surface roughness and snowpack structures.

For land ice studies radar waveform analysis can be used to give insight about the surface conditions of the ice sheet. Knowledge of these properties are, as discussed in Section 4.2.3, important because they are (1) related to climatological parameters (such as wind, precipitation and air temperature) and (2) crucial for a correct analysis of altimeter data. Microwave sensors are particularity sensitive to changes in cm-scale surface roughness and snow density, as they affect the waveform and bias the surface height estimation (Lacroix et al., 2008). Hence, by monitoring the change in the waveform shape the effect of height estimation reduced, and information gained about the current state and evolution of the land ice surface. The waveform shape can be described

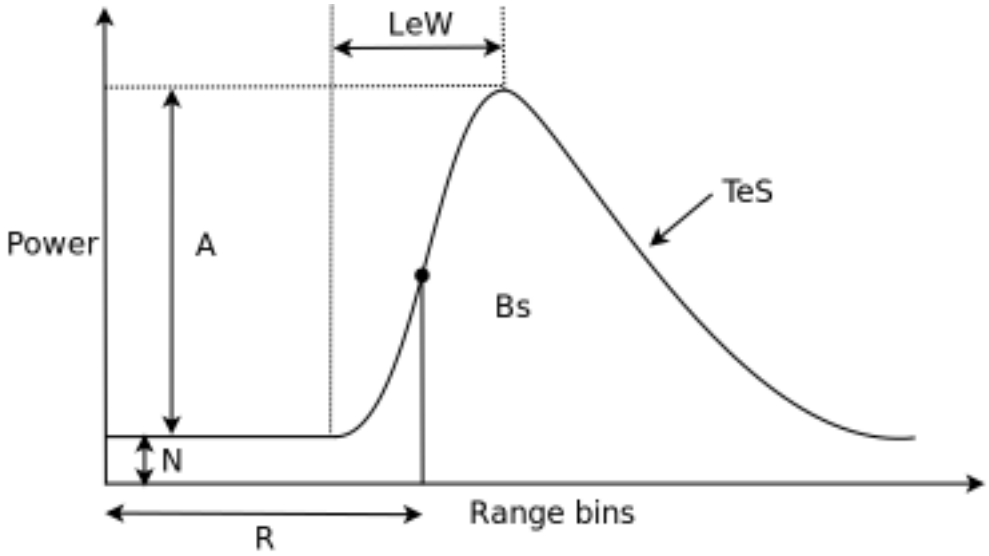

Figure 4.6 Illustration of a radar waveform detailing the position of the retracking point, amplitude (A), noise level (N), trailing edge slope (TeS), leading edge width (LeW) and the backscatter coefficient (Bs).

by several individual waveform parameters, each being sensitive to different physical traits of the physical surface. For the purpose of this study the waveform parameters have been defined according to (Legresy, 1998; Legrésy and Rémy, 1997; Legresy et al., 2005) and (Laxon, 1994). A total of four different waveform parameters, seen in Fig. 4.6 which depends on the signals interaction with the surface, are presented below:

- **Backscattering coefficient** (Bs): Is the integrated backscattered power

from the surface. Backscatter is controlled by both the surface and subsurface scattering, which is connected to the surface slope, roughness, snow density and stratification, (Legrésy and Rémy, 1997).

- **Leading edge width (LeW)**: The width of the leading edge is related to surface the macro-roughness (cm-range), small scale topography, and is further enlarged by signal penetration into the surface medium.

- **Trailing edge slope (TeS)**: The slope of the trailing edge of the waveform is mostly related to the ratio between volume and surface echoes. It is also affected by antenna miss-pointing errors, surface slope and curvature.

- **Pulse peakiness (PP)**: The pulse peakiness is related to the surface properties, as is also the backscatter, and gives an measure of how specular a surface return echo is. It can be used to classify different surface types, as function of its specularity.

These waveform parameters will then be used in Section. 9.2 to correct for height variations due to changes in surface properties of land ice. Studies have shown that there is correlation between changes in waveform parameters and surface height changes (Legresy, 1998; Legrésy and Rémy, 1997; Legresy et al., 2005).

4.3.6 Error sources in radar altimetry

The main sources error sources that affect the accuracy and precision of radar altimeters can over land ice be divided into (1) Atmospheric delays, (2) height errors due to topography and (3) signal penetration effects. These errors are described below in the following sections.

Ionospheric delay correction: The signal propagation of radio frequencies are as optical frequencies affected by the wet and dry components of the Earth's troposphere. However, microwave frequencies (in contrast to there optical counterparts) are also affected by the Earth's' ionosphere.

The ionosphere is the layer of the atmosphere in which ionizing radiation causes free electrons to exist in sufficient quantities to affect the propagation of radio waves. For radio waves the ionosphere is a dispersive medium, as its

refractive index is a function of frequency. The frequency dependency is related to the electron density η_e, i.e. the number of free electrons per volume units. The ionospheric component of the range correction can be estimated by the vertical integration of the electron density along the signal path, and scaled by frequency f (Rees and Rees, 2012).

$$\Delta R = \frac{40.3 \times 10^6}{f^2} \int_0^R \eta_e dz \tag{4.19}$$

For radar altimeter systems operating at a frequency of 13.6 GHz the range correction is on average 0.22 cm per 10^{12} electrons cm^{-2} (Fu and Cazenave, 2000). It can clearly be seen from Eq. 4.19 that the ionospheric propagation delay diminishes rapidly as the frequency increases. Unfortunately, as the frequency increases the attenuation of the signal due to the wet and dry components of the troposphere also increases.

Slope-induced errors: Potentially the largest source of error in radar altimetry is the slope-induced error (Brenner et al., 1983), which is caused by the sloping surface of the ice sheet. Over sloping terrain the return signal does not originated from the nadir location beneath the satellite. Instead it is located at the closest point between the satellite and the surface, and is usually refereed to as the **point-of-closest approach** (POCA).

This means that the satellite measures the surface height at a position up-slope from nadir, and consequently the observed surface height must be therefore relocated to the correct position, or the range to the surface must be slope corrected accordingly. For a smooth surface with a constant slope α and satellite altitude H the vertical displacement ΔH with respect to nadir is:

$$\Delta H = H(1 - \cos(\alpha)) \tag{4.20}$$

An geometric illustration of the range error introduced over a sloping surface can be seen in Fig. 4.7. The horizontal displacement D of the sub-satellite point with respect to nadir can be found from:

$$D = H \cos(\alpha) \sin(\alpha) \tag{4.21}$$

This means that for a satellite orbiting at 700 km altitude over an area with an average slope of 1°, common over the marginal areas of the ice sheets, the vertical error is estimated as ∼100 m. The horizontal displacement of the measurement location away from the nadir position is then estimated to ∼12 km.

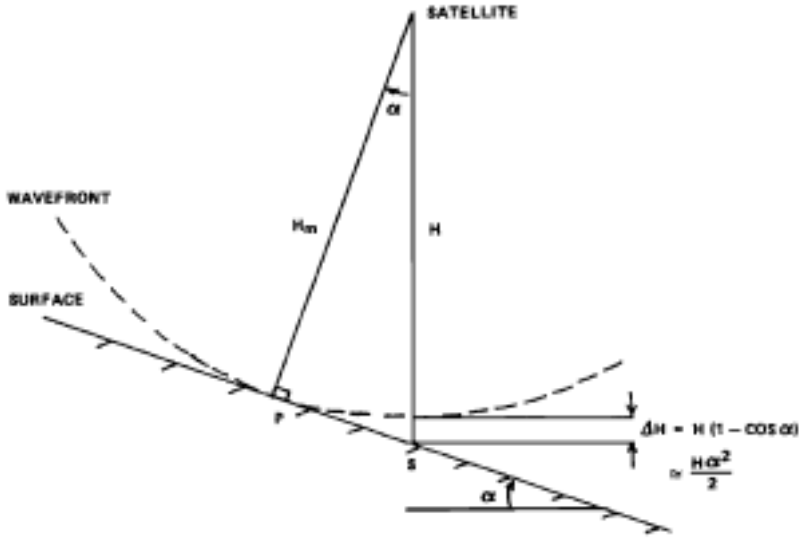

Figure 4.7 Schematic view of the slope-induced error and its relation to topography. Image credit (Brenner et al., 1983)

It should be noted that more many purposes the slope-induced error is corrected for by (1) either relocating the nadir position to the echo location, or (2) by correcting the measured range to nadir using. Both of these methods require a-priori knowledge of the local surface slope.

Surface penetration effects: Measurements made from radar altimeters over snow or firn covered areas are inherently more difficult to analyse than than those obtained over oceans. This problem arises from the fact that the interaction between the electromagnetic pulse and the reflective medium is heavily frequency dependent. The consequence of this frequency dependency is signal propagation into the medium, where the magnitude of penetration is proportional to the wavelength of the transmitted signal.

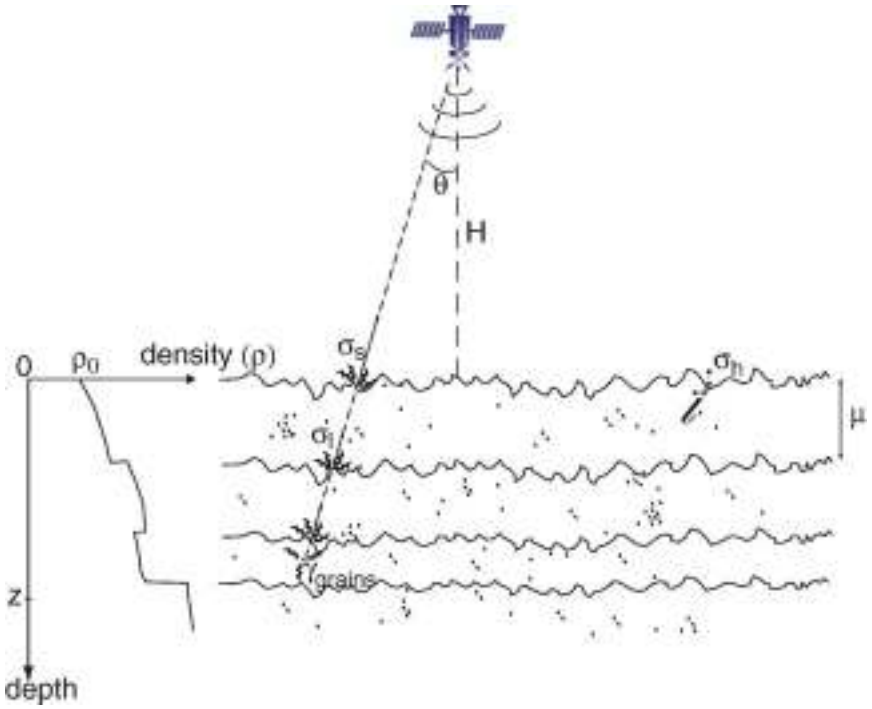

Figure 4.8 Schematic view of surface and sub-surface scattering of the radar signal due to the internal structure of the upper part of the ice surface. Image credit (Lacroix et al., 2007)

Radar altimeters, operating at microwave frequencies, do not observe the true reflective surface, but rather observe a multitude of reflections within the medium, down to a specific penetration depth, which is determined by the properties of the medium. This has the effect of biasing the measured heights and can also introduce area-wide height variations caused by changes in the properties of the medium changes.

The penetration depth into snow depends on the density and internal structure of the first few meters of the surface layers and the features present below the surface, as seen in Fig. 4.8. Features such as high density ice layers and

crystal boundaries also act as multiple reflection surfaces seen by the radar. Surface conditions also has an important effect on the depth of the dominant reflective surface, as summer or extreme melts produces melt-water which also acts as a reflective surface.

This also means that the depth of the reflective surface changes both with space and time, as it is a function of dielectric properties, temperature and water concentration. Studies have shown that for regions such as Greenland and Antarctica the penetration depth of the radar signal can vary from a few centimetres up to several meters (Davis and Zwally, 1993; Ridley and Partington, 1988).

The main issue with the surface penetration effect is that it is not constant over the ice sheet, it varies both as a function of time and space. This introduces spatial and temporal biases which are highly difficult to account for without using external and contemporary information about the surface.

5 Monitoring land ice using satellite altimetry

In this section the background of the use of satellite altimetry to measure the changes of land ice will be presented. Also a qualitative comparison will also be presented that will discusses the main difference between radar and laser altimetry.

5.1 Historical perspective

The idea of using satellite altimetry to measure the Earth's surface was first realized in 1974, when an altimeter was flown on Skylab. GEOS-3 was then launched in 1975 with an altimeter on-board designed to measure the ocean surface. The orbit of GEOS-3 was optimized for ocean studies, but did cover the southern parts of Greenland. (Brooks et al., 1978) proved that these ocean type altimeters could be used to measure the topography over Greenland.

In 1978 and 1985 two other satellite mission were launched, called SEASAT and GEOSAT, also desgined for ocean monitoring. These missions covered larger areas of the Greenland and Antarctic ice sheets and were designed to maintain track over sloping terrain, up to 1°. Using a retracking algorithm, developed by (Martin et al., 1983), (Zwally et al., 1983) produced topographic maps of the ice sheets. From this is was also possible to estimate temporal changes of the topography, by computing height difference from crossing tracks over specific time intervals. More details are presented in Section 9.1 and 9.2.

With the launch of ERS-1 and ERS-2 continuous time series of the ice sheets have been possible since 1991. These altimeters were designed with special modes to allow for surface mapping of the more sloping regions of the ice sheet margins. EnviSat was the follow-on to the ERS-1/2 and was launched in 2002. The radar altimeter on-board EnviSat was derived from the ERS radar altimeters, but providing improved measurements performance and new capabilities, such as adaptive tracking.

In 2003 ICESat satellite was launched, which contained a new and revolutionary laser altimeter. The mission was designed to overcome many of the problems adherent to radar altimeters. ICESat was designed for land and sea ice monitoring and with it's much smaller footprint allowed mapping of sloping terrain up to 3°. The mission also allowed for the monitoring of smaller ice caps and glaciers, which previously had been difficult to monitor using radar altimetry because of it's large footprint. CryoSat-2 was launched in 2010, as CryoSat-1 was lost during launch, and it carried a new revolutionary radar

altimeter. This new type of radar altimeter allows mapping over a larger range of slopes, with a comparable resolution to that of the ICESat mission. Table. 5.1 details a summary of the different mission used for land ice monitoring since the end of the 1970s.

Satellite	Operation	Type	Coverage	Repeat period (days)
SEASAT	June-Aug 1978	Radar	±72°	24
GEOSAT	June-Aug 1978	Radar	±72°	17, 540
ERS-1	1991-1995	Radar	±81.5°	3, 35, 336
ERS-2	1995 2002	Radar	±81.5°	3, 35, 336
ENVISAT	2002-2012	Radar	±81.5°	35
ICESAT	2003-2009	Laser	±86°	8, 183
CRYOSAT-2	2010-Present	Radar	±88°	30, 369

Table 5.1 Previous and current satellite altimeter mission used to measure present-day changes of land ice.

5.2 Qualitative comparison between laser and radar altimetry

There are several advantages and disadvantages using laser and radar altimetry for monitoring land ice and these will be discussed in this section. As previously described the two main differences between laser and radar altimetry is (1) the operational frequency and (2) the beam-limited footprint. The differences in these two parameters have a considerable influence on the precision and accuracy of the two techniques.

Laser altimetry has the advantage, compared to radar altimetry, that its beam-limited footprint is small, on the order of 50-100 m meaning that a very accurate estimate of the echo location is possible. The high frequency also means that the signal will not penetrate far into the surface, which allows for accurate mapping of the physical surface. However, due to the high frequency, heavy cloud cover (common in the Arctic) will fully attenuate the signal, which reduced the total number of available observations.

Radar altimetry can on the other hand, due to its lower frequency, monitor the surface continuously as it is not affected by weather conditions, such as cloud cover. Its larger footprint also allows for a larger area to be surveyed within each range measurement. However its precision and accuracy is limited due to the slope induced error and signal penetration into the surface.

6 The CryoSat-2 mission

The CryoSat-2 radar altimetry mission was launched in 2010 with the purpose of monitoring the Earth's cryosphere. Its primary objective is to measures the changes of land and sea ice due to climate change. Precise measurements from CryoSat-2 of the rate of change in the thickness of land and sea ice will allow for better understanding of the interactions between climate change and sea level rise.

CryoSat-2, seen in Fig. 6.1 was especially designed for overcoming many of the intrinsic difficulties of monitoring ice covered surfaces, mentioned previously in Chapter 2. It has improved ability to monitor the polar regions due its high-inclination orbit, reaching latitudes of 88 degrees, improving coverage compared to other missions. CryoSat-2 also carries a new generation of altimeter; the SAR/Interferometric Radar Altimeter (SIRAL), especially designed to monitor the variations in ice thickness in the marginal areas of the ice sheets and mountain glaciers.

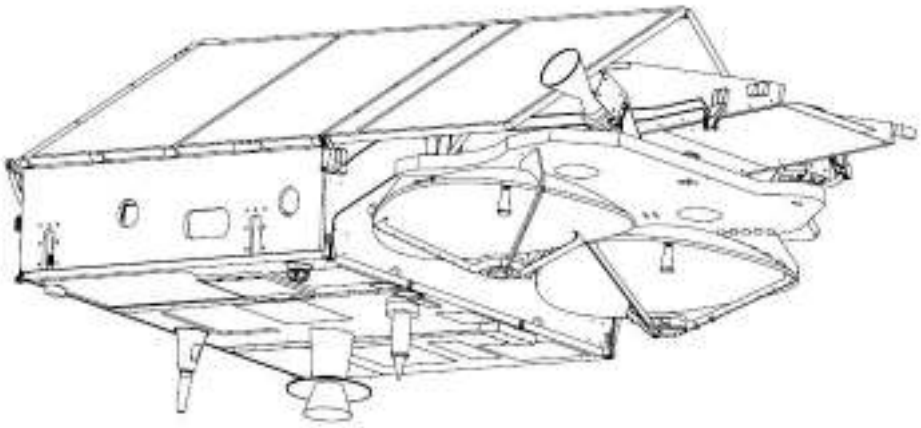

Figure 6.1 CryoSat-2 satellite configuration, depicting its two antennas and other instruments. Image credit (Bouzinac, 2014)

6.1 SIRAL specification and operational modes

The SIRAL altimeter operates at a frequency of 13.5 GHz (Ku-band) in three different modes measure land and sea ice. For the purpose of monitoring land ice only two modes are used; over the flat areas in the interior of the ice sheets the **Low Resolution Mode** (LRM) is used, equivalent to conventional

radar altimetry. For areas with more complex topography, like the marginal areas of the ice sheets and mountain glaciers, the **interferometric synthetic aperture mode** (SARin) is used. The SARin mode uses an extra antenna to perform interferometric processing to determine the across-track angle of the return echo. Measuring the across-track angle will allows for exact determination of the location of the surface echo in sloping terrain. The mode of operation is selected from a predefined geographical mode mask, see Fig. 6.2. The mode mask is updated every two weeks to allow for changes.

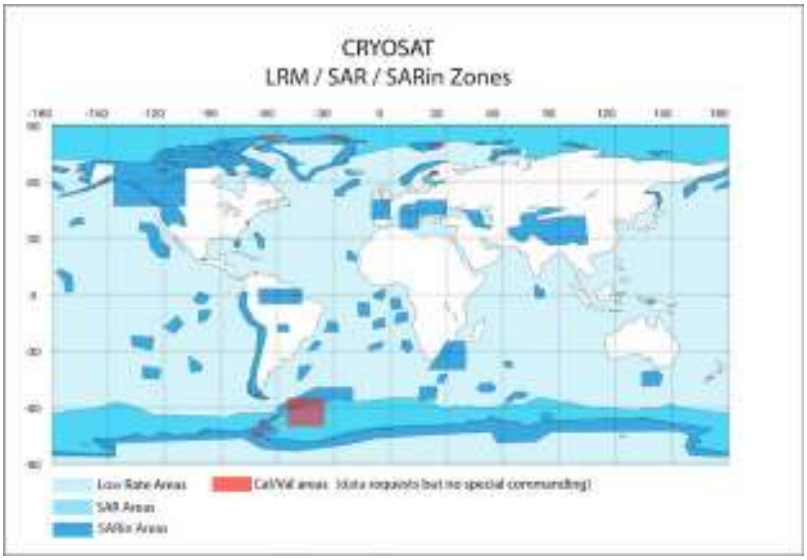

Figure 6.2 CryoSat-2 geographical mode map. Image credit: http://www.esa.int

The different modes have different specifications, as they are designed to monitor different aspects of the surface. However, the main specifications of the SIRAL altimeter are described in Table. 6.1.

Frequency	13.575 GHz
Pulse bandwidth	320 MHz
PRF	LRM 1.97 KHz, SAR/SARin 18.181 kHz
Burst mode	1970 Hz (LRM), 85.7 Hz (SAR), 21.4 Hz (SARIn)
Compressed pulse length	3.125 nm
Pulse duration	44.8 μs
Samples in echo	128 in LRM/SAR, 512 SARin
RF peak power	25 W
Antenna beamwidth	1.06° x 1.1992° (along x across track)
Antenna footprint	15 km
Range bin samples	0.2342 m SAR/SARin and 0.4684 m LRM
Instrument power	149 W
Antenna baseline	1167.6 mm

Table 6.1 SIRAL characteristics for the LRM/SAR/SARin mode, adapted from (Bouzinac, 2014)

6.2 Data products

There are essentially four different steps or levels in the CryoSat processing, called level-0, level-1, level-1b and level-2, each generating one or more data products (Wingham et al., 2006).

The initial product is termed level-0 data and is the telemetered data from the satellite. The level-0 processor is responsible for decoding the telemetry, converting it into engineering units (Watts, seconds, meters, for example) and to apply for applying instrument corrections. The processor also performs the echolocation of the surface return and estimates atmospheric corrections. The resulting product is termed level-1 or full-bit-rate (FBR) product. For the SARin and SAR mode the echo's are ordered along-track according to their time. The pulse limited echo's in the LRM mode contain only the average waveform for each position.

The level-1b processor used for the SAR/SARIn modes takes as input the level-1 product and uses this to estimate the multi-looked echos. This includes pulse compression, synthetic beam forming, and power (SARIn) and phase

multi-looking. This processing stage is omitted for the pulse-limited echo's and the level-1 is passed along to the next step.

The final step is refereed to as level-2 processing and its function is the retrieval of surface height, given the input from the level-1 products for each mode.

6.3 Accessing and reading CryoSat-2 data

This section describes the procedure and software used to download, read and extract the ESA CryoSat-2 data products. These products are then used for the L1b processing and to extract the ESA processed surface heights.

6.3.1 Data description

CryoSat-2 data is freely available for any user, via a registration procedure, and can be downloaded via FTP: *ftp://science-pds.cryosat.esa.int*. The data is constantly being reprocessed to improve the overall quality, which is referred to as different baselines. An alphabetic index is used to indicate the latests version of the baseline (Baseline-A, Baseline-B and so on). The current baseline available from ESA is the "Baseline-B" product. This is also the product used for this study until "Baseline-C" becomes available in the end of 2014 or early 2015.

The baseline data product consists of two files: (1) the XLM header file ".HDR", containing auxiliary/meta-information and (2) and the binary product file ".DBL", containing measurement data and corrections for the different modes. Each "DBL" file corresponds to one ground track acquired during a specific time period. The ".DBL" files also contains both 1 and 20 Hz ground track sampling.

6.3.2 Downloading CryoSat-2 data

For this thesis we use both the L1b and L2 data products available on the ESA server are used. A python routine was developed to download the files from the ESA server. The routine makes use of the infrastructure built by Lars Stenseng (DTU Space) where all the ESA CryoSat-2 header-files are read weekly and indexed to a index-file. This index file then contains the download path, acquisition time, geographical information and other useful meta-data. To download

the data the index file, in conjunction with a geographical bounding box and a desired time-span, is given as input to the routine.

6.3.3 Reading CryoSat-2 data

The L1b and L2 data are read using two MATLAB functions (Cryo_L1b_read.m for L1b and Cryo_L2_read.m for L2 data) developed by ESA, which can be downloaded at: *https://earth.esa.int/web/guest/software-tools/-/article/cryosat-matlab-routines*. MATLAB scripts have then been developed to read and extract the desired parameters needed for the L1b processing and L2 data for the LRM and SARIn mode. The user can choose to extract both 1 or 20 Hz data for the LRM or SARIn mode, given the application of the data.

7 Gridding of scattered observations

This section present and discusses the two different techniques used to grid scattered observations onto a regular space grid. The gridding procedure is performed to allow for the determination of elevation and elevation change products, i.e such as DEMs.

The resampling of scattered data onto a regular grid has many advantages, as it allows for easier determination of volume and mass change estimates, analysis of spatial patterns, data compression and the possibility of using standard signal and image processing techniques for filtering and data analysis. It also allows for the estimating of Digital Elevation Models (DEMs) and other parameters such as the local surface slopes and aspect the Ice Sheet.

The choice of different interpolation or extrapolation algorithm can have profound influence on the estimated results. (Nilsson et al., 2015a) showed that the choice of algorithm used to grid surface elevation change had a significant effect on the total mass balance of ice cap and glaciers in the Arctic.

The initial Section 7.1 describes the algorithm used to interpolate the CrySat-2 surface heights onto a geographical grid using bi-quadratic surface modelling. Section 7.2 described the algorithm used to merge and interpolate different types of surface elevation changes by the means of least-squares collocation. The justification of the choice gridding algorithm is also provided in each section.

7.1 Bi-quadratic surface modelling

The CryoSat-2 surface elevations are interpolated onto a regular spaced grid by the means of local bi-quadratic surface modelling, which have been proven to work well for DEM generation (Zwally et al., 1990). This algorithm is inspired by the algorithm used by (Zwally et al., 1990) to generate a Greenland DEM from SEASAT, and has also been used to generate the ICESat Greenland DEM (DiMarzio et al., 2007). It is therefore believed that this methods will perform well for the purpose of DEM-generation.

The algorithm uses a variable search radius R around every prediction point (or grid node) to fit the surface heights to a bi-quadratic model using least squares minimization. Where the bi-quadratic surface model is defined as from

follows (Zwally et al., 1990)

$$\begin{aligned} H(\lambda,\phi) &= C_1 + C_2\frac{(\lambda-\lambda_i)}{D} + C_3\frac{(\phi-\phi_i)}{D\cos(\phi_i)} \\ &\quad + C_4\frac{(\lambda-\lambda_i)(\phi-\phi_i)}{D^2\cos(\phi_i)} + C_5\frac{(\lambda-\lambda_i)^2}{D^2} \\ &\quad + C_6\frac{(\phi-\phi_i)^2}{(D\cos(\phi_i))^2} \end{aligned} \tag{7.1}$$

where λ and ϕ is the longitude and latitude of the data inside the search radius, λ_i and ϕ_i is the longitude and latitude of the grid node, and D is the cap-size of the data inside the search radius ($D = \lambda_{max} - \lambda_{min}$). Here λ_{max} and λ_{min} are the longitudinal limits of the data inside the cap.

The system of linear equations are solved by an iterative distance-weighted least squares minimization. The system is solved by the means of Cholesky decomposition, where the solution to the system can be generalized mathematically as follows.

$$\hat{x} = (A^T W A)^{-1} A^T W y \tag{7.2}$$

where A is the design matrix containing the partial derivatives of Eq. 7.1, W is the distance weighting matrix, y are the height observations and $\hat{x}$ the estimated model coefficients.

Cholesky decomposition is used to determine the quality of the solution, i.e to determine rank deficiency. If its determined that the solution is rank deficient the search radius is increased and and the solution is re-evaluated. In the fitting procedure a weight W is assigned to each observation inside the cap, according to.

$$W = \frac{1}{1 + \left[\frac{D}{D_c}\right]^2} \tag{7.3}$$

where D is the distance from the prediction point to all other points inside the search radius, D_c is a resolution or correlation factor (usually set to the grid-resolution). The use of this function also secures that the weights never becomes undefined, as division with zero is not possible. The weighting is applied to preserve the local surface details that would otherwise be destroyed during the fitting process, due to the smoothing process, and also to lend greater importance to data closer to the grid node.

In the fitting routine the solution is iterated continuously to identify and remove outliers to improve the overall solution. This is done by computing the

residuals e between the observations H and the model $A\hat{x}$, according to:

$$e = H - A\hat{x} \tag{7.4}$$

The outliers are then identified and removed if any weighted residuals are larger than 3σ, using the following criteria.

$$|We| >= 3\sqrt{\frac{1}{N_i}(e^T We)} \tag{7.5}$$

where N_i is the number of data used in the fitting procedure (around every grid point). A maximum of 5 iterations are used to identify and remove outliers or until no more outliers can be identified.

The standard error $\hat{\varepsilon}$ of the individual model coefficients is then estimated from the scaled covariance-matrix, where the diagonal elements correspond to the uncertainty or standard error of each coefficient.

$$\hat{\varepsilon}^2 = \sigma^2 (A^T W A)^{-1} \tag{7.6}$$

where σ^2 is the variance of the residuals.

Once the standard error and the surface height initially have been estimated a screening procedure is applied. If the σ_{fit} is larger than 25 m or if the estimated elevation is negative a bilinear fit is instead applied, and if the bilinear fit does not improve the solution the elevation is declared invalid and the search radius increased. The search radius is increased and the fitting re-evaluated until a maximum search distance is reached (provided by the user). If no valid solution can be found at the maximum search distance the solution is declared invalid and set to NaN.

A minimum of 10 observations is required by the fitting algorithm to solve for the model coefficients, if the cap contains less than 10 observations the search radius is increased.

The algorithm outputs four parameters: (1) the estimated surface height $H = C_1$ (2) the standard error of the fitting procedure (3) the number of observations used in the fitting procedure and (4) a flag indicating rank-deficient solutions.

7.2 Least Squares Collocation

A detailed study of different interpolation and extrapolation algorithms for the purpose of deriving regional elevation change over glaciated terrain was

undertaken by (Nilsson et al., 2015a). The result of this study showed that least-squares collocation is good choice for the estimation of gridded elevation changes. The method also allows for both data-fusion and error estimation of the gridded product.

Least-squares collocation (Moritz, 1978) (also known as optimal estimation) can be used interpolate and merge different types of data-sets estimated from different methods. It is a linear, unbiased estimator, which can be used to interpolate inhomogeneous sparsely distributed data onto a regular spaced grid. The method uses the spatial correlation between the data and prediction point to weight the data, which makes it closely related to Kriging (Moritz, 1978).

The estimated cross-covariance C_{xy} between the prediction point and the measurements and the auto-covariance C_{xx} between the measurements, as a function of distance, are used to predict the value at the grid point location. This approach assumes that the observational data is error-less, which is certainly not the case in altimetry. To account for this random errors N can be added to the diagonal elements of the auto-covariance matrix.

The solution to the system, seen in Eq. 7.7, provides the best unbiased linear estimate in a least squares sense that minimizes the estimated error. This is also referred to the Wiener-Kolmogorov prediction formula used from stochastic processes.

$$\hat{y} = C_{xy}(C_{xx} + N)^{-1}x \tag{7.7}$$

where $\hat{y}$ is the predicted value and x is the observations matrix.

For the purpose of this study a 2^{nd} Markov model is used to model the covariance, as implemented in the GRAVSOFT GEOGRID routine (Forsberg and Tscherning, 2008). This model was chosen by convenience as it has been known to work well with many types of different geophysical data sets (Forsberg, 1984). The modelled covariance here depends on the overall variance of the observational data set C_0 changing as a function of distance r.

$$C(r) = C_0\left(1 - \frac{r}{\alpha}\right)\exp\left(-\frac{r}{\alpha}\right) \tag{7.8}$$

where α is the correlation distance, determined empirically from the observations.

The prediction error $\hat{\varepsilon}$ for each grid point can be determined using the following relation:

$$\varepsilon^2 = C_0 - C_{xy}(C_{xx} + N)^{-1}C_{xy}^T \tag{7.9}$$

Least-squares collocation was chosen for its many advantages, where the

main advantages is the ability to merge different datasets. It provides a comprehensive and simple way to merge different data set in mathematical optimum way, using there a-priori error estimates which are added as random errors in the matrix N. Therefore it was a clear choice to use for merging the estimated surface elevation changes produces form the two elevation change methods, described in Section 9.

The main disadvantage of the technique is that the solution requires the solution of a number of linear equations equal to the number of unknowns, in the form of inverting the $(C_{xx} + N)$ covariance matrix. This is highly impractical and for that reason a four-quadrant nearest neighbour search is performed to find the N-closest data points inside every quadrants around the prediction point to reduce computation time. The four-quadrant search approach is applied to reduce clustering effects, hence to gain symmetric data coverage around the prediction point.

Another requirement from the least squares collocation theory is that data used for the prediction need to have mathematical expectation zero. Hence all data-sets that includes local surface trends, like the topography of an ice sheet, needs to be de-trended (reduced to zero mean). This requires some a-priori knowledge of the surface trends. gained from i.e another DEM or trend analysis, used to compute surface residuals which are then interpolated. The updated surface is then recovered by adding back the trend surface. This is referred to as the remove-restore technique (Forsberg, 1984).

8 Surface elevations from CryoSat-2

The CryoSat-2 mission has been operational since late 2010 and has since then been providing surface elevation data in the form of the ESA L2 product. However, due to its new and novel design the post-processing of the data has not yet yielded the quality needed for surface elevation change studies. Hence, a large part of this thesis has been devoted to developing new and independent processing chains for the CryoSat-2 LRM and SARin-mode, with the purpose of deriving robust and accurate surface elevation over land ice using the ESA's CryoSat-2 L1b product.

This section will present the two new and novel processors devloped for the LRM and SARin-mode for CryoSat-2, which have been fully validated over several regions in the Arctic. This section details the strategy and implementation of the two processors, especially designed for land ice monitoring. Here the choice of retracker for the two modes will be discussed and justified, this using a statistical comparison with other retrackers. Further the choice of the main parameter values in the processing will further be explained using a statistical comparison.

The structure of the different sub-sections reflect the order of the different steps in the processing, as to give the reader a feeling and understanding of when and how the different steps are implemented in the two processors.

8.1 Low Resolution Mode (LRM) Processor

The section presents the implementation and development of the CryoSat-2 LRM-processor, made by the author. Here the different steps of the processors will be presented, and the choice of different methods and parameters discussed and justified. The processor consist of a threshold retracker, which has in previously studies proven effective for the derivation of robust elevation retrieval (Davis, 1997b). It further applies correction for the range error introduced by surface slope and effective filtering to reduce speckle noise in the CryoSat-2 waveforms. The input to this processor is the ESA L1b-product consisting of the needed parameters to derive the location and surface height of the measurements. For more information about the ESA L1b product please see (Bouzinac, 2014).

8.1.1 Waveform filtering

This section details the steps taken in the processor to deal with the effect and reduction of speckle noise, which is inherent to all radar measurements. The 20 Hz waveforms available from the the ESA L1b product are affected by speckle, which is considered for the purpose of this thesis as high-frequency noise. The speckle noise affects the precision and accuracy of the estimated surface elevation, as it degrades the waveform shape. To reduce the magnitude of the speckle noise low-pass filtering is applied to the waveform. Ordinary low-pass filtering has unfortunately the effects of introducing a signal delay into the smoothed data, which introduces an unwanted range error. To avoid introducing a delay and to suppress the speckle noise a zero-phase low-pass filters is applied to the waveform. A fourth order zero-phase low-pass filter is used to smooth the waveforms with a normalized cut-off frequency of 0.5. The filter order and cut-off frequency was determined using a large subset of different waveforms and visually inspected to determine the quality of the filtering, as over-smoothing of the waveform would cause a loss of both precision and accuracy. The waveforms was filtered on a line-by-line basis, meaning that operation was performed on every waveform. Figure 8.1 illustrates the low-pass filtering of a ordinary LRM waveform for the purpose of speckle reduction

8.1.2 Threshold retracker

To derive CryoSat-2 surface elevations over the relatively flat interior areas of the ice sheets, a threshold retracker was developed, adopting (Davis, 1997b) methodology. A threshold retracker is a statistical retracker that uses the statistics of the waveform to determine the range to the surface. The range to the surface is determined by applying a pre-defined threshold to the maximum amplitude of the waveform, where the range-value at this threshold level is said to correspond to the range to the surface.

The choice of threshold is important, as it has been shown to reflect different properties of the scattering regime and the robustness of the elevation retrieval. (Davis, 1997b) argued that a 20% threshold would represent the best compromise between waveforms that are entirely dominated by either volume or surface scattering, which making it suitable for obtaining first-order estimates of surface elevation for most parts of the Greenland ice sheet.

Hence, a 20% threshold retracker was chosen for the LRM-mode, as the return waveform of the interior higher elevation areas of the Greenland Ice

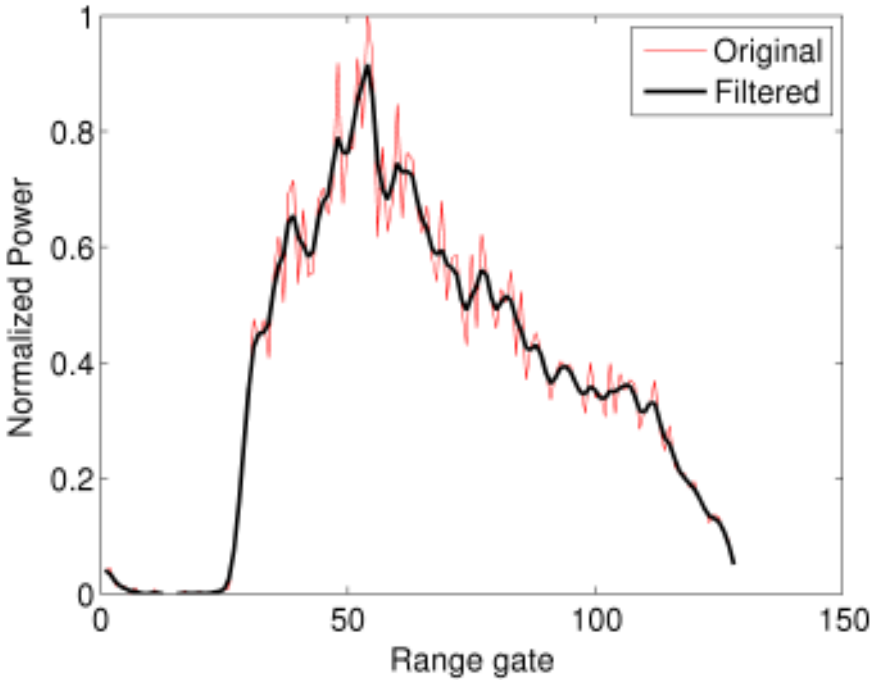

Figure 8.1 Low-pass filtering of a LRM waveform for the purpose of speckle reduction.

Sheet are mostly affected by both volume and surface scattering. This due to that most of the upper parts of the strata of the interior parts of the ice sheets consist mostly low density firn (350-450 kgm$^-$3), in combination with yearly forming ice layers and crystal boundaries, especially for the Greenland Ice Sheet.

To obtain the surface elevation the retracker procedure consist of several steps. The first step of the retracking procedure is to estimate the noise-level or the DC-bias of the waveform P_N by taking the mean value of the 5 first unaliased samples of the waveform.

$$P_N = \frac{1}{n} \sum_{n=1}^{n} P_i \tag{8.1}$$

where P_i is the power at the individual range bins and n is the number of unaliased bins. The number of unaliased bins are for the LRM-mode set to n=5, but depends on the size of the range gate window. The second step is to compute the maximum power P_{max} of the waveform. From these two parameters we compute the "Signal-to-noise" ratio (SNR) of the waveform and

use this to classify and reject bad waveforms. The rejection level for the SNR is currently set to 5 dB to avoid noisy or loss of track waveforms. The choice rejection level is discussed in more detail in Section 8.3.2.

$$SNR = 10\log_{10}\left(\frac{P_{max}}{P_N}\right) \tag{8.2}$$

The third step is to identify the leading edge of the smoothed waveform, meaning the first major peak. This is done by applying a peak-finding algorithm which searches for peaks larger than the mean power of the waveform (to avoid detecting low-power peaks before the leading edge). To avoid detecting small peaks, still left after the smoothing procedure, the waveform is over-smoothed. The over-smoothing has the effect of reducing small-scale topographic noise, but keeping the main surface returns inside the footprint intact. If no peak can be detected in the waveform it is rejected and no further processing is done. Once all peaks in the waveform have been detected, according to minimum peak criteria, the first peak of the waveform is selected and assumed to correspond the the leading edge.

The leading edge is then extracted from the waveform, using the peak index estimated from the over-smoothed waveform. The leading edge is extracted to avoid that the algorithm tracks or processes other parts of the waveform. The power values from the zero gate to the peak-gate value then defined as P_{LE}. The leading edge of the smoothed waveform is then oversampled by a factor of 10, using linear interpolation. This is done to introduce more samples into the leading edge, which usually do not have many samples due to the rapid rise time of the leading edge and the number of limited range gates. The maximum amplitude A is then computed from the extracted leading edge.

$$A = \max(P_{LE}) \tag{8.3}$$

The threshold power level P_{TL} is then estimated according to (Davis, 1997b)

$$P_{TL} = P_N + \alpha(A - P_N) \tag{8.4}$$

where α is the percentage of the the amplitude of the leading edge above the noise level. The precision of the retracking point is further enhanced by linearly interpolating between the two adjacent bins of the threshold using:

$$G_{RT} = (G_{TL} - 1) + \frac{P_{TL} - P_{G_{TL}-1}}{P_{G_{TL}} - P_{G_{TL}-1}} \tag{8.5}$$

where G_{TL} is the location of the first range bin exceeding the threshold level. If $P_{G_{TL}} = P_{G_{TL}-1}$ the retracking location is set to $G_{RT} = (G_{TL} - 1)$.

Finally the corrected range R to the surface can be estimated according to (Bouzinac, 2014)

$$R = 0.5 \cdot c \cdot W_{delay} + R_b(G_{RT} - 64) + C \tag{8.6}$$

where c is the speed of light, W_{delay} is the window delay, R_b range bins size (0.4684 m for LRM) and C sum of the range corrections for land ice (Bouzinac, 2014), available in the L1b product.

8.1.3 Range correction for slope-induced error

As described in Section. 4.3.6 (over sloping surfaces) the return of the radar signal does not originated from the nadir location of the satellite, but instead from the POCA which is located at a location up-slope.

To correct for the slope induced error (Bamber et al., 1998; Brenner et al., 1983) method is used to correct the measured range to the nadir position using an external Digital Elevation Model (DEM) named GIMP (Howat et al., 2014). The local surface slope of the DEM is then computed which is then median filtered to remove arbitrary spikes, caused by the slope generation algorithm. The filtered slope model is then resampled to a resolution of ∼10 km. From the re-sampled DEM the local slopes α are computed for each measurement location using bilinear interpolation. The corrected range R_c at the nadir position is then is then estimated using the local slope interpolated to each measurement location, according to:

$$R_c = \frac{R}{\cos(\alpha)} \tag{8.7}$$

where R is the measured range to the surface (up-slope) and α is the local surface slope in radians.

The re-sampling of the DEM can be justified by noting that the magnitude of the horizontal displacement can easily reach upwards 10-15 km, as discussed in Section. 4.3.6. This means that local undulations of surface slope can have a profound effects on the corrected range. Resampling the DEM to a resolution comparable with the beam-limited footprint produces an average slope inside the footprint, reducing the effects of local topographical undulations.

However the main governing factor of the accuracy of the corrected range is the DEM used for the determining the local slope. Hence one should use a the best possible DEM available, as the choice of DEM has a direct effect on the accuracy of the observations.

8.2 Interferometric SAR (SARin) Processor

This section details, as with the LRM processor, the development and implementation of the CryoSat-2 SARin-mode processors, made by the author. This processors is especially designed for robust and accurate elevation retrieval over highly complex glacial terrain over the high-sloping marginal areas of the ice sheet and ice caps. It is especially designed to reduce phase ambiguities and phase noise, allowing for more accurate mapping of the location of the surface return. The processors further has been equipped with a new and novel retracking approach, designed to increase precision compared to the common threshold retracker.

As for the LRM-mode the processors input consists of the ESA L1b product, which consist of the needed parameters to derive surface height and mapping of the return echo. For more information about the ESA L1b product please see (Bouzinac, 2014).

8.2.1 Waveform filtering

The waveform filtering procedure employed in the SARin processors is equal to the one used in the LRM processor, with two major differences (1) the filter length has been increased to eight (2) the normalized cut-off frequency has been lowered to 0.1. These changes have been made because the SARin range gate window is four times larger than the LRM, which requires a larger filter to obtain the same speckle reduction capabilities. The SARin waveform are also more noisy in nature comparing to the LRM waveforms, requiring a lower cut-off frequency. The magnitude of these two parameters have been determined by visual inspection of a large number of waveforms, as it was done in the LRM processing. Figure 8.2 illustrates the low-pass filtering of a ordinary SARin waveform for the purpose of speckle reduction.

8.2.2 Coherence filtering

The coherence is estimated from the stacking procedure, which is described in Section. 4.3.3, gives and indication on how similar the waveforms inside stack. A low coherence indicates that there are large variations in the shape and power of the waveforms inside the stack, and that the derived stacked waveform might not be usable for determining surface heights. The initial step in the coherence filtering is to set all coherence values larger than one to zero,

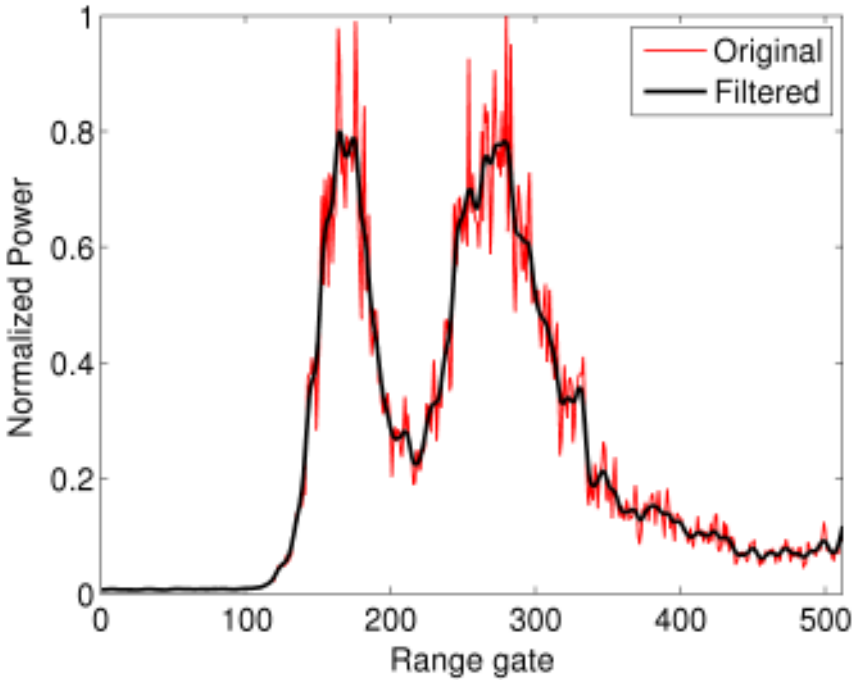

Figure 8.2 Low-pass filtering of a SARin waveform for the purpose of speckle reduction.

as the coherence C is defined from 0 <C< 1 (values larger than one exists in the L1b product, which origins are unknown). The coherence parameters has the shape of a N×512 array and to de-noise this array a 2D Wiener filter is used with a 5×5 filter window. The main reason for filtering the coherence is the future creation of the interferogram, and will be discussed more Section. 8.2.3. Several different methods of filtering the coherence has been tested and it was found, by examining the "Peak-Signal-to-Noise-Ratio" (PSNR), that the wiener-filtering approach gave the best results, in the form of highest PSNR. The PSNR is defined according to

$$MSE = \frac{1}{NM} \sum_{i=0}^{M-1} \sum_{j=0}^{N-1} ([F(i,j) - O(i,j)]^2) \tag{8.8}$$

where F is the filtered array and O is the original array containing noise. The $PSNR$ is then computed according to

$$PSNR = 10 \log_{10} \left(\frac{MAX^2}{MSE} \right) \tag{8.9}$$

where MAX is the maximum value of the two dimensional array.

8.2.3 Phase filtering

CryoSat-2 does not only measure the range to the surface it also measures the phase difference between the transmitted and return signal, using its two antennas. The measured phase difference, or the differential phase is used to determine the echo location of the measured surface and is thus as an important as the waveform retracking, which provides the surface heights. The noise in the differential phase has a direct impact on both accuracy and precision of the measurement, as the noise propagates into the position estimate of the POCA location.

Phase filtering is therefore needed to reduce the noise in the measured phase and to ensure a more robust estimation of the POCA location. However, one of the main issues with filtering the differential phase is that it is commonly affected by phase wrapping, a sudden change of $\pm 2\pi$ (as discussed more in Section 8.2.4), causing sharp discontinuities in the phase. This makes the phase difficult to filter directly, here (Gray et al., 2013) approach has been adopted to over come this problem, where the interferogram is recreated then consequently filtered, as its not affected by the phase wrapping.

The interferogram ψ is recreated from the phase $\Delta\phi$, power P and the coherence C according to:

$$\psi = P \cdot C \cdot \exp\left(-j\Delta\phi\right) \tag{8.10}$$

Here is becomes apparent why filtering of the coherence was performed, as noise in the three parameters map directly into the interferogram. To overcome this problem a wavelet denoiseing strategy was employed, because wavelets have the ability to map noise at different scales and time, making it a far more effective tool for removing noise than linear filters in this case. Wavelet filtering also has the advantage of preserving signal dynamics, as the noise is mapped at different scales, compared to ordinary low-pass filtering which has a tendency sometimes to remove much of the dynamical components of the signal.

The theory of wavelet filtering will not be discussed in detail here, for more detailed information see i.e. (Gonzalez et al., 2004). The wavelet filtering strategy and procedure is described in the following steps here.

- A bi-orthogonal was chosen as the mother wavelet (bior2.6 in MATLAB) to produce the wavelet coefficients decomposed into three levels.
- Soft thresholding was applied to detail coefficients, using a heuristic threshold rule to remove noise at every level.

- Inverse wavelet transform was then performed to recover the filtered signal

The wavelet filtering algorithm used for this processor is implemented in MATLAB, as the *"wden"* function. The filtering was performed, as with the waveform filtering, on a line-by-line basis by filtering the real and imaginary component of the interferogram. The filtered interferogram was then recreated by adding the real and imaginary part together.

$$I = \mathrm{Re}\{I\} + j \cdot \mathrm{Im}\{\mathrm{I}\} \tag{8.11}$$

The final filtered phase is then recovered by solving for the $\Delta\phi$ in Eq. 8.10.

8.2.4 Phase unwrapping

Phase wrapping occurs when there a sudden shift of $\pm 2\pi$ added to the phase causing the ground track to suddenly shift from one side of the nominal track to the other, hence putting the right height in the wrong position. Whole tracks or individual points can be shifted, causing an incorrect determination of surface height at the specific location.

The filtered phase is therefore unwrapped to remove this effect, by simply locating the jumps of 2π and adding or subtracting 2π to all the following elements in the vector, depending on the sign of the phase. There are many other more advanced techniques to perform phase unwrapping in the presence of noise. However, as large efforts already have been put into remove noise from the phase this simple (but effective) method gives satisfactory results.

The phase is then unwrapped from a central region close to the maximum peak of the waveform, where the coherence usually is high $\sim$0.7, in both directions. The start position of the unwrapping is defined from the center of gravity of the waveform, using the OCOG retracker (Vignudelli et al., 2011). Where the center of gravity (COG) of the waveform is determined using the following function.

$$COG = \frac{\sum_{i=1}^{N}(iP_i^2)}{\sum_{i=1}^{N}(P_i^2)} \tag{8.12}$$

where P_i is the power at the individual range gates or bins and (i) is the range gate index (1-512 for SARin). The phase unwrapping is as the waveform filtering performed on a line by line basis.

8.2.5 Maximum gradient retracker

The power distribution of the waveform in a Doppler/Delay system show an important distinction from conventional pulse-limited systems, as earlier described in Section. 4.3.3. In a Doppler/Delay the point on the echo, that correspond to the mean surface, does not lie at the half-power point of the leading edge, but rather somewhere closer to the maximum (Wingham et al., 2006). The shape of the return waveform, processed using Doppler/delay technique, also differs from conventional pulse-limited altimetry. Here, as the resolution is higher, multiple surface may be present inside the footprint producing several distinct peaks in the waveform. This is in contrast to pulse-limited systems, where waveforms mostly consists of one major peak, corresponding to the mean surface inside the much larger footprint.

As the mean surface of the SARin waveform is located closer to the maximum of the leading edge, in the usually more noisy or variable parts of the waveform, a new type of retracker has been developed in this study. The new retracker is refereed to as the **maximum gradient retracker** and tracks the maximum gradient of the leading edge (the first peak) of the waveform. This allows for adaptive tracking of the retracking point, assuming that the maximum gradient corresponds to the mean surface return, which is more favourable. The maximum gradient of the SARin waveform can be found in the upper part of the waveform close to the maximum and would correspond to a threshold of roughly 80% for a threshold retracker.

The maximum gradient retracker share many aspects with the threshold retracker, such as noise power estimation, identifying the leading edge of the waveform and rejection parameters. Hence, these steps will be quickly explained and for more details please see Section 8.1.2. Initially, the noise power is estimated for estimation of the DC-bias, as in the threshold retracker, but in contrast to the threshold retracker the DC-bias is removed according to

$$P_{i,c} = P_i - \frac{1}{n}\sum_{i=1}^{n} P_i \tag{8.13}$$

where $P_{i,c}$ is the power corrected for the DC-bias, P_i is the power in every range bin and n is the number of unaliased range bins. Once this has been done the peak finding procedure is performed, in the same manner as for the threshold retracker, and if no peaks are found or if the SNR is to low (SNR threshold set to 5 dB) the waveform is rejected.

If the waveform has passed these main editing criteria the leading edge is extracted, in the same manner as with the threshold retracker, and the range

gate position of the maximum gradient is estimated.

$$\frac{\delta P}{\delta R} = \max(\nabla P_{LR}) \tag{8.14}$$

where ∇ is the gradient operator, P_{LR} is the power values of the leading edge and $\frac{\delta P}{\delta R}$ is the value of the maximum gradient of the leading edge.

The position of the maximum gradient is then used to extract a segment of power values centred around the range gate location of the maximum gradient (± 5 points). The estimated range gate G_{RT} of the maximum gradient is then refined by over-sampling the segment with a factor of 100, using linear interpolation, and then the value of the maximum gradient value is re-computed. The refined range gate value G_{RT} is then used to estimated the range to the surface according the Eq. 8.6

$$R = 0.5 \cdot c \cdot W_{delay} + R_b(G_{RT} - 256) + C \tag{8.15}$$

where for the SARin mode $R_b = 0.2342$ m.

The refined value is then used to estimate the phase and coherence value at the corresponding range gate location, also using linear interpolation. If the estimated coherence value at the estimate range gate is $C < 0.8$ then the POCA point is rejected.

8.2.6 Geocoding of surface echos

The geocoding procedure is done to determine the position of the return echo on the surface, and is one of the most important steps in the interferometric processing. This as it has a direct bearing on the accuracy and precision of the measurements. The location of the across track echo is determined from the differential phase $\Delta\phi$, thereof the high emphasis on the phase filtering, and is used to compute the across track look angle θ_L.

$$\theta_L = \sin^{-1}\left(\frac{\Delta\phi}{kB}\right) - \beta \tag{8.16}$$

where k is the wavenumber, B the length of the antenna baseline and β the satellite roll angle (Wingham et al., 2006).

The look angle θ_L and the azimuth A (estimated from the North) is then used to construct a line of sight local satellite based (E,N,U) coordinate system. Where E is the east component, N is the north component and U is the up

component of the system. As the SIRAL system and its antennas have a broadside configuration 90° needs to be added to the azimuth.

$$E = \sin(\theta_L)\sin(A+90) \quad (8.17)$$
$$N = \sin(\theta_L)\cos(A+90) \quad (8.18)$$
$$U = -\cos(\theta_L) \quad (8.19)$$

The locally based satellite coordinate system is then projected to the Earth-based system, by computing the unit vectors (u_x,u_y,u_z) of the local system, expressed in a "Earth Centred Earth Fixed" (ECEF) Cartesian coordinate system.

$$u_x = -E\sin(\lambda) - N\sin(\phi)\cos(\lambda) + U\cos(\phi)\cos(\lambda) \quad (8.20)$$
$$u_y = E\cos(\lambda) - N\sin(\phi)\sin(\lambda) + U\cos(\phi)\sin(\lambda) \quad (8.21)$$
$$u_z = N\cos(\phi) + U\sin(\phi) \quad (8.22)$$

where λ is the longitude of the satellites nadir position and *phi* is the latitude of the satellites nadir position.

The satellites geodetic coordinates and altitude is then converted into the same ECEF-coordinate system as with the local satellite-based (E,N,U) system, and the echo-location is found by multiplying the unit-vectors with the range R to the surface.

$$x_e = R \cdot u_x + x_n \quad (8.23)$$
$$y_e = R \cdot u_y + y_n \quad (8.24)$$
$$z_e = R \cdot uz + z_n \quad (8.25)$$

The geodetic coordinates and surface elevation is then recovered by an inverse transformation of the of the ECEF-coordinates (x,y,z). This algorithm was provided by Dr. Laurence Gray (University of Ottawa, Ottawa, Canada), with minor modifications made by the authors.

8.2.7 Phase ambiguity detection and correction

The phase unwrapping procedure is, as described in Section 8.2.4, a common technique for reducing phase ambiguities or discontinuities in the measured differential phase, by locating sudden shifts larger than 2π. Unfortunately the phase unwrapping procedure is not always successful in removing all phase ambiguities and thus still degrades the accuracy and precision of the measurements.

These residual phase ambiguities can be detected and corrected for by using external data. An external DEM can be used to detect and flag ambiguous measurements, by noting the simple criteria that over a sloping surface the surface return must always come from a up-slope position. This means that the height at the echo location must always be higher than at the nadir position, if not the point is almost certainly ambiguous. This means that a simple height criteria can be used to detect phase ambiguous measurements, according to.

$$H(\lambda,\phi)_{echo} - H(\lambda,\phi)_{nadir} > T \tag{8.26}$$

where $H(\lambda,\phi)_{echo}$ is the height at the echo position, $H(\lambda,\phi)_{nadir}$ is the height at the nadir position and T is a height ambiguity threshold. The height ambiguity threshold T is currently set to 15 m in the SARin processor.

The height criteria is applied to all measurements and if a phase ambiguity is found 2π is added or subtracted, depending on the sign, to the along-track phase estimate and the echo location performed again.

Further, to allow detection of phase ambiguities that might not be detected using the external DEM (the DEM might to coarse) a second procedure is applied using the along-track phase estimates themselves. The along-track phase values, estimated from the retracking procedure, can be assumed relatively stable or constant along the ground track, as (1) they follow the topography and (2) they passed the coherence test. Assuming that the along-track phase values do not vary largely across the ground track from point to point large sudden variations of the phase from one point to another would be indicative of a phase ambiguity. This assumption is tested by smoothing the along-track phase and computing the residuals between the original phase values and the smoothed values. If the any of the residual values is larger than a phase threshold, currently set to 1.5π, the original phase is corrected by adding or subtracting 2π and the geocoding is repeated.

However a drawback of this method is that it has a tendency to sometimes incorrectly flag and correct measurements, when there is low along-track density of points or if the assumptions of slowly varying phase is violated. To avoid these gross errors a running hampel-filter (Pearson, 2002) is applied to remove phase estimates that diverge more than 3σ from the median value inside the window.

8.3 Retracker evaluation and parameter tuning

The main purpose of this section is to discuss how the different retrackers for each mode was chosen, and also how the main parameters in the processing was selected to maximize accuracy, precision and data density. This was done using a statistical comparisons over two different test regions, one for each mode. It should be made clear here that a more detailed validation of the measurement uncertainty will be undertaken in the later Section 11.4. This section had the purpose of determining and discussing the choice of retracker and choice of processing parameters.

The Barnes ice cap, in the Canadian Arctic, was chosen as test area for the SARin processor, as this area was extensively surveyed using airborne laser scanner data in 2011. Other advantages of Barnes ice cap is its gentle topography and that it mostly consist of superimposed ice (personal communication with David Burgess, Geological Survey of Canada) which reduces surface penetration effects.

For the LRM processors, a 3°-by-3° degree bounding box centred around the North Greenland Eemian Ice Drilling (NEEM) camp at 77.45 °N and 51.06 °W, in the NW parts of Greenland, above 2000 m was used as a test area. This area was chosen due to its closeness to NEEM, where valuable in-situ snow stratigraphy data are available for the time period. CryoSat-2 data for the months of June and August 2012 was used for the statistical evaluation of the threshold retracker to determine the threshold parameter.

The months of June and August 2012 was also chosen as during the month of July 2012 there was an major melt event that affected over 98.6% of the Greenland ice sheet (Nghiem et al., 2012). This produced a near-surface melt layer that had the effect of shifting the reflective surface, seen by CryoSat-2, upwards nearly 50 cm. The presence of this melt layers was confirmed by in-situ observations at NEEM (snowpit measurements), which was manned during this time of the event. For more a more detailed study of the effects off the melt event on radar altimetry see (Nilsson et al., 2015b).

This event made is possible to judge the accuracy of the LRM observations without using airborne laser scanner data and also allowed for better temporal overlap, as the airborne campaigns are often only flown in the months of April and May. As the event produced a near-surface ice layer which was directly observed by scientists at NEEM (Nilsson et al., 2015b) it allows for a more direct determination of the surface penetration effect of the radar signal. This has been used in combination with satellite crossover analysis to determine the

accuracy and precision respectively for different thresholds.

8.3.1 Retracker evaluation

CryoSat-2 elevation data from the months of Feb-June in 2011 was used to compare with **NASA IceBridge Airborne Topographic Mapper** (ATM) (Krabill et al., 2002) derived laser elevations (http://nsidc.org/icebridge/portal) from April 2011, inside a search radius of 50 m. The longer time span of the CryoSat-2 data was used to derive enough comparison points for a robust determination of the statistics.

The difference of the two data sets where then used to derive the precision (standard deviation) and accuracy (mean-value) of two different CryoSat-2 retracker algorithms. The two algorithms chosen for the comparison were the threshold retracker, detailed in Section. 8.1.2, and the Maximum gradient retracker, detailed in Section 8.2.5. Table. 8.1 shows the derived accuracy and precision of the two retracker algorithms for Barnes ice cap, where the threshold retracker was run using several different thresholds. From Table 8.1 it

Threshold (%)	Mean (m)	Std.dev (m)	max (m)	min (m)
10	2.15	1.56	10.38	-2.32
20	1.00	1.10	11.56	-5.11
30	0.28	0.73	8.39	-3.53
40	-0.15	0.61	8.36	-5.50
50	-0.42	0.72	3.85	-5.46
60	-0.62	0.63	4.03	-3.54
70	-0.83	0.60	8.25	-7.41
80	-0.99	0.76	7.95	-4.86
90	-1.27	0.84	3.40	-3.92
Gradient	-0.35	0.47	2.05	-2.47

Table 8.1 Comparison of precision and accuracy of the maximum gradient retracker and the threshold retracker over Barnes ice cap in the Canadian Arctic, computed using IceBridge ATM laser scanner heights (April 2011) as reference and CryoSat-2 data (Feb-July 2011). Where the precision is defined as the standard deviation of the height difference and the accuracy as the mean value of the height difference.

can be seen that the Maximum gradient retracker performed better than the threshold-based retracker in precision and accuracy for most thresholds, for which 40% thresholds showed the largest accuracy but had lower precision and

higher spread. The main purpose of this study is to derive accurate surface elevation changes, which means that a robust retracker is needed. From this case study of Barnes ice cap it was concluded that the maximum gradient retracker gives superior results compared to the threshold retracker, and therefore the maximum gradient retracker will be used in the remainder of this study for the SARin-mode.

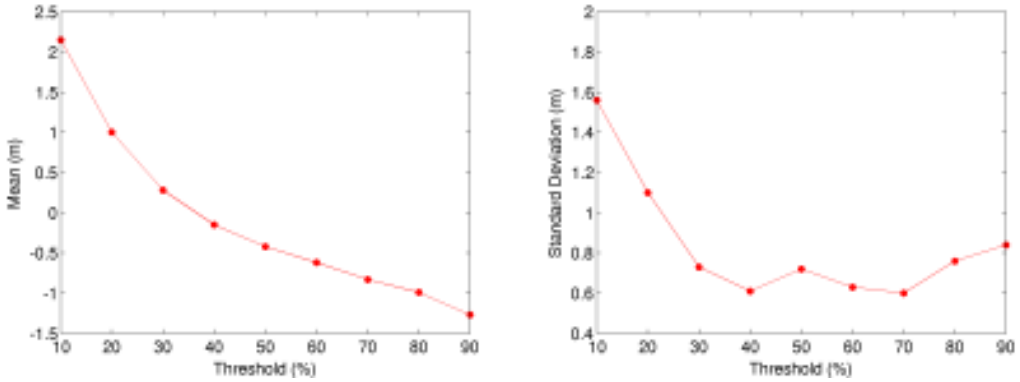

Figure 8.3 Accuracy (mean) and precision (standard deviation) of the SARin threshold retracker as a function of the leading edge threshold estimated over Barnes ice cap in the Canadian Arctic, using CryoSat-2 data for the months of Feb-Jun 2011 and IceBridge ATM for the month of April 2011.

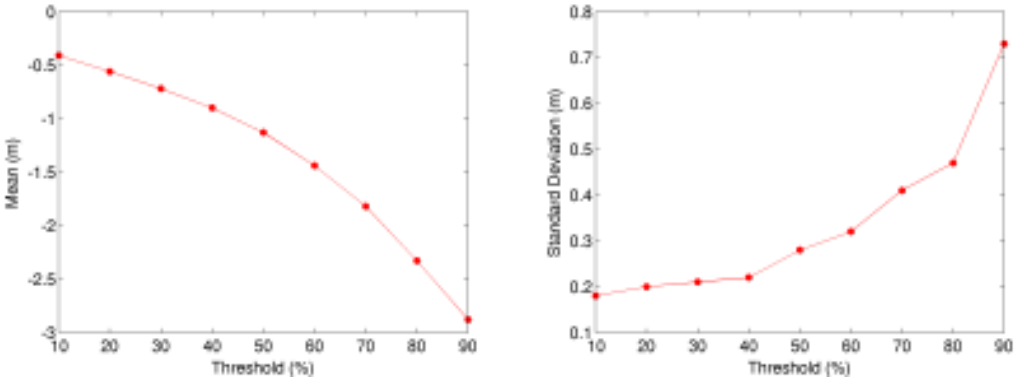

Figure 8.4 Accuracy (mean) and precision (standard deviation) of the LRM threshold retracker as a function of slope around the North Greenland Eemian Ice Drilling (NEEM) camp at 77.45 °N and 51.06 °W, in the NW parts of Greenland, in a 3°-by-3° degree bounding box. The accuracy was determined by estimating the bias between the month of June and August 2012 and the precision using satellite crossovers for the month of August.

The Fig.8.3-8.4 clearly shows the difference between pulse-limited and Doppler/delay altimetry. The precision derived from the SARin threshold retarcker, as a function of threshold, shows a clear inverse relationship compared to the LRM-mode. Where for the SARin mode the precision increases as function of threshold, where a clear breaking point is observed in the standard deviation at a threshold of 30%, seen in Fig. 8.4. This is clear contrast to the LRM-mode, where the best precision is found between the thresholds of 10-20%, in-line with the results obtained by (Davis, 1997b).

From these result and the arguments put forward by (Davis, 1997b) the 20% threshold seem like the clear choice of threshold for the LRM-mode. This as it gives the best overall accuracy and precision, as seen in Fig. 8.3, for waveforms affected by both surface and volume scattering. One should also observe if that if a threshold retracker is used for the SARin mode a threshold above or equal to 40% is recommended, as this gives the best possible precision and accuracy.

8.3.2 Parameter tuning

The main governing parameters that constrain the processing of the altimeter echoes is the SNR (LRM+SARin) of the waveform and the coherence (SARin). The settings of these values has an direct effect on both the precision and the data density (number of measurements) outputted from the processors.

The value of the SNR parameter is an important consideration for the total number of produced measurements. The SNR is the ratio of maximum return power of the waveform in relation to the estimated noise power. High SNR indicates that the received power is high in contrast to the noise power and hence of better quality.

In areas of steep and rough topography, as the SARin-mode operates over, the SNR of the waveforms will be reduced as sloping surface and rougher terrain will decrease the backscatter of the signal to the satellite. This in contrast to the LRM-mode that operates over the flatter interior parts of the ice sheet and will thus receive a larger part of the backscattered signal and have higher SNR. This means that the number of measurements in the stepper parts of the marginal areas will be reduced if the SNR is set to high. This is not preferable as these are the areas that currently is experiencing the largest rates of change and is thus of major interest to measure. However the SNR can not be set to low either as this will lower the precision of the measurements. The same argument can be applied to the coherence threshold level for the SARin

processor.

Low coherence indicates large variability of the waveforms inside the stacking pile and setting the coherence level to low will result in reduction of precision. While setting it to high will result in loss of measurements in the steeper and low elevation regions.

To allow us to determine the values of the SNR and the coherence a decision matrix (Table 8.2) was estimated, showing the precision and number of measurements as functions of the coherence and SNR. The decision matrix was determined using CryoSat-2 elevation data over Barnes ice cap in the Canadian Arctic for the months of Feb-Jun 2011, compared to IceBridge ATM laser scanner data from April 2011.

COH/SNR	1	5	10	20
0.70	0.63/5392	0.62/5362	0.61/5226	0.50/4573
0.75	0.60/5242	0.59/5213	0.59/5092	0.49/4466
0.80	0.54/5009	0.54/4983	0.50/4850	0.47/4286
0.85	0.50/4587	0.50/4566	0.48/4426	0.46/3961

Table 8.2 Parameter decision matrix for determining the values of coherences and SNR (dB) for the CryoSat-2 SARin processor, as a trade-off between measurement density and precision (in meters). The precision and data density was estimated over Barnes ice cap in the Canadian Arctic for the year 2011, using IceBridge ATM laser scanner height data as a reference.

From the results in Table 8.2 we have chosen to use the value of 10 dB for the SNR and a value 0.8 for the coherence threshold for the SARin processor, as this have the best trade-off between precision and data density. For the LRM processor a SNR threshold of 10 dB was also chosen.

8.4 Digital Elevation Model of the Greenland Ice Sheet

Digital elevation models of the ice sheets surface topography has a wide variety of applications for the scientific and non-scientific community. For the scientific community it has applications in areas such as numerical modelling, field planning, data processing and mass balance estimation. Due to its wide variety of applications it is not only important to have accurate topographical information, it is also important to have knowledge about the inherent errors in the estimated topography.

Though the main purpose of this study is to derive surface elevation changes of the Greenland ice sheet, there is no good reason not to produce a DEM in the process. This as the surface topography has already been estimated and is for the purpose of this this study a bi-product of the elevation change estimation procedure. A contemporary DEM estimated from CryoSat-2 observations is also of great value for further improvement of the CryoSat-2 surface elevations, as it can be used to correct for slope-induced error, for which purpose the DEM from (Howat et al., 2014) is currently used. It can also be used to in the process to determine elevation changes, i.e removing long-wavelength topography.

8.4.1 DEM generation

The surface topography of the Greenland ice sheet has been estimated using approximately four years of data (2010-07 to 2014-08) over the glaciated areas, determined from the KMS/GEUS (National Survey and Cadastre of Denmark) land-ice mask. The scattered observations was interpolated onto a regular grid with grid spacing of $0.01^\circ \times 0.025^\circ$ (latitude×longitude), using the method described in Section 7.1. Prior to the interpolation procedure both the LRM and SARiN observations where individually corrected for elevation biases, due to i.e surface penetration of the radar signal. The elevation biases where determined on a continental wide scale using multi-year airborne laser scanner height from ATM (Krabill et al., 2002) observations overlapping with CryoSat-2.

Post-processing of the generated DEM was done to detect any erroneous grid-values using a local outlier detection scheme. Outlier are detected using a local 20 km sub-grid around every grid-node and if any the elevation value at the grid-node exceeds 3σ of the surrounding elevations it is declared an outlier and set to NaN. The NaN-locations are then filled using inverse distance weighted interpolation (IDW), using the 20 closest data-points from the DEM. This procedure was iterated a total number of 5-times or until no more outlier

could be detected.The standard deviation and the number of values used in the prediction is outputted from the IDW-algorithm. Where the standard deviation is taken to be somewhat representative of the validity of the predicted value.

The IDW-interpolation method was used as it has the advantage that the estimated predicted values stays inside the bounds of the of the data (maximum and minimum value) used for the prediction.

The generation of the GrIS DEM can be summarized by the following processing and editing steps.

1. Apply the estimated elevation biases for the LRM (-0.46 m) and SARiN (-0.60 m) mode to the scattered surface elevation observations. Estimated from IceBridge ATM data from the 2011-2013 campaign and 5 months of CryoSat-2 (Feb-Jun) using a 50 m search radius. See Table. 11.3 and Table. 11.2 for bias values.

2. Grid observations onto a regular spaced grid of $0.01°\times0.025°$, corresponding roughly to 1 km resolution, using method described in Section 7.1. The following constraints are set for the interpolation procedure: $0<H<3300$ m and $\sigma_{fit} < 25$ m.

3. Apply KMS/GEUS ice-mask to the gridded data to extract ice sheet topography.

4. Identify outliers in the generated DEM, using a 20 km search radius. Set grid-value to NaN if declared an outlier.

5. Estimate new grid-values at the NaN-location using IDW-interpolation taking the 20 closest nonzero DEM-values around the prediction point

8.4.2 Final DEM product of the Greenland Ice Sheet

The estimated surface topography, topological error, slope and aspect of the GrIS can be viewed in Fig.8.5-8.8. The DEM in Fig. 8.5 was constructed using approximately 17.2 million surface height observations, covering a 4-year time span. Where the LRM-data consisted of ∼9.2 million surface heights and the SARin-data of ∼8.0 million surface heights.

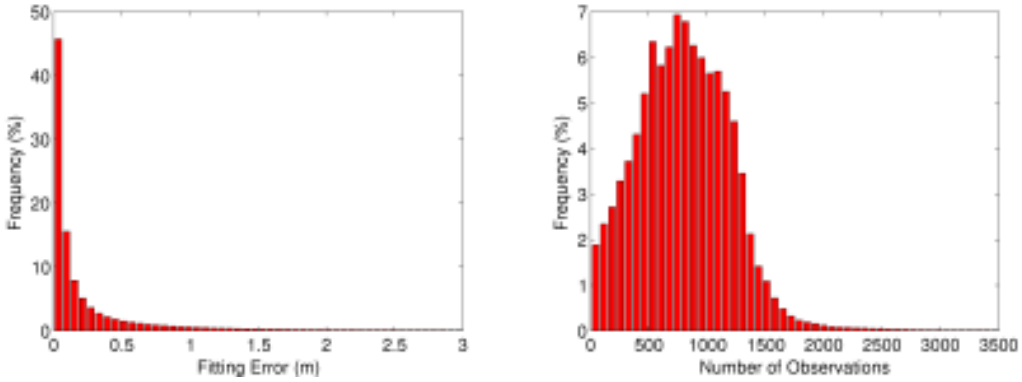

Figure 8.9 Show the DEM interpolation or fitting error (left) and the number of observations (right) that where used in the fitting process to solve for the surface topography.

Fig. 8.5 shows the estimated DEM for the GrIS topography for both glacial ice and the auxiliary ice caps on the coast of the continent. From the estimated topographical error (Fig. 8.6), estimated in the fitting process of the bi-quadratic surface, one can observe that the largest errors are found along the marginal areas of the ice sheet. This pattern is expected, as these areas will have the largest variations of elevations due to the steeper topography of these areas. The error is reduced when moving inland from the coast, as the topography becomes more gentle and surface slopes are reduced. The topographical error ranges from a decimetre level in the interior parts of the ice sheet and up to 25 m along the marginal coastal areas.

The estimation of surface slope of the GrIS show detailed and complex patterns of the driving stresses in the ice sheet. Features, such as the North-east ice stream is clearly visible in Fig. 8.7, and the anomalies in the surrounding basin. All major ice divides across the ice sheet are also clearly visible in great detail. Several new and old anomalies are also evident in the surface slope seen in Fig 8.7, where the surface anomaly found by (Ekholm et al., 1998) is clearly visible in the North-western parts of the ice sheet, at roughly 78°N and 48 °W. All major ice divides are also clearly visible delineating the different Greenland basins, more clearly seen in the surface aspect in Fig. 8.8.

The surface aspect, seen in Fig. 8.8, further shows the main features visible in the surface slope in Fig 8.7. Where all delineations of the major ice divides and basins become very clear in conjunction with other detailed topographical patterns. The most evident pattern is the North-east ice stream and its surrounding surface anomalies, showing a clear offset from the ordinary pattern of aspect in the region.

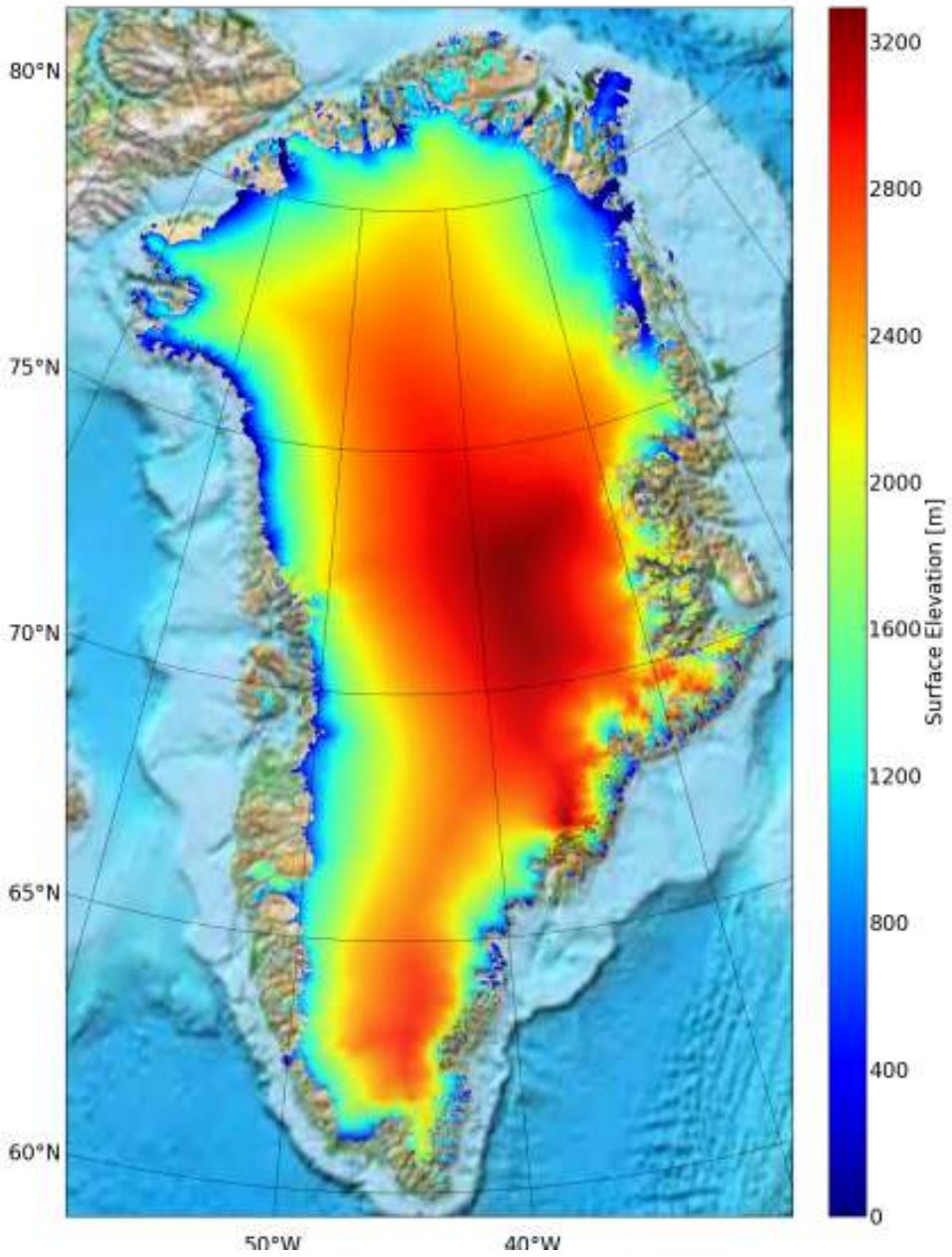

Figure 8.5 Surface topography of the Greenland ice sheet (in meters) estimated from approximately 4-years of CryoSat-2 data processed at DTU using the methodology described in this thesis.

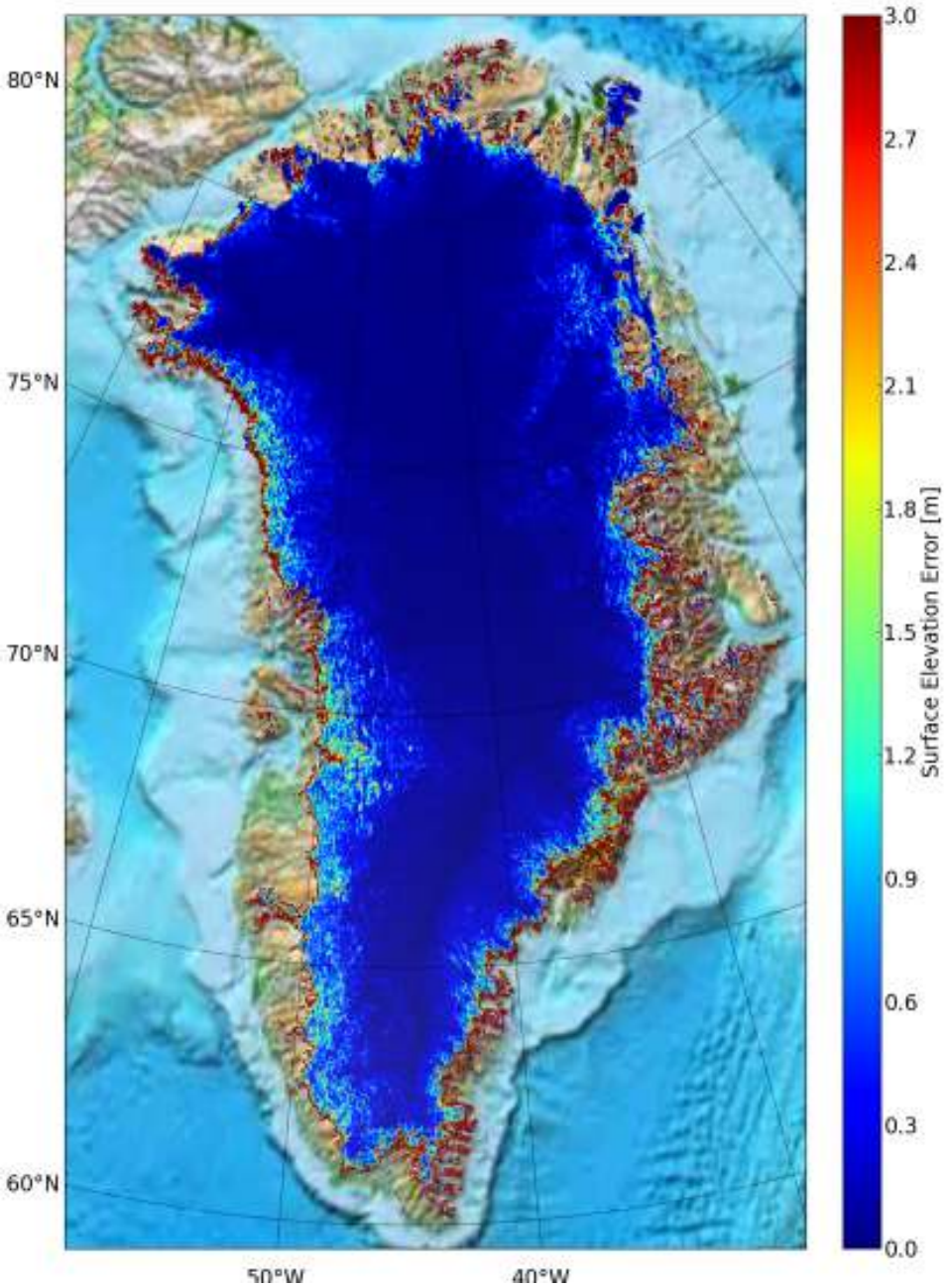

Figure 8.6 Topographical error (in meters) estimated from the interpolation/fitting procedure described in Section 7.1, showing the standard error. The figure show clearly a higher error in the marginal areas shrinking drastically moving inwards to the interior of the ice sheet.

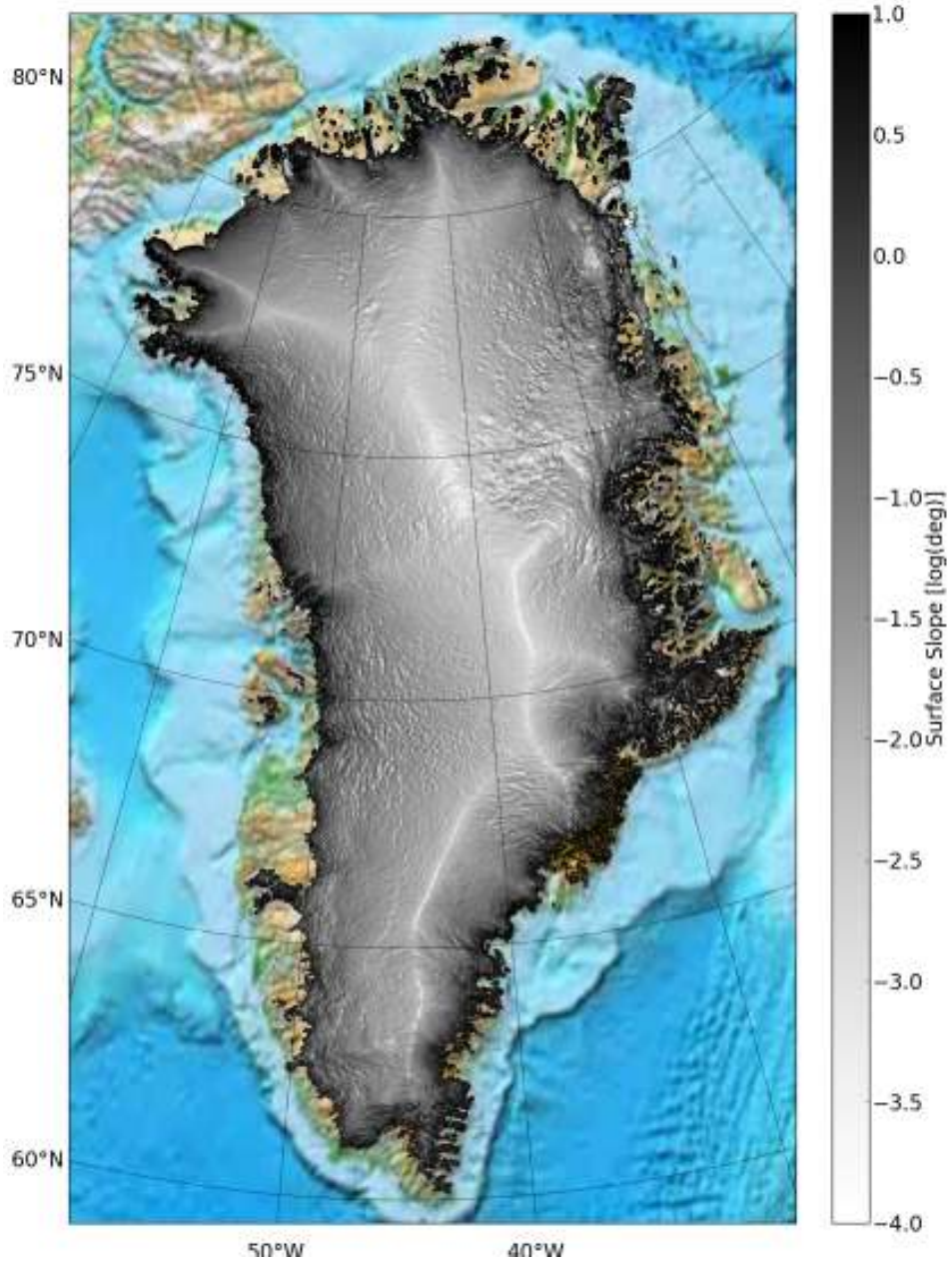

Figure 8.7 Estimated surface slope (in degrees) of the Greenland ice sheet. Showing in great detail the diverse features in the surface topography of the ice sheet. The figure is shown in log-scale of degrees to highlight surface features.

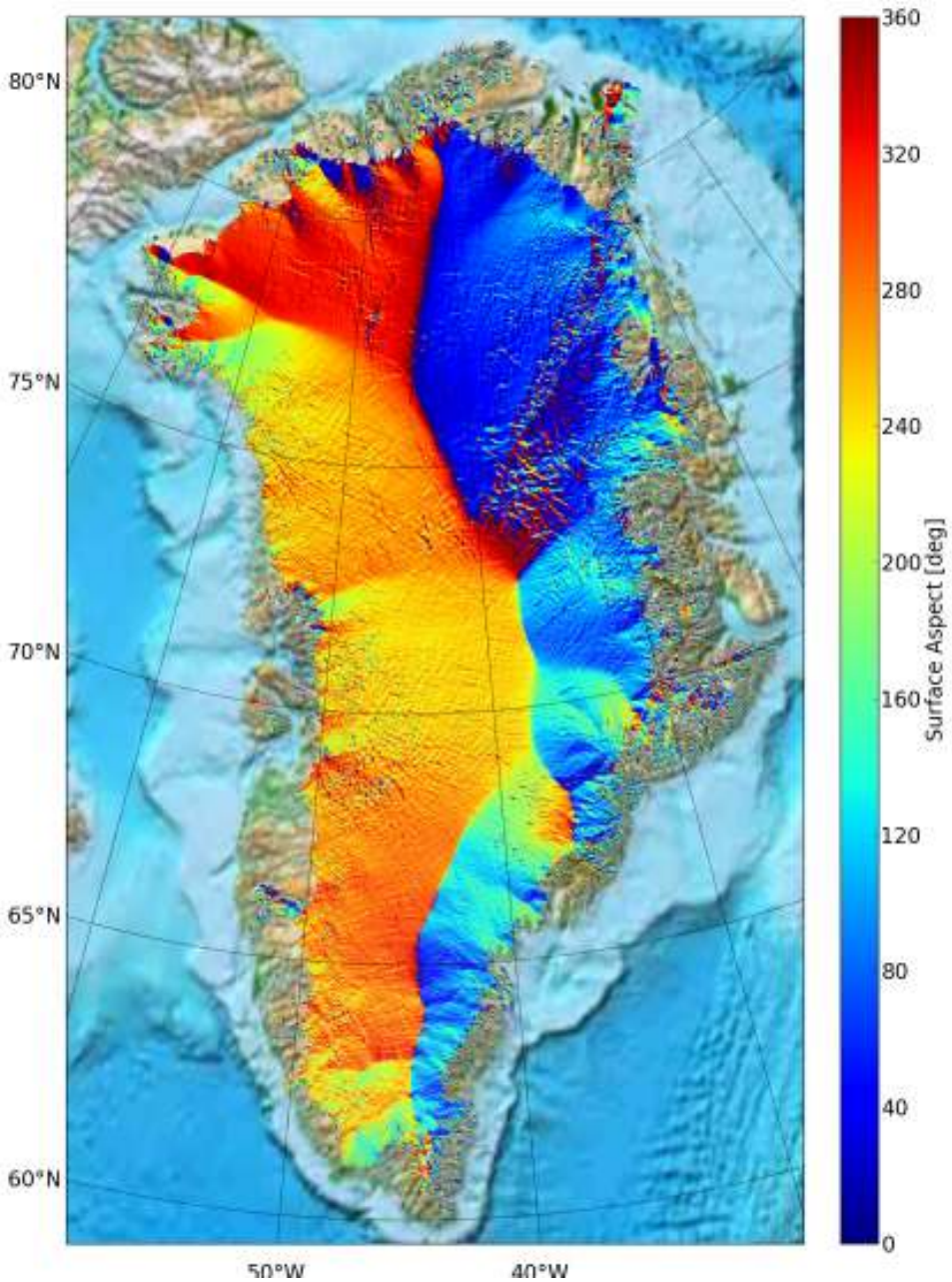

Figure 8.8 Surface aspect of the Greenland ice sheet (in degrees from North), which clearly shows the main ice divides and the main basin of the ice sheet.

9 Surface elevation changes from CryoSat-2

In this section the principles of estimating surface elevation changes over glaciated terrain, using satellite altimetry, will be presented. This will include the description and discussion of two of the most common methods used to date and their capabilities and limitations.

The mass balance of ice sheets and smaller ice caps is estimated by measuring the change in surface topography over a specific time interval. Measurements of surface elevation changes can provide estimates of the overall mass balance of the ice sheet, under assumption of snow/ice densities.

Surface elevation change rates over glaciated ice are usually determined from two different methods, referred to as the crossover method and the repeat-track method. These methods have previously been used to determine elevation changes in both Greenland (Johannessen et al., 2005; Khvorostovsky, 2012; Sørensen et al., 2011; Zwally et al., 2005, 2011), Antarctica (Davis and Ferguson, 2004a; Wingham et al., 1998; Zwally et al., 2005) and several of the major ice caps (Gardner et al., 2013; Moholdt et al., 2010, 2012).

A crossover is the location where two satellite paths intersect. The elevation difference at the crossover location is assumed to correspond to a real physical change of elevation, since it occurs at the same location but at different time epochs. In repeat-track analysis, surface elevations from near-repeat ground-tracks at different times are used to estimated the elevation change rate. As the ground tracks do not exactly repeat over time, the underlying topography needs to be accounted for in the estimation procedure to make the ground-tracks more comparable.

The crossover method and the repeat track method have different advantages and disadvantages, which can be summarized in a trade-off between accuracy and spatial coverage. The crossover method provides higher accuracy, where the repeat-track method provides higher spatial sampling. Hence, the combination of the two methods would allow utilization of their strengths, while minimizing there weaknesses.

The CryoSat-2 mission however is not in repeat orbit, as for ICESat and EnviSat, which means that the repeat-track method needs to be adjusted to properly account for the successive shift in orbit geometry over time. For the purpose of this thesis the adjusted repeat-track method will be referred to as the plane fitting method. Exactly how this method is adjusted to work on non-repeat track geometry will be discussed later in this section.

The estimation of elevation changes are further affected by the changing properties of the ice sheet surface and measurement errors, such as i.e melt, firn compaction, snowfall and orbital errors. Both methods uses different techniques to mitigate these effects on the estimated elevation changes, which will be presented and discussed.

Finally, to fully be able to utilize the advantages inherent in the both methods, they will be merged using a optimal estimation technique taking into account the accuracy of the observations.

In the following sections the two methods developed for the purpose of this thesis will be discussed; the crossover method (XO) and the plane-fitting method (PF).

9.1 The crossover method

The crossover methods is used to derive surface elevation changes at the intersection between two satellite ground tracks, between a ascending and descending track. The difference in surface height ΔH is estimated by the difference in surface height between the two tracks at the crossover intersection, seen in Fig. 9.1. The height difference at the crossover intersection can therefore be written as:

$$\Delta H_{12} = H_2 - H_1 + E \tag{9.1}$$

where H_1 is the elevation at time t_1, H_2 is the elevation at time t_2 and E is the random measurement error. The random measurement error includes satellite orbital errors, altimeter range errors and errors from the retracking algorithm (Zwally et al., 1989).

The height at the crossover location is obtained by linearly interpolating between the two closest data points to the crossover location for each track. If one of these four measurement has a distance larger than 350 m for the LRM-mode and 450 m for the SARin-mode, the crossover point is discarded. The cut-off distance for the SARin-mode is set higher than for the LRM-mode, as the ground-track in the SARin-mode has a tendency to follow topography. This has the effect that the position can vary heavily from point to point, two different ground tracks can even intersect several times, in contrast to the LRM-mode where the position is defined as the nominal ground-track, and the range corrected instead. The cut-off distance for discarding the crossover is set after CryoSat-2 20 Hz ground sampling distance, which is approximately 350 m along-track. At each crossover location the difference in surface height,

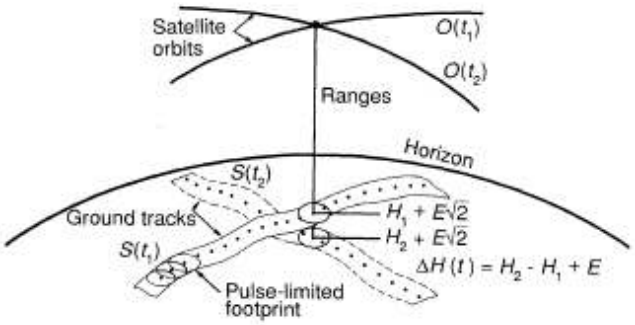

Figure 9.1 Principle of the crossover method for measuring surface elevation change between two sub-satellite ground-tracks from radar-altimeter measured observations. Image credit: (Zwally et al., 1989)

time span and waveform parameters are computed between the ascending and descending track. The waveform parameters are used to correct the estimated height difference for changes in ice sheet scattering properties (Khvorostovsky, 2012), see Section 9.1.1.

Before determining the elevation change rate the computed crossover height differences are corrected for their correlation to changes in the waveform parameters. This as changes in backscatter properties of the ice sheet can introduce spurious changes in elevation, see Section. 4.3.6. This procedure is described in detail in Section 9.1.1.

The surface elevation change is then obtained for every crossover location by dividing the estimated crossover height difference, between the ascending and descending track, with the corresponding time difference. The differences are computed as $dH = (H_a - H_d)$ and $dt = (t_a - t_d)$. The estimated elevation change rates, at the crossover locations, are estimated regardless if dt is positive or negative. This produces elevation changes rates that are normally distributed, with time spans ranging from 0-4 years for this study.

There exists methods of determining elevation changes rates over the entire time span of the data set. Where one of the most commonly used methods is the dH/dt-method, described in (Zwally et al., 1989) in which the elevation change rate is determined by fitting a linear model to the randomly distributed dH versus dt, where the elevation change rate is determined as the slope of the trend.

The usage of the dH/dt-method requires that a multitude of points are required to fit the model, which has the implications that the ice sheet needs

to be divided into different sub-regions or that data inside a specific radius is used. However, this has the implication of reducing the resolution and the accuracy of the crossover elevation changes, as they now consist of not only the random altimetric error but also the error from the fitting procedure.

In the work done for this thesis, none of the methods discussed in (Zwally et al., 1989) have been used. This as the accuracy of the crossover rates are the main priority, which is substantially reduced when applying the linear model over an area large enough to solve for the rate (typically around 5-10 km), as they are going to be used as reference rates for the plane-fit derived elevation change rates. This does however reduce the number of available crossovers with the necessary time span of approximatively 3-4 years, assuming that the rates does not change between these two years.

9.1.1 Correction for changes in ice sheet scattering properties

One of the most important corrections applied to surface elevation changes is the correction used to account for their correlation to changes in the ice sheets scattering properties, e.g the difference in waveform parameters discussed in Section. 4.3.5 and Section. 4.3.6.

This correction is important as changes in the waveform parameters (Bs, PP, LeW and TeS) reflect changes in the snow properties of the ice sheet, and can introduce spurious changes of elevation interpreted as an actual elevation change. This type of adjustment procedure has previous been adapted in studies by e.g. (Davis and Ferguson, 2004b; Khvorostovsky, 2012; Wingham et al., 1998).

In the crossover height difference calculation not only the height change is computed, but also the differences in the four waveform parameters. These are then used to estimate the sensitivity gradient (Khvorostovsky, 2012), connecting the change in elevation change to the changes in the waveform parameters. The sensitivity gradient is estimated using multivariate regression and the corrected elevation change ΔH_c can be written as:

$$\Delta H_c = \Delta H_i - \left(\frac{\delta H}{\delta Bs}\right)\Delta Bs - \left(\frac{\delta H}{\delta PP}\right)\Delta PP - \left(\frac{\delta H}{\delta LeW}\right)\Delta LeW - \left(\frac{\delta H}{\delta TeS}\right)\Delta TeS \tag{9.2}$$

where $\left(\frac{\delta H}{\delta Bs}\right)$, $\left(\frac{\delta H}{\delta PP}\right)$,$\left(\frac{\delta H}{\delta LeW}\right)$, $\left(\frac{\delta H}{\delta TeS}\right)$ are the different sensitivity gradients for each waveform parameter (estimated from the multivariate regression scheme). ΔBs, ΔPP, ΔLeW, ΔTeS and ΔH_i are the differences at the crossover location of the waveform parameters and the surface height.

This procedure is applied to each crossover location where the sensitivity gradient is computed using crossover differences of waveform parameters and surface heights inside a radius of 10 km. This is done to capture the local scattering properties of the ice sheet and to allow for a stable solution of the sensitivity gradient. Each crossover height difference is then corrected using their waveform parameter differences as input to the model in Eq. 9.2.

The sensitivity gradient is determined iteratively to improve the overall fit, where a 3σ editing procedure is used to discard outliers in each iteration. A total of up to 5-iterations is used in the procedure or until no more outlier can be detected. If the solution of the linear system is rank-deficient the estimated correction is not applied to crossover height difference and the point assumed to be removed in the later outlier editing procedure. This to preserve as many crossover as possible, as the solution is dependent on the number of available surrounding crossovers which are fewer in the marginal areas for example.

9.1.2 Accuracy and Precision

The magnitude of the random error, referred to as the ascending/descending bias (A/D-bias), can be estimated by averaging the crossover height differences with short time intervals (Fu and Cazenave, 2000), assuming that during these small time intervals there will be no physical change in the surface elevation of the ice sheet. The A/D-bias is estimated by averaging height differences with a time span less than 30 days ($\Delta t < 30$ days), according to:

$$\bar{\mu} = \frac{1}{N} \sum_{i=1}^{N} \Delta H_i \tag{9.3}$$

where $\bar{\mu}$ is the estimated A/D-bias and N is the number of crossover with a $\Delta t < 30$ days.

From this relation the relative accuracy of the surface elevations can be inferred, and where the relative precision of the surface elevation can be estimated from the standard deviation of the data with $\Delta t < 30$ days, according to:

$$\bar{\sigma} = \sqrt{\frac{1}{N} \sum_{i=1}^{N} (\Delta H_i - \bar{\mu})^2} \tag{9.4}$$

where $\bar{\sigma}$ is the estimated precision and N is the number of crossover with a $\Delta t < 30$ days.

Compared to previous radar altimetry missions CryoSat-2 was designed for land-ice monitoring with an orbit configuration optimized to obtain more satellite crossovers (10 crossovers per km^2 per year at 87°) than previous missions (Wingham et al., 2006). The accuracy of the crossover differences decreased as a function of surface slope (Brenner et al., 2007). Even though the estimated height difference has a slope dependency, it still avoids the major influence of slope, as its measured over the same location. This important fact allows for the method to be used to validate elevation changes estimated by the plane-fitting method, described in Section 9.2.

9.1.3 Capabilities and Limitations

Determining elevation change rates using crossover analysis has many advantages, where one of the main advantages is that it is not largely affected by the slope-induced error. This as the height difference is determined in the same location at different time epochs, which reflects the same underlying topography, as the pulse-limited footprint illuminates the same area between t_1 and t_2. This effectively cancels the slope-induced error in range (not in position) leaving only the random measurement errors and makes the accuracy of the method very heigh compared to i.e the plane-fitting method, discussed later.

However, the main drawback of the method is that it only provides information about the change in elevation at the crossover location. This spatial limitation makes it difficult to monitor the rapidly changing areas on outlet glaciers and the ice sheet margins, which are showing the most change to date.

9.2 The plane-fitting method

The plane-fitting method is a modified version of the repeat-track method (Flament and Rémy, 2012; Moholdt et al., 2010; Sørensen et al., 2011) where the elevation change rate is detected by applying a linear topographical model that solves for the surface elevation change rate, surface slope, changes in scattering conditions and several biases. The model is fitted to multi-temporal observations, using ordinary least squares, inside a specific radius around a wanted prediction point (grid-nodes or the observation itself).

The repeat-track method has been modified in this study, as Cryosat-2 is not in a repeat-orbit configuration, which means that conventional repeat-track method is not applicable. However, CryoSat-2 has a 30 days sub-cycle and a 369 days full repeat-cycle. This long repeat cycle gives very dense ground-track

geometry, giving an average ground-track separation of 7.5 km at the equator, which decreases with a function of latitude. The 369 day repeat and 30 day sub-cycle means that same geographical location will be revisited every 369 days and the same area roughly every 30 days. Hence, for a 4-year data set there should, in theory, be enough data to resolve the temporal trend for a relatively small area (km-scale). This as the area would contain the 369-day repeat observations plus 30-day monthly values, allowing for determination of both the seasonal variations and the trend.

However, the surface elevations inside the local area of interest, defined by the search radius, will consist of both a local topographical signal and the wanted elevation change signal. Several different approaches to separate these two signals have been proposed, such as (Howat et al., 2008; Moholdt et al., 2010, 2012; Pritchard et al., 2009; Sørensen et al., 2011) using ICESat. The repeat-track approach requires that the ground tracks are randomly spaced around the reference track (Ewert et al., 2012). This is usually the case for the repeat-track orbit configuration, as the shift in ground track is mostly due to orbital perturbations, pointing errors and other factors (Slobbe et al., 2008). This is not the case for the CryoSat-2 orbit configuration and can, due to orbit geometry, introduce a involuntary systematic (spatially correlated) temporal elevation change bias, as the orbit moves in a specific direction over time.

The approach developed in this thesis is to use the newly generated CryoSat-2 DEM, see Section 8.4.2 to remove the long-wavelength topography from the individual surface height observations, effectively removing the topographical part of the signal. However, due to the resolution of the DEM, smoothing from the gridding procedure and gridding artefacts there will still exist unmodelled topographical components left. To account for the residual topographical signal the linear model, described in 9.5, solves for the residual topography by estimating the along and across track slopes.

The linear model used in this thesis uses the methodology developed by (Flament and Rémy, 2012) for elevation change detection using EnviSat. The model is an extension of the model used for repeat-track analysis for ICESat (Ewert et al., 2012; Howat et al., 2008; Moholdt et al., 2010, 2012; Sørensen et al., 2011), but modified for the specific conditions inherent to radar altimetry. In contrast to the model used in laser altimetry the radar version is not only built to account for the local topography, but also for other factors such as (1) changes in scattering conditions of the ice sheet, (2) the A/D-bias, (3) seasonal variations and (4) the 2012 Greenland melt event, see (Nilsson et al., 2015b).

The surface topography and changes in surface topography can be modelled

using a multivariate regression scheme, according to:

$$\begin{aligned} H &= H_0 + \alpha_1(\lambda - \lambda_0) + \alpha_2(\theta - \theta_0) + \alpha_3(\lambda^2 - \lambda_0^2) + \alpha_4(\theta^2 - \theta_0^2) \\ &\quad + \alpha_5(\lambda^2 - \lambda_0^2)(\theta^2 - \theta_0^2) + \alpha_6(Bs - \bar{Bs}) + \alpha_7(LeW - \bar{LeW}) \\ &\quad + \alpha_8(PP - \bar{PP}) + \alpha_9(TeS - \bar{TeS}) + \alpha_{10}Az \\ &\quad + \alpha_{11}H_{0/1}(t - t_e) + A_s \sin(2\pi t) + A_c \cos(2\pi t) \\ &\quad (dH/dt)(t - t_o) + res \end{aligned} \tag{9.5}$$

where H_0 is the mean elevation (or elevation residual) inside the footprint, (λ,θ) are the longitudes and latitudes (respectively) of the observations inside the search radius, (λ_0,θ_0) are the longitudes and latitudes of the prediction points, (t,t_0) is the time and mean time of the observations inside the search radius, dH/dt is the estimated elevation change, (Bs,$\bar{Bs}$) is the backscatter coefficient and the mean backscatter coefficient (dB), (LeW,$\bar{LeW}$) is the leading edge width and the mean leading edge width (m), (PP,$\bar{PP}$) is the waveform peakiness and the mean peakiness, (TeS,$\bar{TeS}$) is the trailing edge slope and the mean trailing edge slope (s^{-1}), Az is the satellite heading (deg), $H_{0/1}$ is a heavyside function, (t_e) is the time of the 2012 melt event, the sine and cosine term describes the seasonal component of the signal (years) and res is the residual error between the model and the observations.

(Armitage et al., 2014) found a large A/D-bias over Antarctica using the OCOG-retracker (Vignudelli et al., 2011). To account for this bias (McMillan et al., 2014) introduced a ascending/descending bias-term in the regression model (Az). (Helm et al., 2014) however showed that this bias is heavily dependent on the retracking threshold used and is almost removed when using a threshold of 20%, which is used in the LRM-mode in this thesis. This term was however included in the regression model to try to account for any residual A/D-bias effects in the data.

The heavyside function $H_{1/0}$ is a very important parameter for the average elevation change signal of the GrIS during the CryoSat-2 operational period. This is due to that in mid July 2012 the interior of the GrIS experienced the largest melt in modern-recorded history, affecting more than 90% of the ice sheet (Nghiem et al., 2012). The rapid melt and subsequent refreezing of the surface shifted the radar reflecting surface upwards approximately 50-100 cm (depending on retracker) and created a false elevation change signal. This can be seen in Fig. 9.9 where the interior of the ice sheet, which usually shows very small height changes, now show a very large positive signal. Please see (Nilsson et al., 2015b) for a more detailed description of how the melt event affects the retrieval of surface heights over GrIS using radar altimetry.

This false elevation change signal needs to be accounted for in our regression model, and is done so by introducing a heavyside function ($H_{1/0}$) centred at the time of the melt event t_e=2012.75 (corresponding to mid July 2012).

The heavyside function is defined as follows:

$$H_{0/1}(t) = \begin{cases} 0 & \text{if } t_e > t \\ 1/2 & \text{if } t_e = 0 \\ 1 & \text{if } t_e < t \end{cases}$$

This function accounts for the change in magnitude introduced by the melt event in the local time-series around every prediction point. The details of which will be further discussed and shown in Section 9.3 and Fig. 9.3,9.9

The coefficients of the linear model are solved for using a iterative distance-weighted least-squares approach almost identical with the one described in Section. 7.1, using Cholesky decomposition. The iterative solution is used to identify and remove outlier, where model residuals larger than 3σ are considered outliers. A maximum of 5-iterations are used or until no more outliers are detected. In the iteration process the rank-deficient solutions are detected using the Cholesky decomposition singularities. If a rank-deficient solution is found a flag is set and the value solution set to NaN.

The model of 15-terms in the algorithm require a minimum of 25 observations to solve for the coefficients, this to minimize rank-deficient solutions. This is one of the main reasons why the height observations are detrended, as this allows for the reduction of the number of coefficients in the model, i.e the bi-quadratic terms. However, these are still used in the study, as they only account for smaller fraction of the variance between the model and the data when detrended.

The solution to the linear system can be generalized as follows.

$$\hat{x} = (A^T W A)^{-1} A^T W \Delta H \tag{9.6}$$

where A is the design matrix containing the partial derivatives of the model, W is a weighting function defined in Eq. 9.7 and ΔH are the de-trended height observations.

The same weighting function is used in this algorithm as in the bi-quadratic surface modelling algorithm in Section. 7.1.

$$W = \frac{1}{1 + \left[\frac{D}{D_c}\right]^2} \tag{9.7}$$

where D is the distance between observations and prediction point and D_c is a factor controlling the resolution of the model.

The standard error of the coefficient are also further defined as in Section. 7.1 and are assumed to representative of the overall accuracy of the estimated parameters.

$$\hat{\varepsilon}^2 = \sigma^2 (A^T W A)^{-1} \tag{9.8}$$

where σ^2 is the variance of the residuals.

9.2.1 Accuracy and Precision

The accuracy of the plane-fitting method is heavily dependent on the determination of the cross-track slope, as this is representative of the local surface slope. Hence, the resolution of the plane, e.g the size, is of large importance. Fitting of larger planes reduced the possibility of capturing the local spatial patterns of elevation change and introduces larger fitting errors. Further, as the plane is used to determine the surface slope it is likely that the fitting procedure and outlier editing might remove real parts of the signal, degrading the overall accuracy. This means that the relatively simple model used in Eq. 9.5 is only good for smaller regions and were the size of the regions depends on the number of parameters in the model.

The model also assumes that the surface can be represented by a smooth continuous function. This is however not true for the marginal and coastal areas of the ice sheets where there exist large surface slopes and rough topography. These are the areas where the largest changes are expected to be seen (Rignot and Kanagaratnam, 2006a). However, there has been previous studies using this type of method that find good agreement in the linear trends and seasonal variations of the ice sheets estimated from other missions, such as GRACE (Horwath et al., 2012). Other studies has also shown good agreement between these types of repeat-track methods with the crossover method (Moholdt et al., 2010; Sørensen et al., 2011).

9.2.2 Capabilities and Limitations

The main advantages of the plane-fitting method in comparison with the crossover method is that it increases the spatial sampling and the number of elevation changes obtained. This has the effect of increasing the overall SNR and the spatial resolution, as more measurements are available for the

analysis. This allows better coverage of local spatial patterns in the marginal and coastal areas of the ice sheet.

The introduction of the CryoSat-2 DEM also allows the removal of the long-wavelength component of the topography, allowing for a better separation of the elevation change signal. However, the current resolution of the DEM and the smooth function approximation does not allow for the removal of the short-wavelength component of the topographical signal. This has the possibility of introducing a bias that might be hard to quantify (Slobbe et al., 2008).

9.3 Merging of surface elevation change

The merging of the crossover and plane-fit derived elevation changes is done in an effort to improve the overall recovery of the local spatial pattern while preserving accuracy. The crossover derived elevation changes, with their higher accuracy seen in Table. 9.1, are used as a reference surface to correct the plane-fit derived elevation changes. The plane-fit derived elevation changes, with its much higher spatial resolution, is then adjusted using the more accurate crossover estimates.

This allows for improved spatial resolution and higher accuracy of the estimated spatial pattern of elevation change. This is in general not an uncommon approach, as crossover are usually used to validate elevation changes derived from the plane-fitting method(s), as put forward in Section 9.1.2. However, combining the two methods using their accuracies allows the crossover to be used not only for validation but also for the estimation.

Before the merging procedure can be performed several constraints must be meet. Firstly the derived surface elevation changes need to have the same time span. This as elevation changes with different time spans need not have the same elevation change rate, introducing a discrepancy in the final estimate. Secondly the estimated elevation change rates need to be analysed to determine if there exist any slope dependencies, or differences in slope dependencies between the two data set. This as any dependency on surface slope will effectively bias the final estimates. The estimated rates from the two products finally also need to be edited for gross outliers, to avoid interpolation errors.

To merge the elevation change rates from the crossover and plane-fit methods they need to cover the same time span. Analysing the time span of the estimated elevation change rates from the plane-fitting method in Fig. 9.7 one observes that the bulk of the rates are estimated over a time span of 3-4

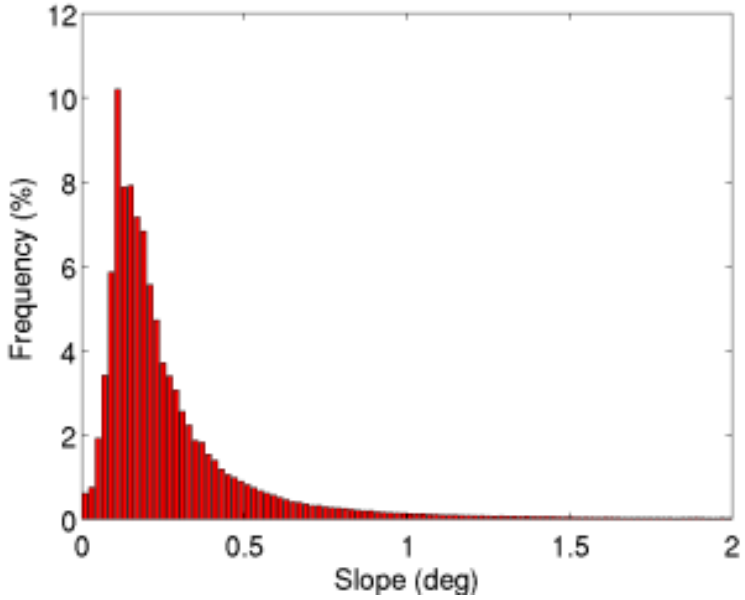

Figure 9.2 Shows the number of elevation changes (XO+PF) binned according to the surface slope. From this it can be observed that there are very few observations on slope larger than 1°.

years. Therefore a cut-off time span of 3-years was set for both the crossover and plane-fit rates, where all time spans less than 3-years were removed. This produced average values of time spans of 3.33 years for the crossover method and 3.78 years for the plane-fit method, as seen in Table. 9.1 and Table. 9.2. Both methods show reasonable consistent average time spans and are therefore allowed to be merged, this assuming that no large change in the rate of elevation change is presented between the 3-4 year time span. Analysing the slope dependencies of the elevation changes between the two products, seen in Fig. 9.3, an overall slope dependency can be found. However, the two methods show good agreement, up to roughly 1° of surface slope, from where it diverges. The good agreement, up to ∼1°, allows us to go a-head with the merging procedure, as this is the regions where most of the observations are located, see Fig. 9.2.

The divergence between two methods should no be thought of as an error. It instead reflects the accuracy and the difference in the number of observations of the two data set, and this difference is one of the main reason why the merging is done at all. The crossover method for example show a much higher rate and more variable rate of elevation change for the higher sloping regions (marginal areas of the ice sheet) than the plane-fitting method. This is most probably due

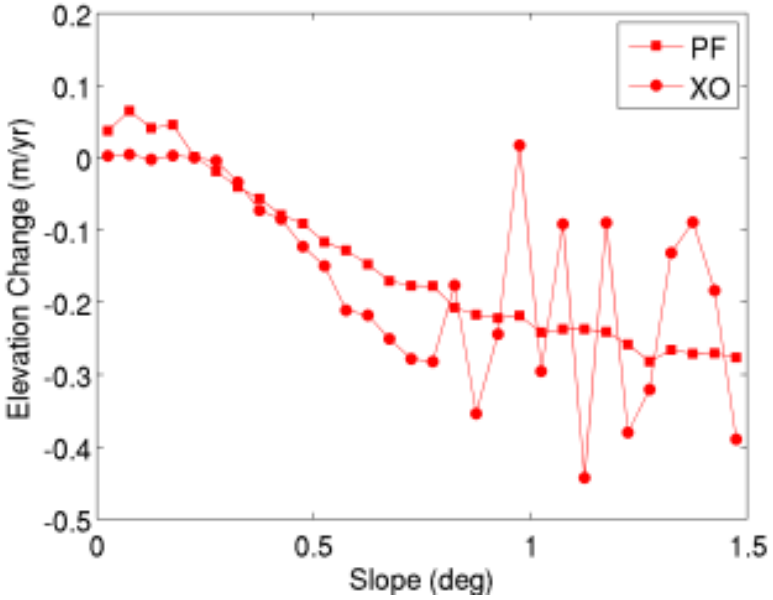

Figure 9.3 Shows the crossover (XO) and plane-fit (PF) derived elevation changes relation to surface slope. The elevation changes from the two methods show good agreement up to approximately 1° of surface slope, after which they start to diverge. The elevation changes estimated from the crossover method show larger rates of elevation changes at higher surface slopes than the ones derived from the plane-fitting method.

to that the crossover method better can capture the elevation change in this regions, as the average interpolation distance to obtain the height difference should be in the order of 225 m.

The plane-fitting method on the other hand shows very little variation, as a function of slope, and a much lower rate of elevation change in the higher sloping regions. This can most likely be attributed to the size and resolution of the plane used for estimating the elevation change signal. In the higher sloping areas, with more rough topography, the method has larger difficulties separating the topographical signal from the elevation change signal. This due to that the topography is assumed to be represented by a smooth function. Hence, by merging the results from the two methods the elevation signal in theses areas should be captured better. One should also mentioned that the large variations seen in the crossover method above 1.2° is due to the sparse number data points in these bins. Studying the lower slope regions ($\alpha < 0.1°$), in Fig. 9.3, in more detail a discrepancy can be found between the crossover and

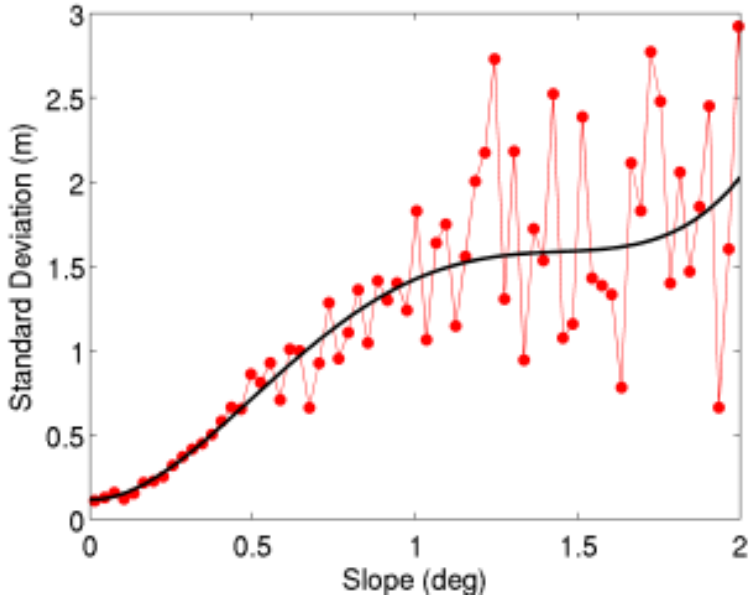

Figure 9.4 Shows the standard deviation of satellite crossovers, binned as function of surface slope, with a time span of Δt <30 days. It further shows the parametrized error model (black-line) used for deriving the precision of the observations as a function of surface slope.

plane-fit method. The plane-fitting method in this area show a more positive signal (∼5 cm) than its crossover counterpart, which is close to zero. This can probably or most likely be attributed to the 2012 melt event, which was not be fully accounted for in the regression model of Eq. 9.5.

The two methods are merged using their estimated accuracies, or standard deviations, by the means of least-squares collocation. However, the estimated accuracies from the fitting procedure of the two methods are not representative of their true accuracy. This is best illustrated by the plane-fitting method, which due to its many parameters, has a tendency of over parametrization producing very small residuals and thus a small standard error. This can have the result that the errors become unrealistically small. To obtain a more representative error the measurement uncertainty is added, which is estimated from crossovers with a time span of less than 30 days (see Section 9.1.2).

However, the precision and accuracy degrades with surface slope (Brenner et al., 2007), therefore the degradation needs to be accounted for somehow. In this thesis this was done by parametrizing the precision as a function of surface slope, using a 4th-order polynomial up to 2° surface slope, seen in Fig 9.4.

The parametrization was performed by first binning the crossovers with Δt <30 days according to slope to reduce noise. The resulting relation is shown in Fig. 9.4, and shows an almost linear relation up to approximatively 1° surface slope. The parametrized model was used to estimate the measurement precision for all elevation changes up to 1.5° surface slope, after which the noise becomes very large. The crossovers with a slope larger than 1.5° was instead set to a constant value of 1.5 m, as the precision tends levels out around this value.

The measurement error or precision σ_{cs} of the measurements are converted to an elevation change error by dividing the estimated standard deviation by the mean time span the data set ($\Delta t = 4$ years). The resulting elevation change error is then a function of surface slope α and used to determine the elevation change error ε_{xo} for each crossover observation.

$$\varepsilon_{xo} = \frac{\sigma(\alpha)_{cs}}{\bar{\Delta t}} \tag{9.9}$$

The elevation change error for the plane-fitting ε_{pf} method can instead be written as the root-square-sum (RSS) of the measurement error, as a function of slope, and the error estimated from the fitting procedure ε_{fit}, according to;

$$\varepsilon_{pf}^2 = \varepsilon_{xo}^2 + \varepsilon_{fit}^2 \tag{9.10}$$

Finally before merging the two data sets a outlier removal procedure is applied to remove any residual gross error in the elevation changes and the estimated error, by the means of a simple iterative 3σ filter. Steps where taken not to over edit the elevation changes, as this has the risk of removing dynamical signals in the marginal areas.

The merging was performed using collocation (Moritz, 1978), described in Section 7.2, onto a regular space grid with a resolution of 0.01° × 0.025° (latitude × longitude), corresponding to roughly 1 km resolution. The 1 km resolution was selected to be able to capture local scale phenomena in the marginal areas of the ice sheet, which currently are showing the largest changes.

The two data sets are given as input to the GEOGRID interpolation software (Forsberg and Tscherning, 2008). The estimation was done using a correlation length of 100 km to endure a certain amount of smoothing, a minimum RMS-error of 3.2 cm a^{-1} (estimated from the precision over flat terrain, where α <0.1°) and a total of 100 observations per prediction point. A correlation length of 100 km was used to obtain adequate smoothing of the estimated grid.

However, the majority of the 100 points used in the prediction should be inside a radius of 0-3 km, see Table. 9.2. The estimated elevation change grid was then smoothed top reduce interpolation artefacts using a 15 km Gaussian smoothing kernel.

9.4 Surface elevation change of the Greenland Ice Sheet

Surface elevation changes of the Greenland Ice Sheet were estimated independently for the two different modes. This was done to reduce the elevation change bias due the implementation of the two different retrackers in the different modes. This as the choice of retracker has a direct bearing on the magnitude of the A/D-bias, which can be seen in Fig. 8.4 and Fig. 8.3. Processing them separately reduced the magnitude of the bias at the border in between the two modes, which is further reduced by the smoothing applied in Section 9.3.

The elevation changes estimated by the crossover and the plane-fitting method were, as described in Section 9.1 and 9.2, corrected for changes in ice sheet scattering properties. No correlation threshold for applying the scattering correction was however applied in the two methods, as was for example done in (Khvorostovsky, 2012). It is instead assumed that low correlation would not add a significant correction to the elevation change, and that any spurious change in elevation would be removed in the iterative outlier screening procedure (for the plane-fit method), or in the final outlier screening procedure discussed Section 9.3.

The search radius for the plane-fitting method was set to 3 km around every prediction point, where the observations inside the radius was used to solve for the coefficient of the model described in 9.5.

In previous studies using variations of the repeat-track method, such as for ICESat (Sørensen et al., 2011) and EnviSat (Flament and Rémy, 2012), the search radius used was 250 m and 500 m respectively. The larger search radius used for EnviSat reflects the coarser ground track sampling of EnviSat compared to ICESat. The choice of the smaller search radius, used in these studies, are used to increase the likelihood that the derived elevation change will reflect the local elevation change pattern. A larger search radius has a smoothing effect on the locally estimated surface elevation change. However, for the EnviSat study (Flament and Rémy, 2012) an 8-year data set was used to derive the surface elevation change. The longer time series improves the data coverage, as more data is available per unit area, allowing for the least-squares

model to be easily be solved.

This is the main reason for the larger search area used in this thesis, as an adequate number of observations are needed to solve for the 15-term linear model. However, to reduce the smoothing effect the resolution parameter described in Eq. 9.7 was used in the solution. This parameter is set to 500 m, corresponding to the resolution used in the EnviSat study.

Comparing the elevation changes estimated from the two methods they show on average good agreement both in average rates and variability, seen in Table. 9.1 and Table. 9.2. The crossover method shows higher variability indicated by its standard deviation, compared to the plane-fit method. This difference in variability is most likely due to the smoothing effect introduced by the plane fitting, discussed in Section 9.3.

Parameters	Mean	Std	Max	Min	N
ΔH (m/yr)	-0.06	0.67	2.81	-3.82	64,334
ΔE (m/yr)	0.08	0.08	0.40	0.03	64,334
ΔT (years)	3.33	0.25	4.10	3.00	64,334

Table 9.1 Statistics for the crossover method in the form of the elevation change ΔH, elevation change error ΔE, time span ΔT and the number of crossover elevation changes N for the entire Greenland Ice Sheet.

Figures 9.5-9.7 show the histograms of the different parameters of the two methods, where one should notice the much smaller error for the crossover method. Another important thing to notice is the number of crossovers rates available compared to the plane-fitting method, seen in Table. 9.1 Table. 9.2. The number of rates available from the crossover method is only 64,334, compared to 16,446,738 for the plane-fitting method. However, the main purpose of the crossover method is to adjust the estimated plane-fit rates, as the crossover rates are by definition more accurate. There exist possibility of increasing the number of crossover rates by i.e. applying the dH/dt-method, detailed by (Zwally et al., 1989), where a linear model is fit to surrounding crossover versus time differences around the crossover location. This has however the disadvantages of reducing the overall accuracy due to the fitting procedure and the large search radius needed, and is therefore not used in this thesis.

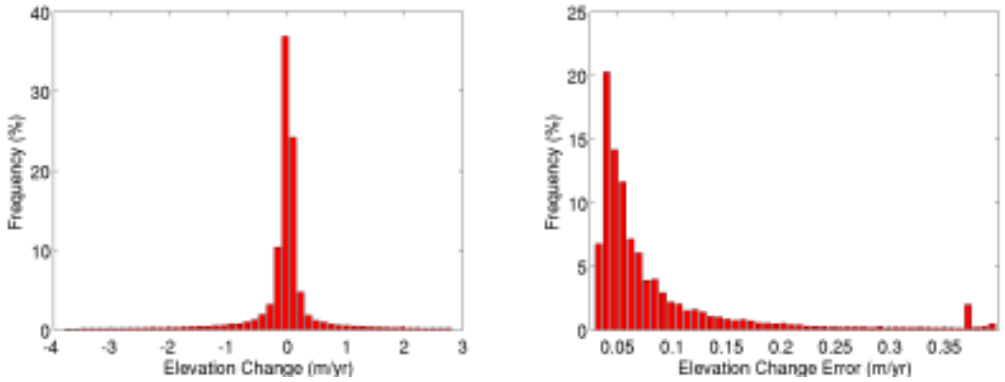

Figure 9.5 Surface elevation changes (left) of the Greenland Ice sheet estimated from the crossover method, with the corresponding elevation change error (right).

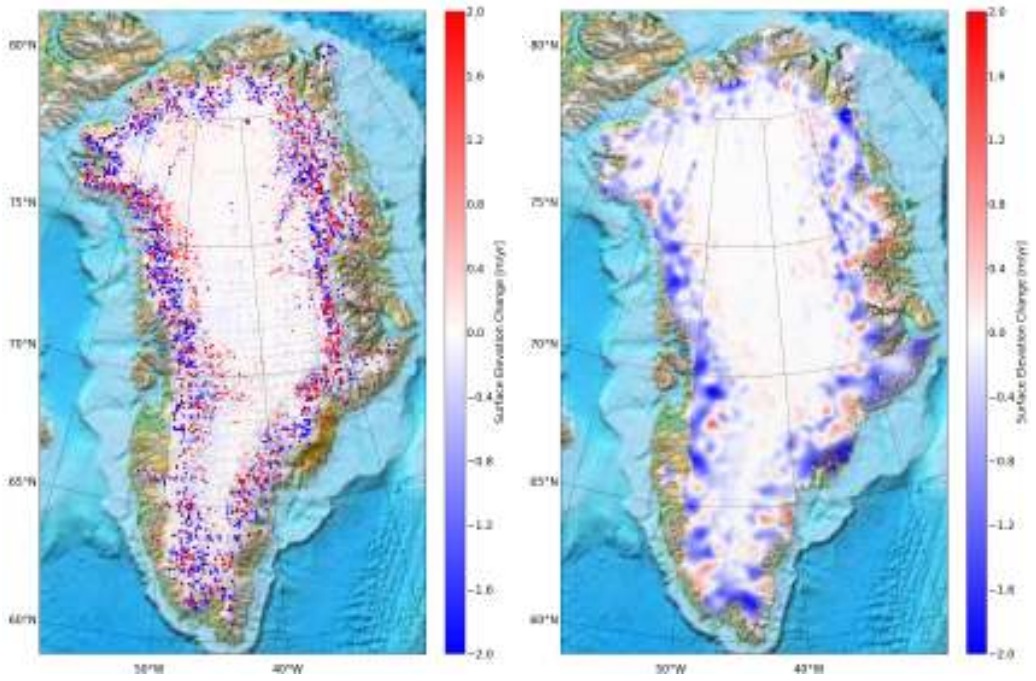

Figure 9.6 Surface elevation changes of the Greenland Ice sheet estimated from the crossover method, depicting both gridded (right) and non-gridded (left) observations.

Fig. 9.6 shows the spatial pattern of elevation changes estimated from the crossover method with a time span larger than 3 years. From Fig. 9.6 it can be observed that the interior of the ice sheet show elevation changes close to zero, whereas the rates increase outwards to the margins. Further, the variability of the elevation changes at the margin of the Greenland Ice

Sheet (SARin area) is much larger compared to the estimated from the plane-fit method in Fig. 9.8. This reflects the accuracy of the two methods where the crossover methods higher accuracy captures better the local patterns of elevation change compared the plane-fit method. The difference of which can be attributed to the the plane-fit method assumes that the surface topography can be represented by a smooth bi-quadratic plane.

Fig. 9.6 and 9.8 also shows the difficulties of interpolating a sparse set of surface elevation changes. Where the interpolated spatial patterns between the crossover method and plane.fitting methods alone show large difference, in the form of interpolation errors. However, the crossover derived elevation changes seems to be less affected by the 2012 melt event (Nilsson et al., 2015b), as seen when comparing the two figures visually. Here the plane-fit derived elevation changes show a larger positive signal in the interior of the ice sheet compared to the crossover derived elevation changes.,

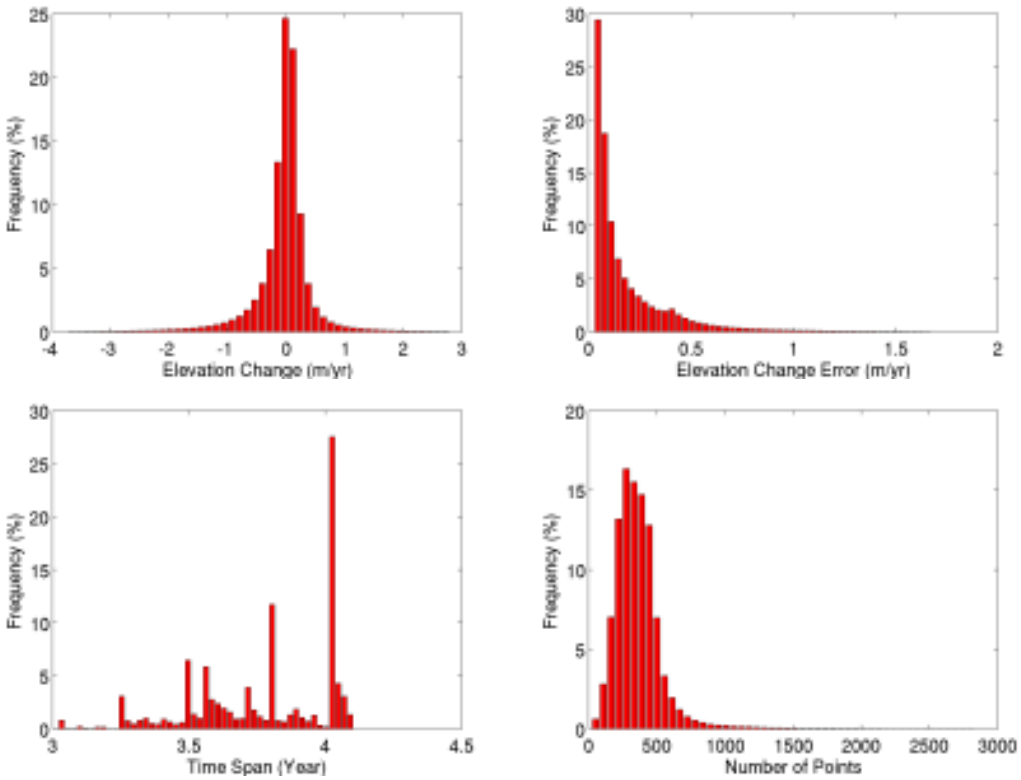

Figure 9.7 Surface elevation changes (top-left) of the Greenland Ice sheet estimated from the plane-fitting method, with the corresponding elevation change error (top-right), time span (bottom-left) and number of data points in solution (bottom-right).

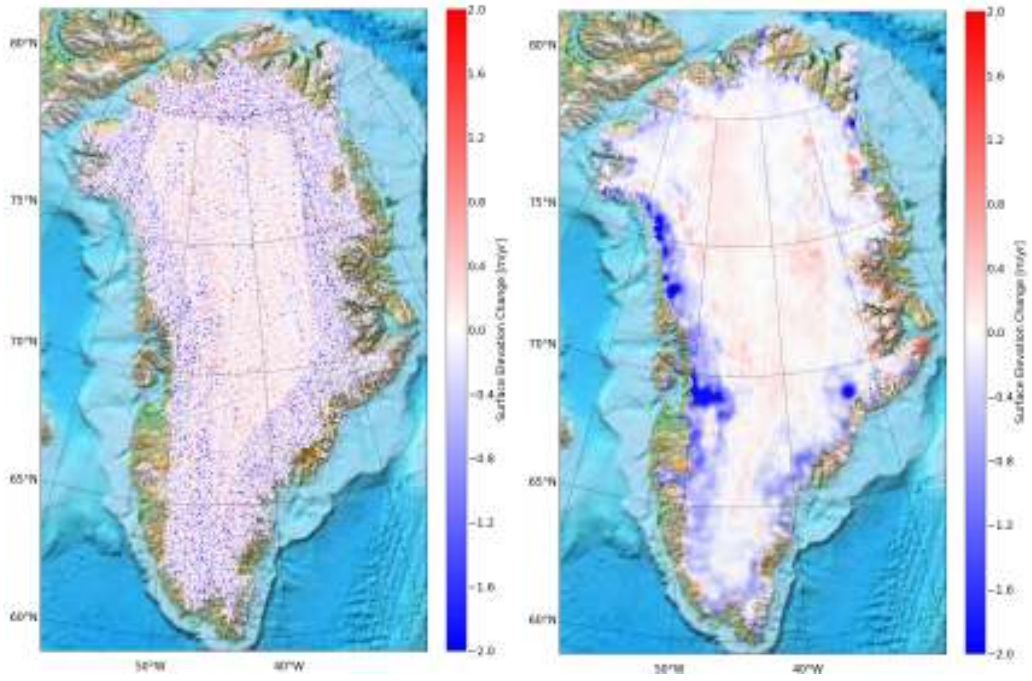

Figure 9.8 Surface elevation changes estimated from the plane-fitting method over the Greenland Ice Sheet, in gridded (right) and non-gridded (left) format.

Parameters	Mean	Std	Max	Min	N_{tot}
ΔH (m/yr)	-0.05	0.48	2.79	-3.75	16,446,738
ΔE (m/yr)	0.19	0.21	1.67	0.03	16,446,738
ΔT (years)	3.78	0.26	4.10	3.00	16,446,738
N_{sol}	360	188	2829	24	16,446,738

Table 9.2 Statistics for several important parameters estimated from the plane-fitting method. Such as the elevation change ΔH, elevation change error ΔE, time span ΔT, the number of surface height used in the solution N_{sol} and the total number of plane-fit surface elevation changes N_{tot}.

Noting that the crossover derived elevation changes seems to less affected by the Greenland 2012 melt than the plane-fitting method shows that the introduction of the heavyside function in the plane-fit regression model does not fully account for the positive signal introduced by the melt event. It does however reduce it dramatically, as seen in Fig. 9.9. If one assumes that the majority of the positive elevation change signal is due to the melt event and only using observations above 2000 m (for predominant dry snow condition),

the introduction of the heavy-side function effectively reduced the magnitude of the positive bias with 88%. This makes the parameters an important part in the estimation of accurate elevation changes on the Greenland Ice Sheet during the 2010-2014 period. One can however note in Fig .9.3 and Fig. 9.9 that their still exists a residual average error of roughly 5 cma^{-1} in the flat interior parts of the ice sheet that have not been accounted for.

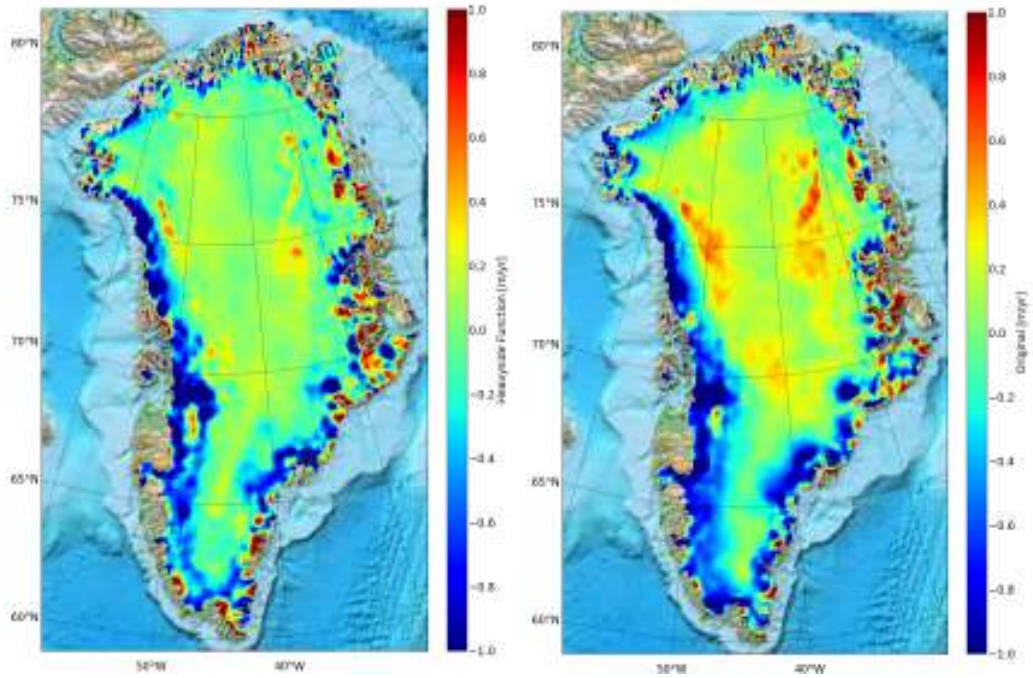

Figure 9.9 The figures depict the reduction in magnitude of the elevation bias introduced by the 2012 melt event, by the introduction of a heavy-side function into the regression model. Where the figure on the (right) shows the surface elevation change pattern with the heavyside function included and (left) the elevation change pattern without the inclusion of the function. The figures are smoothed using a 40 km Gaussian smoothing kernel for visualization purposes.

However, a residual signals can still be observed in the gridded observations of elevation change, seen in Fig. 9.9. If these signals are melt event related is difficult to speculate about at this time. They seem on the other hand be related to the sub-surface scattering properties of the ice sheets near surface layers, as these positive anomalies can also be spotted in semi-contemporary elevation changes derived from EnviSat from 2006-2010 (Sørensen et al., 2014), but not in ICESat derived elevation changes from 2003-2009 (Sørensen et al., 2011).

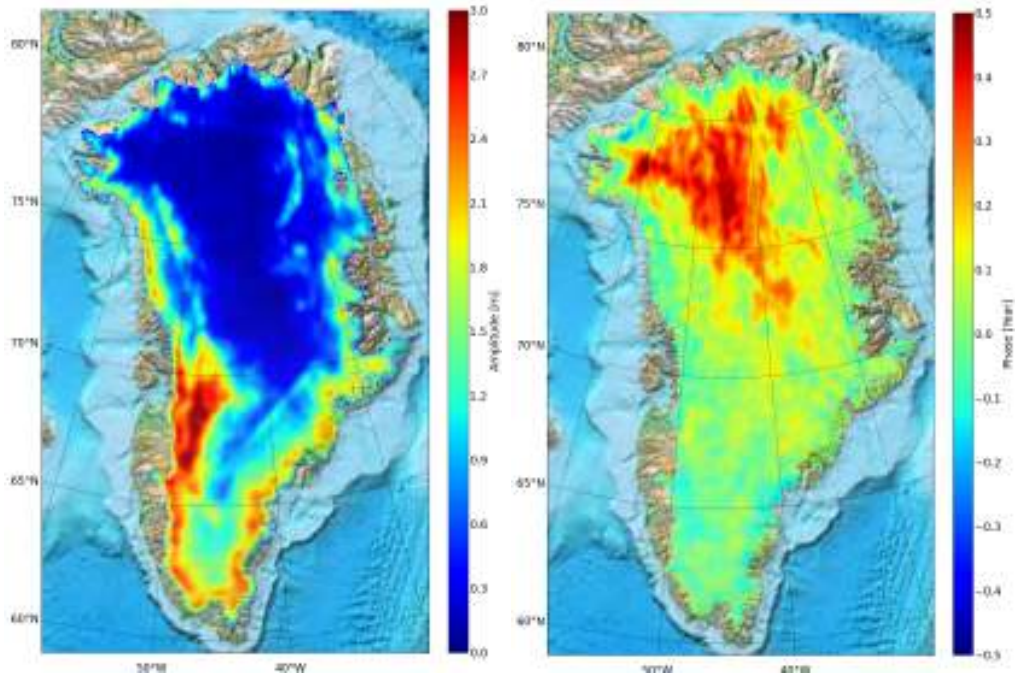

Figure 9.10 The estimated amplitude (left) and seasonal phase (right) of the seasonal signal Greenland Ice Sheet, estimated from the solution of the model in Eq. 9.2.

One of the advantages of using the plane-fitting method is that important auxiliary glaciological information can be derived from the solution of the topographical model used to derive the elevation change. Fig. 9.10 shows and example of this where the seasonal amplitude and phase have been plotted. Figures like these allow for the analysis of i.e. accumulation, flow and melt on spatial scale during a year. Figure 9.10 shows large seasonal signals (amplitude) in the souther-marginal areas of the ice sheets that agrees well with the accumulation pattern of the Greenland Ice Sheet, see (Bales et al., 2009). The pattern of seasonal phase is however in this case more ambiguous, as the model seem not to be able to fully account for the variations in the southern parts of the ice sheet. It does however indicate accumulation in the NW part of Greenland during the summer part of the year, as would be expected.

Figures 9.11-9.12 show the interpolated results from the merged crossover and plane-fit elevation changes, using the collocation method, and the interpolation error. Fig. 9.11 a large thinning can be observed along the marginal coastal areas of the ice sheet, especially in the areas of major outlet glaciers, see Fig. 9.13. The thinning pattern at these location are very localized compared to the other surrounding regions, indicating large dynamics in these

regions during the 2010-2014 time span. This pattern has also been observed by (Helm et al., 2014) using CryoSat-2 data and (Sørensen et al., 2011) using ICESat. The spatial pattern of elevation change show localized thinning and accumulation in different parts of the ice sheet. However, the overall pattern shows small scale accumulation in the interior of the ice sheet (stable), with increased thinning rates moving down in elevation to the marginal areas of the ice sheet.

Figure 9.12 show the interpolation error from the collocation method, which depicts the standard error from each prediction point. From Fig 9.12 it can be observed that the largest error can be found in the marginal areas of the ice sheet, where some regions show errors larger than 30 cma^{-1}. This is can especially be seen on the east coast of Greenland, where the magnitude of the interpolation error correlates well spatially with rapid or largely varying elevation change features. This is expected as these regions also show the highest slopes and the roughest topography on Greenland.

However, comparing spatial pattern in Fig. 9.14 from different mission, such as Envisat and ICESat with roughly contemporary time spans, many of the surface features seen in CryoSat-2 can not be seen in ICESat. EnviSat does however show many of the same features as CryoSat-2, such as the large positive signal on the eastern parts of Greenland close to the 77.5° latitude.

There also exists difference in the rates on the eastern Greenland peninsula 70° latitude. Here a positive rate of elevation change is observed for both EnviSat and CryoSat-2, but not observed by ICESat which shows negative or close to zero rates of elevation change. As the rates for EnviSat and ICESat are roughly contemporary, and that the same overall elevation change pattern can be seen by both CryoSat-2 and EnviSat, indicates that these signals might be radar dependent.

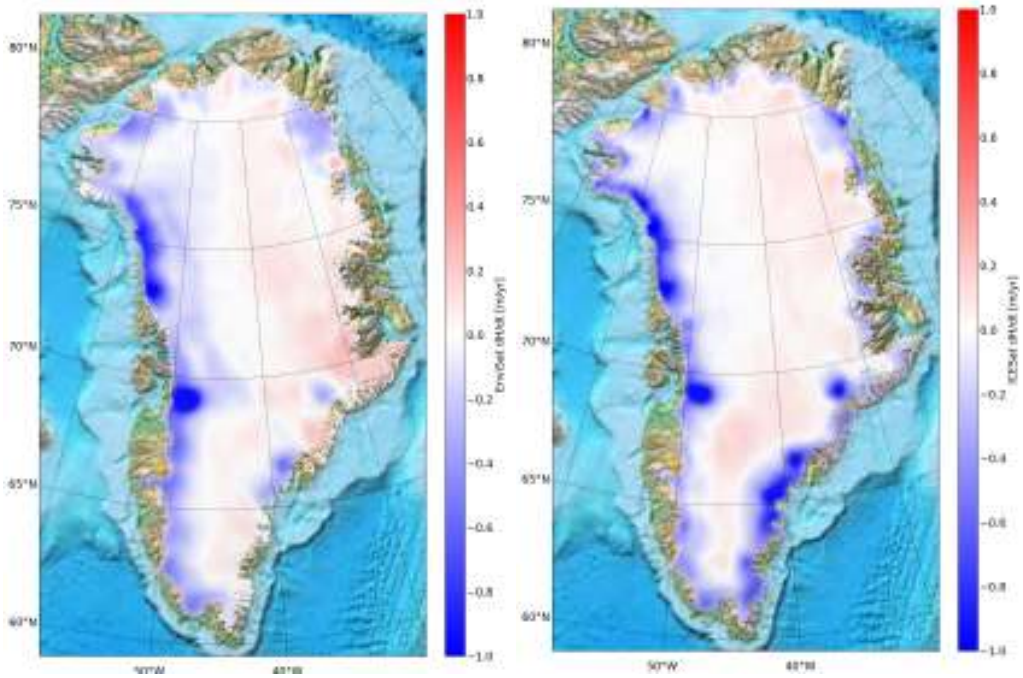

Figure 9.14 Elevation change rates estimated from radar and laser repeat-track analysis from EnviSat (left) 2006-2010 and ICESat (right) 2003-2009 (Sørensen et al., 2014, 2011)

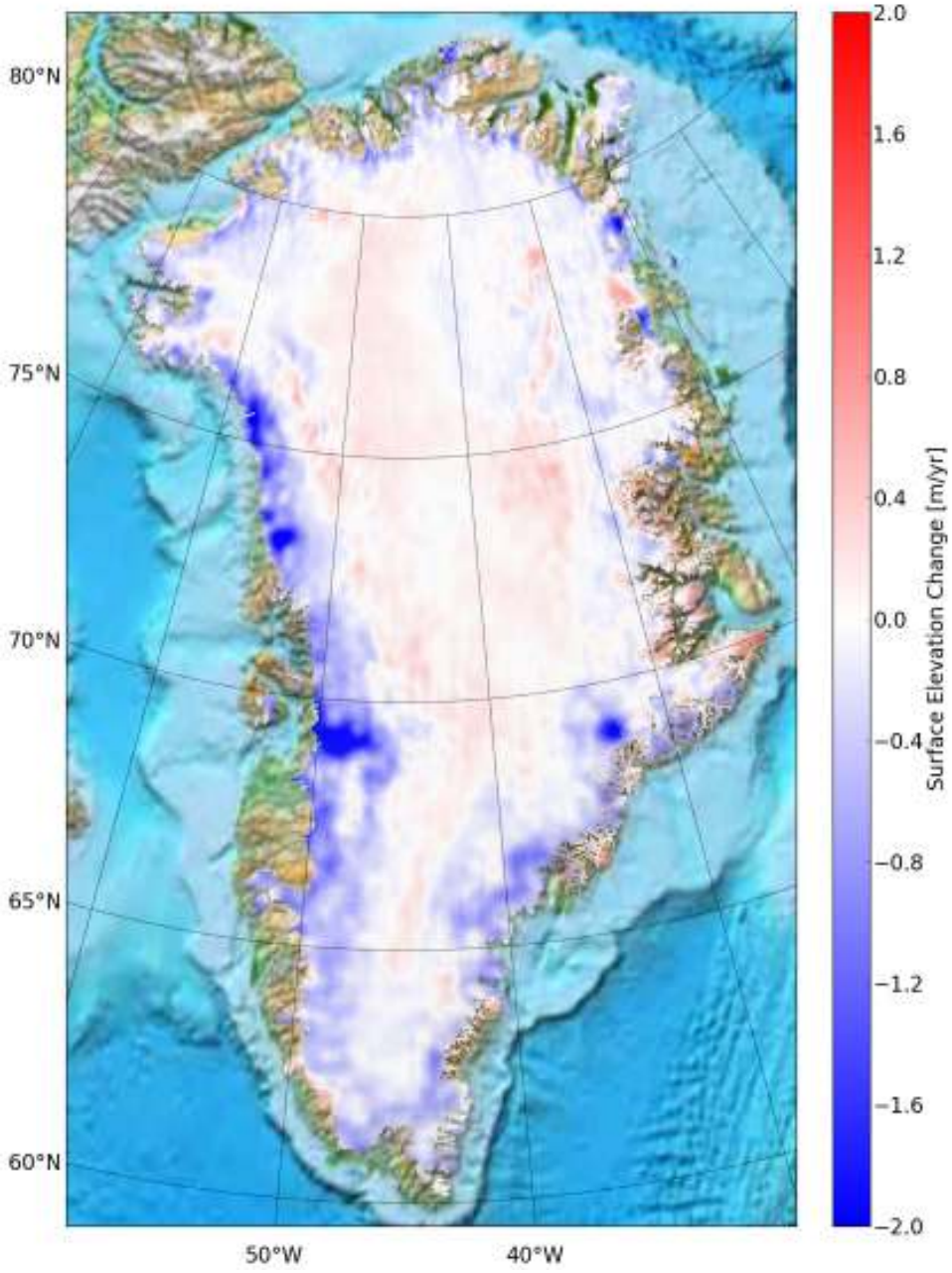

Figure 9.11 Surface elevation change of the Greenland Ice Sheet from 2010-2014 estimated from CryoSat-2 observation. Surface elevation changes estimated from the combination of the crossover and plane-fitting method using least-squares collocation

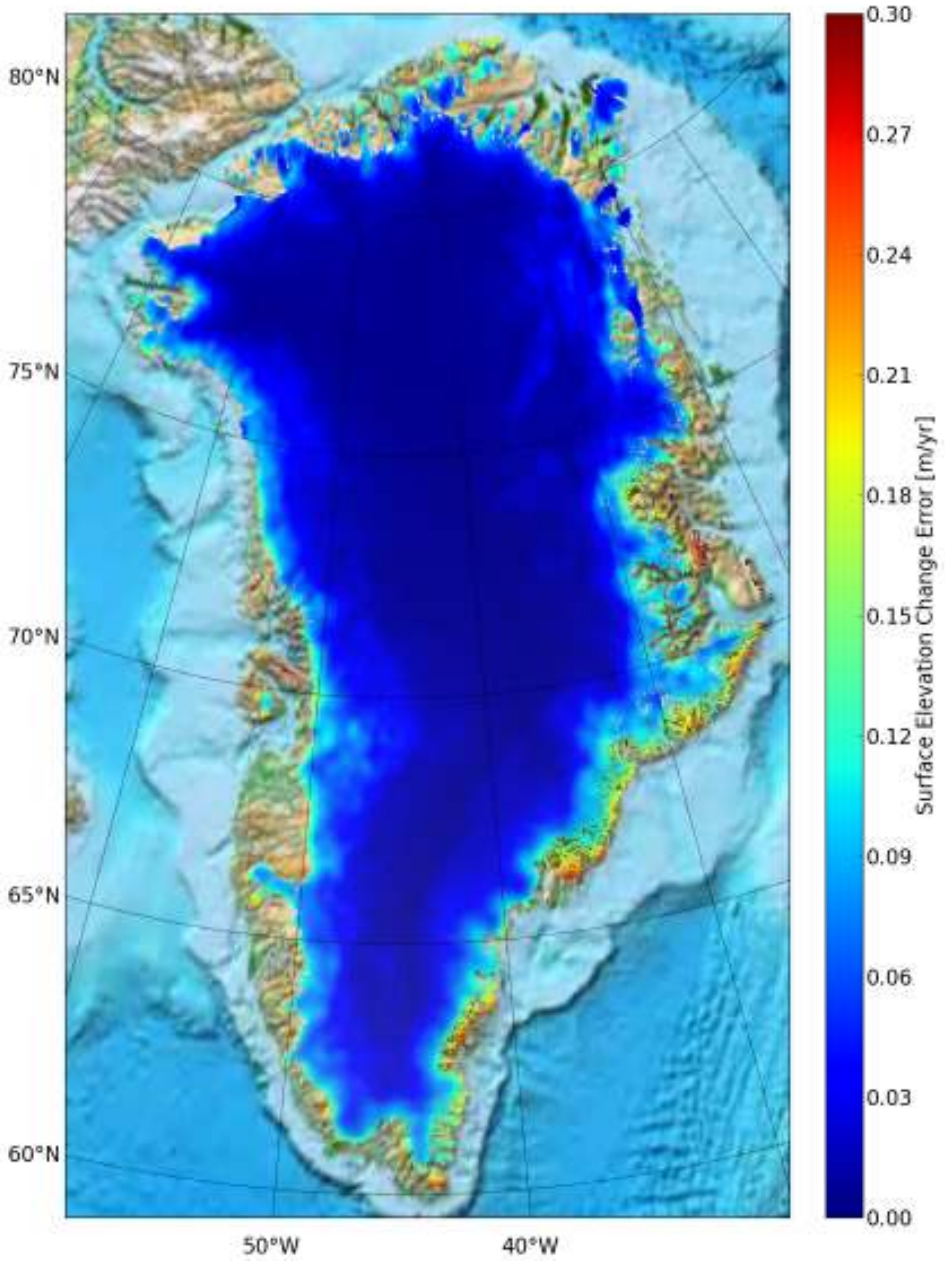

Figure 9.12 Least-Squares collocation interpolation error from the CryoSat-2 estimated elevation changes from 2010-2014.

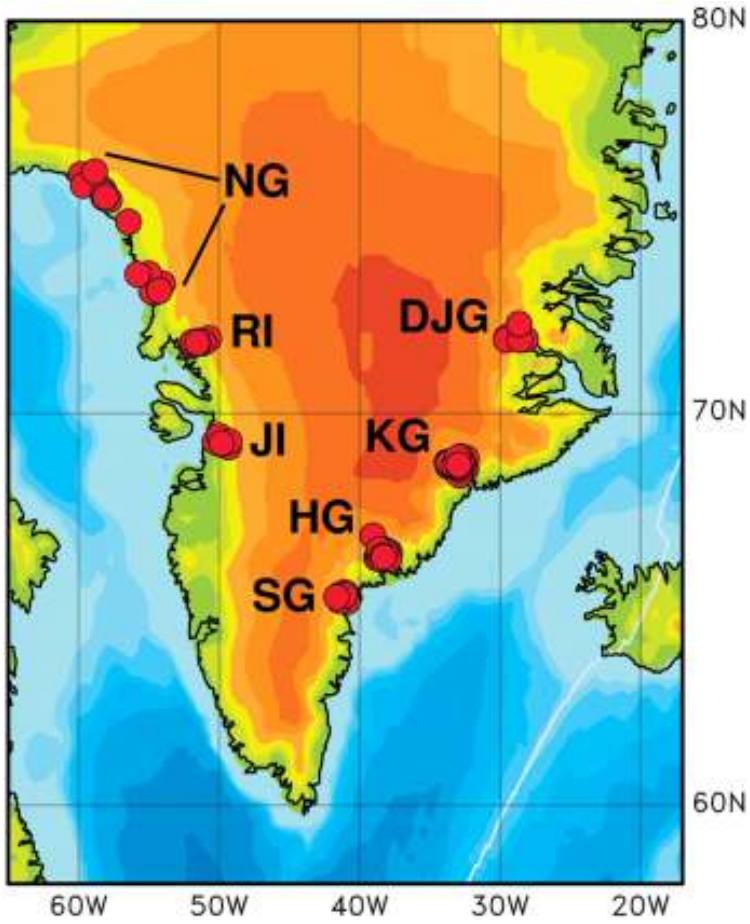

Figure 9.13 Locations of Greenland's major outlet glaciers. Abbreviations denote the following glaciers: DJG, Daugaard Jensen Glacier; KG, Kangerdlugssuaq Glacier; HG, Helheim Glacier; SG, southeast Greenland glaciers; JI, Jakobshavn Isbrae; RI, Rinks Isbrae; NG, northwest Greenland Glaciers. Image credit (Ekström et al., 2006)

10 Volume change of the Greenland Ice Sheet

The gridded surface elevation changes estimated in Fig. 9.11 are used here to estimate the total volume change of the Greenland Ice Sheet. The volume change can be estimated by summing all elevation change elements in the gridded product and multiplying them with their corresponding area, according to:

$$\left[\frac{\Delta V}{\Delta t}\right] = \sum_{i=1}^{N} \left(\left[\frac{\Delta H}{\Delta t}\right]_i \times \Delta A_i \right) \tag{10.1}$$

where $\left[\frac{\Delta V}{\Delta t}\right]$ is the total estimated volume change, $\left[\frac{\Delta H}{\Delta t}\right]_i$ is the individual elevation change value in every grid cell and ΔA_i is the area of each grid cell.

As the observations are gridded using a geographical coordinate system the surface area of each grid cell changes with latitude. This means that grid cells are not of equal area and needs to be scaled with the latitude and the Earth's radius to obtain the correct area. This is done using spherical geometry and by assuming a spherical Earth, according to:

$$\Delta A_i = R_E^2 \cos(\phi_i) \Delta\lambda \Delta\phi \tag{10.2}$$

where R_E is the Earth's equatorial radius (6378.1370 km), ϕ_i is the latitude of the grid cell, $\Delta\lambda$ is the longitudinal spacing of the grid (0.025°) and $\Delta\phi$ is the latitudinal spacing of the grid (0.01°). Where all angles are in radians.

Using the approach detailed in this section, a total volume change of -224±25 km^3a^{-1} of the Greenland Ice Sheet is observed for the time period of 2010-2014. The estimated volume change of -224 km^3a^{-1} is well in line with previous estimates from studies such (Ewert et al., 2012; Shepherd et al., 2012; Sørensen et al., 2011).

It is however 41% smaller than the value of -375 km^3a^{-1} estimated by (Helm et al., 2014) for the period of 2011-2014. One should expect that the value in this thesis should be more negative, as the positive bias introduced from the 2012 melt event still persists, seen in Fig. 9.3 for slope less than 0.1°. The residual effect of the melt even would effectively make the overall volume change less negative. Assuming an average residual signal of 0.05 ma^{-1} and a zero elevation change over the interior part of the ice sheet, defined as the total area above 2000 m, this can correspond to a false volume change contribution on the order of 54 km^3a^{-1}.

	Volume change (km^3a^{-1})	Error (km^3a^{-1})
GrIS	-224	25

Table 10.1 The Greenland Ice Sheet total volume change over the period of 2010-2014 estimated from CryoSat-2 elevation changes.

The main purpose of this thesis is to determine accurate and robust elevation and elevation changes over land ice using CryoSat-2. Therefore only a simple model is used to determine the volumetric error, which is based on the relative precision, elevation change and interpolation error. To estimate the total volumetric error one first need to determine the total elevation change error. For the purpous of this thesis the total elevation change error is defined as the root-square-sum (RSS) of the CryoSat-2 measurement, the elevation change and least-squares collocation interpolation error, according to:

$$\varepsilon_{tot} = \sqrt{\left(\frac{\varepsilon_{cs}}{\sqrt{N}}\right)^2 + \left(\frac{\varepsilon_{dh/dt}}{\sqrt{N}}\right)^2 + \left(\frac{\varepsilon_{int}}{\sqrt{N}}\right)^2} \tag{10.3}$$

where ε_{tot} is the total elevation change error, ε_{cs2} is the measurement error, $\varepsilon_{dh/dt}$ is the elevation change error and ε_{tot} is the interpolation error. N is the number of correlation bins determined from the correlation length of the elevation changes. A_{tot} is the total glaciated area. The correlation area bin factor is determined from the correlation length of the data, and used to divided the total area of the ice sheet into bins. Where the correlation bin factor is defined as $N = A_{tot}/\rho^2$, where ρ is the correlation length of the elevation changes. The calculation of this error budget is similar to the method used by (Nilsson et al., 2014).

The CryoSat-2 measurement error ε_{cs} is defined as the relative precision obtained from the crossover analysis, from Table. 11.4 in Section. 11.3.1, averaged over the time span of the data set.

$$\varepsilon_{cs2} = \frac{\sigma_{cs}}{\Delta t} \tag{10.4}$$

where σ_{cs} is the standard deviation of the crossover with a time span less than 30 days and Δt is the time span of the data.

The elevation change error $\varepsilon_{dh/dt}$ was estimated as the standard deviation of the differences between the ATM-derived elevation changes and the CryoSat-2 elevation change product in Table. 11.6 in Section. 11.4. Hence, it is a combined value for both the crossover and plane-fit method.

The interpolation error ε_{int} of the elevation changes are estimated as the average standard deviation of the estimated interpolation error from the collocation procedure.

$$\varepsilon_{int} = \sqrt{\sum_{i=1}^{N} \left(\frac{\sigma_i^2}{N} \right)} \tag{10.5}$$

where σ_i are the individual error estimates for each prediction inside the ice mask and N the total number of prediction inside the mask.

The total volumetric error ε_{vol} can then be estimated as follows:

$$\varepsilon_{vol} = \varepsilon_{tot} A_{tot} \tag{10.6}$$

where A_{tot} is the total are of the Greenland ice sheet.

For this calculation the following errors and area where assumed; $\sigma_{cs} = 0.075$ ma^{-1}, $\sigma_{dh/dt} = 0.27$ ma^{-1}, $\sigma_{int} = 0.035$ ma^{-1}, $A_{tot} = 1.75{\times}10^6$ km^2 and a correlation length of $\rho = 65$ km. The total area of the Greenland Ice Sheet was determined by summing the area elements estimated in Eq. 10.2 over glacial terrain.

11 Validation and Comparison

In this section the results of the validation procedure is presented and discussed. The estimated surface elevations from the two developed LRM and SARiN-mode processors are validated against contemporary airborne laser scanner data and crossover analysis. This is done to determine the absolute and relative precision and accuracy of the measured surface heights. Finally, the accuracy and precision of the generated gridded products of elevation and elevation changes are determined using contemporary surface heights and height changes. This allows, in the end, for a extensive and quantitative comparison of the quality between the two different CryoSat-2 processing chains, allowing for the determination of possible improvements for the ESA processing chain.

For the purpose of this study the ESA derived surface elevations and elevation changes, both gridded and point data, have undergone the same processing and are bound by the same constraints as the DTU processing . This has been done to reduce difference in the products due to, i.e. harder outlier editing and so on, This means that the ESA products might not be fully optimal as it could have been. However, the level of editing and processing is a sign of quality itself, where products in need of extensive editing are usually indicative of poorer quality.

11.1 ESA Level-2 Baseline-B data

In this thesis the ESA level-2 (L2) baseline-B elevation product have been used for the validation and the comparative study. Surface elevations with a ground sampling of 20 Hz was extracted over Greenland for the period of 2010-2014. The 20 Hz elevations were corrected for geophysical errors for land ice, as described in (Bouzinac, 2014). In this process the backscatter coefficient and peakiness parameter, describing the waveform shape, was also extracted. Please not that for the ESA L2 baseline-B product they are the only available waveform parameters, in contrast to the four estimated in this thesis.

The ESA L2 data are available via FTP: *ftp://science-pds.cryosat.esa.int*, given user name and password from ESA.

11.2 Airborne Laser Scanner data

In this section the airborne laser scanner data used to validate the CryoSat-2 derived surface heights and height changes are presented. The airborne laser scanner data consists of two main mission; "Operation IceBridge Airborne topographic Mapper" (ATM) and the "CryoVEx" mission (CRY). The ATM mission will further be used to derive the uncertainty of the estimated surface heights changes of the Greenland Ice Sheet.

11.2.1 Operation IceBridge Airborne Topographic Mapper

NASA's "Operation IceBridge" mission was initiated in 2009 to collect airborne remote sensing data over the Earth's polar areas to bridge the gap between ICESat and the upcoming ICESat-2. The mission is planned to continue for a 6-year period or probably until the launch of ICESat-2, which is planned for in early 2017. The airborne mission consists of several instrument payloads, such as; laser scanner, accumulation radar, snow radar, optical imaging sensors, magnetometer, Ku-band radar, infrared pyrometer and other meteorological instruments.

For this thesis the laser scanner payload called the "Airborne Topographic Mapper" (ATM) has been used to validate the derived surface elevations from CryoSat-2. ATM is used for topographic mapping of glaciated terrain, such as ice sheet, ice caps, glaciers and also sea ice. It operates at a wavelength of 532 nm with a PRF of 5 kHz. The measurements are made using a conical point scanner with a 22.5° scan angle along the aircraft's flight line measuring 5000 points per second. The nominal across-track swath resolution is approximately 400 m with an average point density of one laser-shot per 10 m^2. There also exits a narrow swath scanning laser scanner (NATM) with an angular swath width of 2.7°. This produces a ground swath of roughly 45 with a PRF of 3 kHz.

The reported vertical surface elevation accuracy for the ATM systems is on the order of 10 cm and better, where the surface heights are referenced according to the WGS-84 reference ellipsoid (Krabill, 2014).

The ATM laser scanner data products used in this thesis are the following:

- **IceBridge ATM L2 Icessn Elevation, Slope, and Roughness** from NASA DAAC at the National Snow and Ice Data Center, available at (http://nsidc.org/data/ilatm2.html)

- **IceBridge Level-4 ATM Surface Elevation Rate of Change** from NASA DAAC at the National Snow and Ice Data Center, available at (http://nsidc.org/data/idhdt4)

11.2.2 CryoVEx

The CryoVEx campaign started in 2003 and is planned to continue until at least 2015. The purpose of the mission is to gather a multitude of ground-truth observations in the Arctic region for the purpose of validating the observations from the CryoSat-2 mission. The mission provides measurements of elevations over glaciated terrain, mostly over well studied ice caps, and sea ice. The campaign is particularly aimed at understanding the miscellaneous error sources and the interaction of the radar signal with the surface. The CryoVEx mission is joint venture between DTU Space, Alfred Wegener Institute (AWI) and other European and Canadian institute.

The CryoVEx payload consists of airborne radar and laser altimetry, EM-sounding and in-situ observations. For the purpose of this thesis the focus will solely on the laser altimeter carried by the aircraft.

The airborne laser scanner instrument is a Riegl LMS Q-240i type laser scanner operating at a wavelength of 904 nm with a PRF of 10 kHz. It provides both linear and parallel scan lines with a 60° scan angle. The aircraft altitude is roughly 350 m above the ground with a average ground speed of 250 km/h, yielding a horizontal resolution of 0.7×0.7 m and across-track swath of 350 m. The aircraft location is determined using GPS and attitude (pitch, role and heading) is recorded by inertial navigation system (INS). Calibration of the laser scanner is performed by multiple overflight over specific building with known high-precision coordinates.

The vertical accuracy of the laser scanner system is estimated to be on the order of 5-10 cm, depending on the quality of the GPS solution. The measures surface heights are given relative to the WGS-84 reference ellipsoid (Skourup et al., 2013).

The CryoVEx laser scanner data used for this thesis consist of laser derived elevations which have been re-sampled to a resolution of 5 m, acquired over Austfonna in 2011 and 2012. These two data sets are available in-house here at DTU Space, for more information please see (Skourup et al., 2013).

11.3 Validation of surface elevations and gridded products

The derived surface heights from the two CryoSat-2 processors developed in this thesis where rigorously validated, using airborne laser scanner data and crossover analysis over several types of glacial terrain. The absolute precision and accuracy is determined using airborne laser scanner data and the overall relative accuracy and precision using crossover analysis.

The results from this validation procedure is then compared to the current ESA L2 surface height product to judge the improvement of the new processing chains. For consistency this is done for the same time period and location using the same validation methodology. The accuracy and precision of the derived CryoSat-2 DEM will also be determined in this step, and compared to a corresponding identical processed DEM generated from the ESA L2 product. This to be able to judge improvement in precision and accuracy of the two products.

The two processing chains were individually validated over different types of glacial terrain. The SARiN processor has been validated over both ice caps, specific ice sheet regions and over the entire continental ice sheet. The LRM processor was validated in the interior parts of the Greenland ice sheet, wherever laser scanner data are available. Further, as less airborne validation data are available in the interior parts the ice sheet, due to the larger focus on the marginal areas of the ice sheet, a comprehensive crossover analysis was also undertaken. This was done to obtain a larger continental wide perspective on the relative accuracy and precision of the LRM-processor.

Three main parameters are used to determine the overall quality of the height measurements. These three parameters consist of the accuracy and precision determined from the difference of overlapping observations and the residual slope-induced error. The residual slope-induced error is used to judge the quality of the relocation method or the range correction, due to range error introduced by surface slope, see Section. 4.3.6.

11.3.1 Surface elevations

The validation procedure to estimate the accuracy and precision of the CryoSat-2 derived surface heights from both the DTU and ESA processors. The accuracy is defined as the mean value of the height residuals and the precision as the standard deviation around this mean value. The residual slope error is

determined by fitting a trend to the height residuals versus slope, where the rate is taken as the measure of the residual-slope error.

The validation procedure can be summarized in the different steps below.

1. Extract CryoSat-2 data over glacial terrain, using polygon or ice masks.
2. Find all airborne laser scanner data points around a 50 m search radius around every CryoSat-2 point
3. Compute the difference between the CryoSat-2 (H_{cs}) and the airborne heights (H_{ab}), according to $dH = H_{cs} - H_{ab}$
4. Remove gross outliers in dH
5. Accuracy is determined from the mean of the derived height residuals (dH)
6. Precision is determined from the standard deviation of the height residuals (dH)
7. Estimate the residual slope-error by binning dH as a function of surface slope, in 0.05° degree bins. Where the residual slope error is estimated as the rate of a linear fit between 0-0.5° for LRM and 0-1° for the SARiN-mode.

The airborne campaigns are usually flown in the late spring every year, usually in the months of April, due to the more favourable weather conditions. This means that to compare derived surface heights they need to be close both in time and position. However, due to the sub-cycle of 30 days of many radar remote sensing satellites only a few ground tracks are available over a specific area at a specific time. This puts constraints on the statistical robustness of the analysis, as one might have data close in time but not enough observations to obtain a good statistical measure of the accuracy and precision. This can be helped by increasing the search radius, thus including more data in the analysis. However, this is not recommended as increasing the search radius introduces a slope error component in the estimation, effectively biasing the results. This can be overcome by de-trending the data using a priori DEM or solving for the slope in the estimation. However, the DEM might not be good enough or there might not be enough data points inside the search radius to solve for the topographical slope.

In this thesis a trade-off has been chosen between location and acquisition time to try to obtain enough samples to make a robust estimate of the absolute precision and accuracy. This was done by using a search radius of 50 m, to reduce slope errors, and a total of 5-months of CryoSat-2 centred around the airborne acquisition date. The inclusion of more data in the analysis,

by including more months, increases the number of overlapping observations. However, caution has to be taken not to include to many months, as this analysis assumes that the glacial topography should be relatively stable.

To determine this a small case study was undertaken on Barnes ice cap to judge the change in elevation over the 5-month interval on monthly basis. The data was de-trended using a 150 m resolution DEM (CDEM-Canadian Digital Elevation Model *http://www.geobase.ca/geobase/en/data/cded/*) and the mean of the height residuals was computed for each month. The rate of change was then estimated by fitting a trend to the average values of the five months, which gave a trend of 6.5±11 cm/month. This value estimated over 5-months give a change in elevation of 32.5 cm which does have a bearing on the absolute accuracy. However, for the purpose of this thesis the absolute accuracy is not as important as the relative accuracy and precision, as the main purpose of this part of the study is to compare our DTU derived heights with those estimated by the ESA product.

In Table. 11.1 the results of the validation procedure can be found. It is clear from these tables that the overall accuracy and precision has been increased using the new developed SARiN-processor compared to the ESA-processor. A average improvement of roughly 63% can be seen for the accuracy and 42% for the precision over several ice caps and the roughed area of Jakobshavn, in South-West Greenland.

The SARiN processor shows a residual slope-induced error when comparing the difference in surface heights between the CryoSat-2 and airborne data. This residual error is however much smaller than the one affecting conventional altimetry, where the residual slope-induced error post slope correction is still on the order of several meters, seen in Table. 11.2. The residual slope error in the DTU-product is also on the order 25% smaller than the ESA-product, indicating better handling of phase-filtering, phase-ambiguities and improved geocoding. For the LRM-mode this was restricted to 0.5° or surface slope and 1° for the SARiN mode, as these are the slope-intervals containing the majority of the observations.

The validation results from the LRM-mode over the interior parts of Greenland also show a remarkable improvement, in both precision and accuracy, of the estimated surface elevations. Where the accuracy has improved, if using the 2011-2013 estimates in Table 11.2, with 50% and the precision with 13%. The largest difference is observed in the residual slope-error where an improvement of almost 72% is observed, using the values from the 2011-2013 estimates.

DTU-SARiN	Year	Mean	Std.dev	Max	Min	N	Slope	Mission
Penny	2013	-0.20	0.75	1.90	-2.10	75	0.07	ATM
Barnes	2011	-0.31	0.44	1.00	-1.40	139	0.40	ATM
Devon	2011	-0.35	0.34	0.61	-1.16	22	0.47	ATM
Devon	2012	0.10	0.67	1.71	-1.51	105	0.28	ATM
Austfonna	2011	-0.55	0.45	0.52	-1.85	183	0 10	CRY
Austfonna	2012	-0.60	0.46	0.82	-2.20	248	0.10	CRY
Jakobshavn	2011	0.00	0.98	3.30	-2.91	880	0.48	ATM
Jakobshavn	2012	-0.31	0.66	2.28	-2.30	452	0.53	ATM
Jakobshavn	2013	-0.29	0.37	1.14	-1.40	391	0.48	ATM
ESA-SARiN	Year	Mean	Std.dev	Max	Min	N	Slope	Mission
Penny	2013	-0.70	0.61	1.00	-1.98	40	0.12	ATM
Barnes	2011	-0.82	0.73	1.19	-2.86	149	0.00	ATM
Devon	2011	-0.50	0.69	1.30	-1.70	28	1.44	ATM
Devon	2012	-1.14	0.66	1.16	-3.40	170	0.32	ATM
Austfonna	2011	-1.17	0.62	0.62	-3.62	260	0.11	CRY
Austfonna	2012	-1.55	1.11	1.35	-5.00	256	0.62	CRY
Jakobshavn	2011	-0.50	1.76	4.70	-6.15	1814	0.17	ATM
Jakobshavn	2012	-0.74	1.46	3.80	-5.70	964	0.64	ATM
Jakobshavn	2013	-0.58	1.22	3.14	-4.47	941	0.31	ATM

Table 11.1 Described the statistics of the estimated height differences over several Arctic ice caps and Jakobshavn, between airborne and CryoSat-2 observations for the SARiN mode.

A larger difference in accuracy was expected as the magnitude of the accuracy depends on the retracking point, which is 20% for the retracker used in this study. The ESA L2 product is probably using something closer to 50%, judging from the improvement in accuracy. However, this is more speculation than facts, as we to date do not fully know how the retracker is implementation in the ESA L2 product, as this has not become public. The smaller improvement in precision is also expected, as the the LRM-mode operated in relatively smooth terrain where most observation sits between 0-0.5° slopes.

DTU-LRM	Mean	Std.dev	Max	Min	N	Slope	Mission
2011	-0.56	0.57	1.49	-2.90	5276	2.19	ATM
2012	-0.40	0.64	1.94	-2.70	7070	3.33	ATM
2013	-0.29	1.13	4.10	-4.92	2667	2.97	ATM
2011-2013	-0.46	0.78	2.43	-3.45	35569	1.96	ATM
ESA-LRM	Mean	Std.dev	Max	Min	N	Slope	Mission
2011	-1.27	0.81	1.67	-3.30	4717	4.96	ATM
2012	-1.38	0.84	1.64	-3.65	4605	7.13	ATM
2013	-0.37	0.59	2.80	-2.40	2498	2.27	ATM
2011-2013	-0.91	0.90	2.16	-3.44	33027	5.10	ATM

Table 11.2 Describes the statistics of the height differences between the airborne and CryoSat-2 heights for the LRM-mode in the DTU and ESA derived surface height over the interior parts of the Greenland Ice Sheet. The 2011-2013 results are estimated by combing all 5-months CryoSat-2 data from the different years with the corresponding airborne data, giving roughly an average value of the three data sets.

The validation results from the continental wide analysis of the SARiN-mode over the Greenland ice sheet is inline with what is observed on the ice caps (Table. 11.1). Here, a 49% improvement in accuracy and 39% in precision is observed when using the 2011-2013 values estimated in Table. 11.3. The residual slope-error shows an improvement of 18%, which is less than what is observed on the ice caps (Table. 11.1) which shows an improvement of 34-52%, depending on the calculation. However, ice sheet show less roughed terrain than many ice caps, which should have a converging effect on the residual slope error between the two products. This as difference in geolocation algorithm have less influence on the estimated echo-location in these flatter areas.

DTU-SARiN	Mean	Std.dev	Max	Min	N	Slope	Mission
2011	-0.56	0.67	1.56	-2.60	7605	0.71	ATM
2012	-0.44	0.55	1.49	-2.10	9377	0.70	ATM
2013	-0.38	0.29	0.79	-1.24	5026	0.32	ATM
2011-2013	-0.59	0.71	1.86	-2.80	58718	0.46	ATM
ESA-SARiN	Mean	Std.dev	Max	Min	N	Slope	Mission
2011	-1.10	1.10	2.10	-4.50	8742	0.83	ATM
2012	-1.10	0.11	2.25	-4.80	11262	1.10	ATM
2013	-0.77	0.65	1.40	-3.20	5788	0.65	ATM
2011-2013	-1.15	1.16	2.40	-5.00	68860	0.56	ATM

Table 11.3 Describes the statistics of the height differences between the airborne and CryoSat-2 heights for the SARiN-mode in the DTU and ESA derived surface height over the interior parts of the Greenland Ice Sheet. The 2011-2013 results are estimated by combing all 5-months CryoSat-2 data from the different years with the corresponding airborne data, giving roughly an average value of the three data sets.

To compare the relative accuracy and precision of the DTU and ESA product the ESA L2 crossovers height difference where estimated in the same manner as for the DTU product. From which the accuracy and precision was computed and compared to the DTU product.

Comparing the relative accuracy and precision of the DTU product with the ESA product and overall improvement can be found, as seen in Table. 11.4. Table. 11.4 shows a 50% improvement in accuracy, defined by the A/D-bias, and a 60% improvement in the relative accuracy. This when averaged over the entire Greenland ice sheet over the period of 2010-2014.

Figure 11.1 shows the relative accuracy and precision as a function of surface slope. Here good agreement between the two products exits up to roughly 0.3-0.4°, where they afterwards starts to diverge. From Fig. 11.4 it can be seen that the DTU product outperformed the ESA L2 product over the entire slope interval, up to 1°. Where a difference of up to 2 m in precision can be observed in the higher sloping areas.

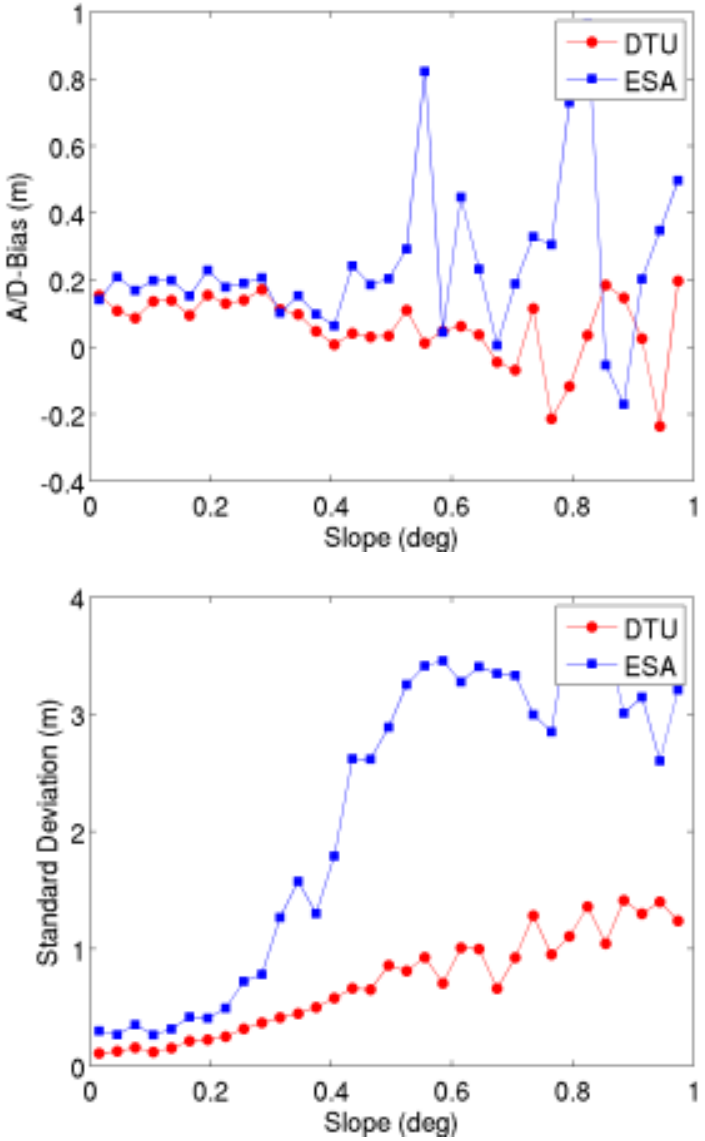

Figure 11.1 Shows the relative accuracy (left) and the relative precision (right) of the measured surface heights over Greenland from the DTU and ESA products

Product	Mean (m)	Std.dev (m)	Max (m)	Min (m)	N
DTU	0.11	0.29	1.41	0.11	40705
ESA	0.21	0.73	0.38	0.27	29799

Table 11.4 The relative accuracy (Mean) and relative precision (Std.dev) average over the of the DTU and ESA elevation products. Where the maximum (Max) and minimum (Min) values indicate the range of the relative precision, and (N) the number of crossover with a Δt<30 days used for the estimation.

When estimating the ESA crossover height difference for the comparative analysis a heavier outlier rejection procedure needed to be applied to obtain comparative results. This can be observed in the number of crossovers used for computing the statistics in Table. 11.4, which is also an general indicator of the quality of the products.

11.3.2 Digital Elevation Model

The accuracy and precision of the generated DEM in Section. 11.3.1 is estimated to determine the quality of the gridded product. The estimated uncertainty is then compared to a DEM generated, using the same methodology and processing, from the ESA L2 product from the same time period. Both DEMs are height adjusted prior to the gridding procedure with the mean bias value (Mean) estimated in 11.2 and Table. 11.3 from the 2011-2013 ATM data.

The validation is performed using the combined ATM surface heights measured during the period 2011-2013. This is done as the DEM consists of an ensemble of CryoSat-2 surface heights spanning a 4-year time period 2010-2014. The validation procedure of the DEM can be summarized into the main following steps for the determination of the accuracy and precision.

1. Estimate the DEM surface height at each ATM location using bilinear interpolation
2. Compute the difference in surface height $dH = H_{dem} - H_{atm}$ from the CryoSat-2 and ATM observations.
3. Reject all height differences larger than 100 m
4. Apply 3σ outlier rejection filter to remove gross outliers
5. Estimate the mean and standard deviation of the residuals

From Table. 11.5 the estimated uncertainty of the DEM generated from

DTU processed CryoSat-2 surface heights can be found. The estimated uncertainty of the produced DEM is estimated to 3.1±15.7 m, when comparing to airborne laser scanner data from 2011-2013. The generated DEM from ESA L2 surface height show roughly factor of two higher uncertainty but a somewhat higher precision. These number are in line with the uncertainty derived for (Helm et al., 2014) Greenland DEM, generated from 2011-2013 data. The results of this validation and further comparison points to the CryoSat-2 great potential for deriving highly accurate and contemporary DEMs.

Product	Mean (m)	Std.dev (m)	Slope-error (m/deg)
DTU	3.1	15.7	8.9
ESA	6.1	14.3	11.0

Table 11.5 The estimated uncertainty and quality of the DEMs derived from the DTU and ESA L2 surface elevation products.

11.4 Validation of surface elevation changes

The estimated CrySat-2 gridded elevation changes from 2010-2014 were validated using IceBridge ATM derived elevation changes from 2011-2013. ATM elevation changes were used due to (1) the contemporary time period and (2) the high accuracy of the estimated elevation changes. This as the estimated ATM elevation change error have an accuracy of roughly 10 cma^{-1} or better (Krabill et al., 2002). Finally the precision and accuracy of the gridded surface elevation changes are compared to ESA-derived gridded elevation changes for the same time period.

The gridded CryoSat-2 elevation changes weere interpolated to the locations of the ATM flight-track, using bilinear interpolation, and the differenced according to; $\Delta dH = dH_{cs} - dH_{atm}$. The estimated elevation change residuals where edited visually for outlier using and iterative 3σ filter until no gross outlier where found. The precision and accuracy of the CryoSat-2 derived elevation changes for the ESA and DTU product was then computed, which are shown in Table. 11.6.

Table. 11.6 shows good agreement between CryoSat-2 estimated elevation changes compared to ATM derived elevations changes. The derived elevtion change error for the the DTU product is on the order of 27 cma^{-1} compared to the ESA derived error of 31 cma^{-1}, giving and RMS-difference of 4 cma^{-1}. A higher correlation between the CryoSat-2 derived and ATM derived elevation

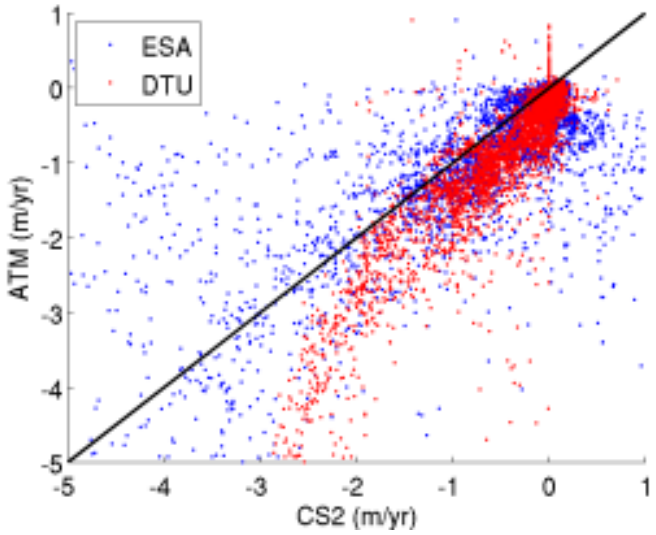

Figure 11.2 CryoSat-2 versus ATM elevation changes estimated from the gridded ESA and DTU products.

changes are also observed for the DTU product compared to the ESA product. Here, a correlation of $\rho_{dtu} = 0.93$ is observed for the DTU product compared to a correlation of $\rho_{esa} = 0.80$ for the ESA product. The ESA product does however show a lower elevation change bias, on the order of 13 cma^{-1}, compared to the DTU product. The difference between the ATM and CryoSat-2 products can be seen in Fig. 11.2.

Product	Mean	Std.dev	Max	Min	R^2	N
DTU	0.21	0.27	1.53	-0.61	0.93	228,858
ESA	0.13	0.31	2.44	-3.00	0.80	228,858

Table 11.6 Statistical comparison between CryoSat-2 gridded products with ATM-derived elevation changes from 2011-2013, where the values are in (ma^{-1}). The mean value indicates the accuracy, the standard deviation the precision, R^2 the correlation between the ATM and CryoSat-2 elevation changes and N the number of comparison points.

The elevation change validation procedure shows the same overall results as the validation of the surface elevations, where the DTU product show both lower standard deviation and higher correlation. However, the difference in elevation changes are smaller compared to the differences seen in the surface height estimation. This result is expected as the estimation of elevation changes

are of a relative nature, cancelling out larger differences.

It should be noted that the correlation for the ESA product can be increased by harder editing of the overall product. A quick test show that harder editing can increase the correlation up to 0.89 with an increase in bias from 0.13 to 0.21 ma^{-1}. This however required the removal of a total of 7.4% of the data for the ESA product, compared to 4.2% for the current editing of the DTU product.

12 Summary and conclusion

The research topic of this Ph.D thesis has been to determine and improve the estimation of present-day elevation changes of the ice covered land regions in the Arctic and the North Atlantic using both satellite and airborne altimetry data sets. The present-day elevation change and also ice-volume/mass change have been determined using ICESat and CryoSat-2 data, and are presented here in the form of this thesis and together with the articles; (Nilsson et al., 2015a) and (Nilsson et al., 2015b). For the purpose of determining the present-day elevation change of land ice (in the Arctic and North-Atlantic region) a central part of this thesis has been to develop software and algorithms for the retrieval of surface elevations and elevation changes, with a specific focus on the CryoSat-2 mission.

The software consists of a new set of processing chains for the retrieval of surface heights for the CryoSat-2 LRM and SARin-mode over both smooth and complex glacial terrain. For the SARin-mode, which is the most advanced mode, this has consisted of the development of a new type of retracker, implementation of advanced waveform and phase-filtering and automatic detection and correction of phase-ambiguities. For the LRM-mode an optimized threshold retracker was developed for the retrieval of surface and surface elevation changes over the interior parts of the ice sheets, including the application of advanced waveform filtering and slope-error correction. For both modes additional information, to the ESA L2 product, about the shape of the waveforms was also extracted to allow for more precise characterization of the ice sheet scattering properties.

The software written for the retrieval of surface elevations consists of several thousands of lines of code and is mostly written in MATLAB. The code is optimized for speed by the usage of parallel processing and is very powerful. It can, given the computer power, process 4-years of CryoSat-2 L1b data over Greenland in less than 12 hours, where roughly 75% of the processing time is devoted to the SARin processor, due to its more advanced design than the LRM processor.

In addition to the software written for the retrieval of surface heights over land ice, a considerable amount of effort was also undertaken to design algorithms for the detection of surface elevation changes. From which two algorithms optimized for the CryoSat mission was developed, based on satellite crossovers and fitting of rigid planes, designed to account for the changes in ice sheets scattering characteristics.

The retrieved surface elevations and elevation changes estimated from these processors have also been fully validated using airborne laser data over several types of glacial terrain in the Arctic region to characterize their errors. In parallel to this validation procedure, the ESA L2 processing chains were also validated and used in the inter-comparison. From this validation study it was shown that the new processing lines developed in this thesis performs better than the currently implemented ESA L2 baseline-B product. The new processing chain for the SARin-mode show and average improvement of roughly ∼50% in both accuracy and precision. The LRM-mode processing chain shows improvement in the average precision and accuracy on the order of roughly 40%.

The development of new surface elevation change algorithms have provided unprecedented coverage of the Greenland Ice Sheet, consisting of more than 17 million surface elevation change observations. The quality of these observation was estimated by comparisons to airborne laser derived elevation changes, which showed a correlation higher than 0.9 and good agreement in accuracy. The estimated elevation changes where used to determine the total volume change of the Greenland Ice Sheet producing and estimate of -224±25 km^3a^{-1}, in good agreement with other studies. This effectively proves that with enhanced processing the CryoSat-2 mission can be used for both large and small scale mass balance studies of ice sheet, ice caps and glaciers.

The work outlined in this thesis provides many possibilities for the improvement of the current ESA L2 processing chain to increase both the accuracy and precision for land ice studies using CryoSat-2. It is further the authors belief that the next coming years will provide new and exiting possibilities for improving the monitoring capabilities of CryoSat-2 and the cryosphere. This with the implementations of new techniques such as SWATH-mode processing (Gray et al., 2013) and inter-comparison to other new missions such as ICESat-2 and Sentinel.

13 Future work

During the time of this study new and interesting ideas for future work have emerged that should be useful for improving the estimation of surface elevations and elevation changes from satellite altimetry. However, also issues have during this time emerged that needs to be accounted for or solved in future work.

In the following section some of these ideas and issues are outlined:

- The introduction of SWATH-mode processing for CryoSat-2, pioneered by (Gray et al., 2013), provides exiting possibilities to improve the coverage in the marginal area of the ice sheet. The increased coverage of these regions will have the impact of greatly improving the SNR in elevation change analysis, allowing for mapping of the very small outlet glaciers in great detail.

- Improving the elevation change rate estimation in the plane-fit method by usage of a Kalman-smoothing filter approach to solve for the model coefficients of the topographical model.

- Reducing the search radius of the plane-fit method to reduce smoothing effect by investigation into the optimum number model parameters in the topographical model.

- Improve the merging procedure of crossover and plane-fit derived elevation changes, as the crossover derived rates have been proven, in this thesis, to be less affected by the Greenland 2012 melt even.

- Development of a physical retracker for the SARin and LRM-mode optimized to account for changes in the ratio between surface and volume scattering.

- Solving for the residual elevation bias from the 2012 melt event that was not fully accounted for in the regression model using the heavyside function.

- Improved understanding of the SARin and LRM waveforms interaction with the physical surface due the Doppler/Delay technique and firn density ratios.

- Estimation of firn properties over the interior parts of the ice sheets by means of radar-waveform inversion using CryoSat-2 superior spatial coverage to improve the observational SNR.

Some of these ideas will require a considerable amount of time and effort to solve, others are easier to implement. They do however provide important steps for improving of the current capabilities of radar-altimeter remote sensing over land ice and thus for mass balance studies.

Bibliography

W. Abdalati, W. Krabill, E. Frederick, S. Manizade, and J. Martin, C, Sonntag, J., Swift, R., Thomas, R., Wrighy, W., Yungel. Airborne laser altimetry mapping of the Greenland ice sheet : application to mass balance assessment. *Journal of Geophysics*, 34:391–403, 2002. ISSN 02643707. doi: 10.1016/s0264-3707(02)00048-0.

W. Abdalati, W. Krabill, E. Frederick, S. Manizade, C. Martin, J. Sonntag, R. Swift, R. Thomas, J. Yungel, and R. Koerner. Elevation changes of ice caps in the canadian arctic archipelago. *Journal of Geophysical Research: Earth Surface (2003–2012)*, 109(F4), 2004.

D. Alsdorf, C. Birkett, T. Dunne, J. Melack, and L. Hess. Water level changes in a large amazon lake measured with spaceborne radar interferometry and altimetry. *Geophysical Research Letters*, 28(14):2671–2674, 2001.

A. A. Arendt, K. A. Echelmeyer, W. D. Harrison, C. S. Lingle, and V. B. Valentine. Rapid wastage of alaska glaciers and their contribution to rising sea level. *Science*, 297(5580):382–386, 2002.

T. W. Armitage, D. J. Wingham, and A. L. Ridout. Meteorological origin of the static crossover pattern present in low-resolution-mode cryosat-2 data over central antarctica. 2014.

R. C. Bales, Q. Guo, D. Shen, J. R. McConnell, G. Du, J. F. Burkhart, V. B. Spikes, E. Hanna, and J. Cappelen. Annual accumulation for greenland updated using ice core data developed during 2000–2006 and analysis of daily coastal meteorological data. *Journal of Geophysical Research: Atmospheres*, 114(D6):n/a–n/a, 2009. ISSN 2156-2202. doi: 10.1029/2008JD011208. URL http://dx.doi.org/10.1029/2008JD011208.

J. Bamber, S. Ekholm, and W. Krabill. The accuracy of satellite radar altimeter data over the greenland ice sheet determined from airborne laser data. *Geophysical Research Letters*, 25(16):3177–3180, 1998.

J. L. Bamber and A. J. Payne. Mass balance of the cryosphere. *Observations and modelling contemporary and future changes. Cambridge*, 2004.

C. Bouzinac. *CryoSat Product Handbook*. European Space Agency, ESA, 2014. URL https://earth.esa.int/documents/10174/125272/CryoSat_Product_Handbook.

A. Brenner, R. Blindschadler, R. Thomas, and H. Zwally. Slope-induced errors in radar altimetry over continental ice sheets. *Journal of Geophysical Research: Oceans (1978–2012)*, 88(C3):1617–1623, 1983.

A. Brenner, J. DiMarzio, and H. Zwally. Precision and accuracy of satellite radar and laser altimeter data over the continental ice sheets. *IEEE Transactions on Geoscience and Remote Sensing*, 45(2):321–331, 2007. ISSN 01962892. doi: 10.1109/TGRS.2006.887172. URL http://www.scopus.com/inward/record.url?eid=2-s2.0-33846622393&partnerID=40&md5=ce653da33bba48bd55019cfd8bdb98ca.

R. Brooks, W. J. Campbell, R. O. Ramseier, H. R. Stanley, and H. J. Zwally. Ice sheet topography by satellite altimetry. 1978.

C. H. Davis. Growth of the Greenland Ice Sheet: A Performance\rAssessment of Altimeter Retracking Algorithms. *IEEE Transections on Geoscience and Remote sensing*, 33(5), 1995.

C. H. Davis. A robust threshold retracking algorithm for measuring ice-sheet surface elevation change from satellite radar altimeters. *IEEE Transactions on Geoscience and Remote Sensing*, 35(4):974–979, 1997a. ISSN 01962892. doi: 10.1109/36.602540.

C. H. Davis. A robust threshold retracking algorithm for measuring ice-sheet surface elevation change from satellite radar altimeters. *Geoscience and Remote Sensing, IEEE Transactions on*, 35(4):974–979, 1997b.

C. H. Davis and A. C. Ferguson. Elevation change of the antarctic ice sheet, 1995-2000, from ERS-2 satellite radar altimetry. *IEEE Transactions on Geoscience and Remote Sensing*, 42(11):2437–2445, 2004a. ISSN 01962892. doi: 10.1109/TGRS.2004.836789.

C. H. Davis and A. C. Ferguson. Elevation change of the antarctic ice sheet, 1995-2000, from ers-2 satellite radar altimetry. *Geoscience and Remote Sensing, IEEE Transactions on*, 42(11):2437–2445, 2004b.

C. H. Davis and H. J. Zwally. Geographic and seasonal variations in the surface properties of the ice sheets by satellite-radar altimetry. *Journal of Glaciology*, 39:687–697, 1993.

J. DiMarzio, A. Brenner, R. Schutz, C. Shuman, and H. Zwally. Glas/icesat 500 m laser altimetry digital elevation model of antarctica. boulder, colorado usa: National snow and ice data center. *Digital media*, 2007.

S. Ekholm, K. Keller, J. L. Bamber, and S. P. Gogineni. Unusual surface morphology from digital elevation models of the greenland ice sheet. *Geophysical research letters*, 25(19):3623–3626, 1998.

G. Ekström, M. Nettles, and V. C. Tsai. Seasonality and increasing frequency of greenland glacial earthquakes. *Science*, 311(5768):1756–1758, 2006.

H. Ewert, A. Groh, and R. Dietrich. Volume and mass changes of the greenland ice sheet inferred from icesat and grace. *Journal of Geodynamics*, 59:111–123, 2012.

E. Ferraro and C. Swift. Comparison of retracking algorithms using airborne radar and laser altimeter measurements of the Greenland ice sheet. *IEEE Transactions on Geoscience and Remote Sensing*, 33(3):700–707, 1995. ISSN 0196-2892. doi: 10.1109/36.387585.

T. Flament and F. Rémy. Dynamic thinning of Antarctic glaciers from along-track repeat radar altimetry. *Journal of Glaciology*, 58(211):830–840, 2012. ISSN 00221430. doi: 10.3189/2012JoG11J118.

R. Forsberg. A study of terrain reductions, density anomalies and geophysical inversion methods in gravity field modelling. *Scientific Report No.5 The Ohio State University*, page 129, 1984. URL http://oai.dtic.mil/oai/oai?verb=getRecord&metadataPrefix=html&identifier=ADA150788.

R. Forsberg and C. Tscherning. An overview manual for the gravsoft geodetic gravity field modelling programs. *Contract report for JUPEM*, 2008.

R. Forsberg, L. Sørensen, J. Fredenslund Levinsen, and J. Nilsson. *Mass loss of Greenland from GRACE, IceSat and CryoSat*. European Space Agency, ESA, 2013.

L.-L. Fu and A. Cazenave. *Satellite altimetry and earth sciences: a handbook of techniques and applications*, volume 69. Academic Press, 2000.

A. S. Gardner, G. Moholdt, J. G. Cogley, B. Wouters, A. A. Arendt, J. Wahr, E. Berthier, R. Hock, W. T. Pfeffer, G. Kaser, et al. A reconciled estimate of glacier contributions to sea level rise: 2003 to 2009. *Science*, 340(6134): 852–857, 2013.

R. C. Gonzalez, R. E. Woods, and S. L. Eddins. Digital image processing using matlab. *Dorling Kindersley*, 2004.

L. Gray, D. Burgess, L. Copland, R. Cullen, N. Galin, R. Hawley, and V. Helm. Interferometric swath processing of Cryosat data for glacial ice topography. *Cryosphere*, 7:1857–1867, 2013. ISSN 19940416. doi: 10.5194/tc-7-1857-2013.

V. Helm, a. Humbert, and H. Miller. Elevation and elevation change of Greenland and Antarctica derived from CryoSat-2. *The Cryosphere Discussions*, 8(2009):1673–1721, 2014. ISSN 1994-0440. doi: 10.5194/tcd-8-1673-2014. URL http://www.the-cryosphere-discuss.net/8/1673/2014/.

M. Horwath, B. Legrésy, F. Rémy, F. Blarel, and J.-M. Lemoine. Consistent patterns of antarctic ice sheet interannual variations from envisat radar altimetry and grace satellite gravimetry. *Geophysical Journal International*, 189(2):863–876, 2012.

I. M. Howat, I. Joughin, and T. A. Scambos. Rapid changes in ice discharge from greenland outlet glaciers. *Science*, 315(5818):1559–1561, 2007a.

I. M. Howat, I. Joughin, and T. A. Scambos. Rapid changes in ice discharge from greenland outlet glaciers. *Science*, 315(5818):1559–1561, 2007b.

I. M. Howat, B. E. Smith, I. Joughin, and T. A. Scambos. Rates of southeast greenland ice volume loss from combined icesat and aster observations. *Geophysical Research Letters*, 35(17), 2008.

I. M. Howat, A. Negrete, and B. E. Smith. The greenland ice mapping project (gimp) land classification and surface elevation data sets. *The Cryosphere*, 8(4):1509–1518, 2014. doi: 10.5194/tc-8-1509-2014. URL http://www.the-cryosphere.net/8/1509/2014/.

O. M. Johannessen, K. Khvorostovsky, M. W. Miles, and L. P. Bobylev. Recent ice-sheet growth in the interior of greenland. *Science*, 310(5750):1013–1016, 2005.

I. Joughin, S. B. Das, M. A. King, B. E. Smith, I. M. Howat, and T. Moon. Seasonal speedup along the western flank of the greenland ice sheet. *Science*, 320(5877):781–783, 2008.

I. Joughin, B. E. Smith, I. M. Howat, T. Scambos, and T. Moon. Greenland flow variability from ice-sheet-wide velocity mapping. *Journal of Glaciology*, 56(197):415–430, 2010.

R. Keith Raney. The delay/doppler radar altimeter. *IEEE Transactions on Geoscience and Remote Sensing*, 36(5):1578–1588, 1998. ISSN 01962892. doi: 10.1109/36.718861.

S. A. Khan, J. Wahr, L. A. Stearns, G. S. Hamilton, T. van Dam, K. M. Larson, and O. Francis. Elastic uplift in southeast greenland due to rapid ice mass loss. *Geophysical Research Letters*, 34(21), 2007.

S. A. Khan, L. Liu, J. Wahr, I. Howat, I. Joughin, T. van Dam, and K. Fleming. Gps measurements of crustal uplift near jakobshavn isbrae due to glacial ice mass loss. *Journal of Geophysical Research: Solid Earth (1978–2012)*, 115 (B9), 2010.

K. Khvorostovsky. Merging and analysis of elevation time series over Greenland ice sheet from satellite radar altimetry. *IEEE Trans. Geosc. Remote Sens.*, 50, 1(1):23–36, 2012.

W. Krabill. Icebridge narrow swath atm l1b elevation and return strength. version 2. [2015]. Technical report, 2014.

W. Krabill, W. Abdalati, E. Frederick, S. Manizade, C. Martin, J. Sonntag, R. Swift, R. Thomas, W. Wright, and J. Yungel. Greenland ice sheet: High-elevation balance and peripheral thinning. *Science*, 289(5478):428–430, 2000.

W. Krabill, W. Abdalati, E. Frederick, S. Manizade, C. Martin, J. Sonntag, R. Swift, R. Thomas, and J. Yungel. Aircraft laser altimetry measurement of elevation changes of the greenland ice sheet: Technique and accuracy assessment. *Journal of Geodynamics*, 34(3):357–376, 2002.

W. Krabill, E. Hanna, P. Huybrechts, W. Abdalati, J. Cappelen, B. Csatho, E. Frederick, S. Manizade, C. Martin, J. Sonntag, et al. Greenland ice sheet: increased coastal thinning. *Geophysical Research Letters*, 31(24), 2004.

P. Lacroix, B. Legrésy, R. Coleman, M. Dechambre, and F. Rémy. Dual-frequency altimeter signal from Envisat on the Amery ice-shelf. *Remote Sensing of Environment*, 109:285–294, 2007. ISSN 00344257. doi: 10.1016/j.rse.2007.01.007.

P. Lacroix, M. Dechambre, B. Legrésy, F. Blarel, and F. Rémy. On the use of the dual-frequency ENVISAT altimeter to determine snowpack properties of the Antarctic ice sheet. *Remote Sensing of Environment*, 112:1712–1729, 2008. ISSN 00344257. doi: 10.1016/j.rse.2007.08.022.

S. Laxon. Sea ice extent mapping using the ers-1 radar altimeter. *EARSeL Adv. Remote Sens*, 3:112–116, 1994.

B. Legresy. Using the temporal variability of satellite radar altimetric observations to map surface properties of the Antarctic ice sheet. *Journal of Glaciology*, 44(147):197–206, 1998. ISSN 00221430.

B. Legrésy and F. Rémy. Altimetric observations of surface characteristics of the Antarctic ice sheet. *Journal of Glaciology*, 43:265–275, 1997.

B. Legresy, F. Papa, F. Remy, G. Vinay, M. Van Den Bosch, and O. Z. Zanife. ENVISAT radar altimeter measurements over continental surfaces and ice caps using the ICE-2 retracking algorithm. *Remote Sensing of Environment*, 95:150–163, 2005. ISSN 00344257. doi: 10.1016/j.rse.2004.11.018.

V. Martin, C. Brenner, and A. Bindschadler. Analysis and Retracking of Continental Ice Sheet Radar Altimeter Waveforms. *Journal of Geophysics Research*, 88(C3):1608–1616, 1983.

M. McMillan, A. Shepherd, A. Sundal, K. Briggs, A. Muir, A. Ridout, A. Hogg, and D. Wingham. Increased ice losses from antarctica detected by cryosat-2. *Geophysical Research Letters*, 2014.

G. Moholdt, C. Nuth, J. O. Hagen, and J. Kohler. Recent elevation changes of svalbard glaciers derived from icesat laser altimetry. *Remote Sensing of Environment*, 114(11):2756–2767, 2010.

G. Moholdt, B. Wouters, and A. S. Gardner. Recent mass changes of glaciers in the russian high arctic. *Geophysical Research Letters*, 39(10), 2012.

H. Moritz. Least-squares collocation. *Reviews of geophysics*, 16(3):421–430, 1978.

S. Nghiem, D. Hall, T. Mote, M. Tedesco, M. Albert, K. Keegan, C. Shuman, N. DiGirolamo, and G. Neumann. The extreme melt across the greenland ice sheet in 2012. *Geophysical Research Letters*, 39(20), 2012.

J. Nilsson, L. Sandberg Sørensen, V. R. Barletta, and R. Forsberg. Mass change of arctic ice caps and glaciers: implications of regionalizing elevation changes. *The Cryosphere*, 9:1–12, 2015a. doi: 10.5194/tc-9-1-2015.

J. Nilsson, P. Vallelonga, S. Simonsen, L. Sørensen, R. Forsberg, D. Dahl-Jensen, M. Hirabayashi, K. Goto-Azuma, C. Hvidberg, H. Kjær, and

K. Satow. Greenland 2012 melt event effects on cryosat-2 radar altimetry. *Geophysical Research Letters*, 2015b. Submitted.

F. Papa, B. Legrésy, and F. Rémy. Use of the Topex-Poseidon dual-frequency radar altimeter over land surfaces. *Remote Sensing of Environment*, 87: 136–147, 2003. ISSN 00344257. doi: 10.1016/S0034-4257(03)00136-6.

R. K. Pearson. Outliers in process modeling and identification. *Control Systems Technology, IEEE Transactions on*, 10(1):55–63, 2002.

H. D. Pritchard, R. J. Arthern, D. G. Vaughan, and L. A. Edwards. Extensive dynamic thinning on the margins of the greenland and antarctic ice sheets. *Nature*, 461(7266):971–975, 2009.

G. Rees and W. G. Rees. *Physical principles of remote sensing*. Cambridge University Press, 2012.

F. Remy, C. Brossier, and J. F. Minster. Intensity of satellite radar-altimeter return power over continental ice: a potential measurement of katabatic wind intensity, 1990. ISSN 00221430. URL http://www.scopus.com/inward/record.url?eid=2-s2.0-0025655470&partnerID=tZOtx3y1.

F. Remy, B. Legresy, S. Bleuzen, P. Vincent, and J. Minster. Dual-frequency topex altimeter observations of greenland. *Journal of electromagnetic waves and applications*, 10(11):1507–1525, 1996.

J. K. Ridley and K. C. Partington. A model of satellite radar altimeter return from ice sheets. *International Journal of Remote Sensing*, 9(September 2014):601–624, 1988. ISSN 0143-1161. doi: 10.1080/01431168808954881.

E. Rignot and P. Kanagaratnam. Changes in the Velocity Structure of the Greenland Ice Sheet. *Science*, 311:986–990, 2006a. doi: 10.1126/science.1121381.

E. Rignot and P. Kanagaratnam. Changes in the velocity structure of the greenland ice sheet. *Science*, 311(5763):986–990, 2006b.

E. Rignot, G. Casassa, P. Gogineni, W. Krabill, A. u. Rivera, and R. Thomas. Accelerated ice discharge from the antarctic peninsula following the collapse of larsen b ice shelf. *Geophysical Research Letters*, 31(18), 2004.

A. Shepherd, E. R. Ivins, A. Geruo, V. R. Barletta, M. J. Bentley, S. Bettadpur, K. H. Briggs, D. H. Bromwich, R. Forsberg, N. Galin, et al. A reconciled estimate of ice-sheet mass balance. *Science*, 338(6111):1183–1189, 2012.

H. Skourup, S. Hvidegaard, R. Forsberg, I. Einarsson, A. Olesen, L. Sørensen, L. Stenseng, S. Hendricks, V. Helm, and M. Davidson. *CryoVEx 2011-12 Airborne Campaigns for CryoSat Validation*. ESA - SP. European Space Agency, ESA, 2013.

D. C. Slobbe, R. C. Lindenbergh, and P. Ditmar. Estimation of volume change rates of Greenland's ice sheet from ICESat data using overlapping footprints. *Remote Sensing of Environment*, 112(12):4204–4213, 2008. ISSN 00344257. doi: 10.1016/j.rse.2008.07.004. URL http://dx.doi.org/10.1016/j.rse.2008.07.004.

L. Sørensen, S. Simonsen, R. Meister, R. Forsberg, J. Levinsen, and F. T. Envisat-derived elevation changes of the greenland ice sheet, and a comparison with icesat results in the accumulation area. *Remote Sensing of Enviroment*, 2014. doi: 10.1016/j.rse.2014.12.022.

L. S. Sørensen, S. B. Simonsen, K. Nielsen, P. Lucas-Picher, G. Spada, G. Adalgeirsdottir, R. Forsberg, and C. Hvidberg. Mass balance of the greenland ice sheet (2003-2008) from icesat data-the impact of interpolation, sampling and firn density. *Cryosphere*, 5(1):173–186, 2011.

R. J. Sullivan. *Radar foundations for imaging and advanced concepts*. SciTech Pub., 2004.

R. Thomas, C. Davis, E. Frederick, W. Krabill, Y. Li, S. Manizade, and C. Martin. A comparison of greenland ice-sheet volume changes derived from altimetry measurements. *Journal of Glaciology*, 54(185):203–212, 2008.

R. Thomas, E. Frederick, W. Krabill, S. Manizade, and C. Martin. Recent changes on greenland outlet glaciers. *Journal of Glaciology*, 55(189):147–162, 2009.

D. Vaughan, J. Comiso, I. Allison, J. Carrasco, G. Kaser, R. Kwok, P. Mote, T. Murray, F. Paul, J. Ren, E. Rignot, O. Solomina, K. Steffen, and T. Zhang. Observations: Cryosphere. *Climate Change 2013: The Physical Sci- ence Basis. Contribution of Working Group I to the Fifth Assessment Report of the Intergovernmental Panel on Climate Change*, pages 317–382, 2013. doi: 10.1017/CBO9781107415324.012.

S. Vignudelli, A. G. Kostianoy, P. Cipollini, and J. Benveniste. *Coastal altimetry*. Springer, 2011.

D. Wingham, A. Ridout, R. Scharroo, R. Arthern, and C. Shum. Antarctic elevation change from 1992 to 1996. 456(1998):1996–1999, 1998. ISSN 1095-9203. doi: 10.1126/science.282.5388.456. URL http://discovery.ucl.ac.uk/113219/.

D. J. Wingham, C. R. Francis, S. Baker, C. Bouzinac, D. Brockley, R. Cullen, P. de Chateau-Thierry, S. W. Laxon, U. Mallow, C. Mavrocordatos, L. Phalippou, G. Ratier, L. Rey, F. Rostan, P. Viau, and D. W. Wallis. CryoSat: A mission to determine the fluctuations in Earth's land and marine ice fields. *Advances in Space Research*, 37:841–871, 2006. ISSN 02731177. doi: 10.1016/j.asr.2005.07.027.

H. Zwally, B. Schutz, W. Abdalati, J. Abshire, C. Bentley, A. Brenner, J. Bufton, J. Dezio, D. Hancock, D. Harding, et al. Icesat's laser measurements of polar ice, atmosphere, ocean, and land. *Journal of Geodynamics*, 34(3):405–445, 2002.

H. J. Zwally, R. a. Bindschadler, a. C. Brenner, T. V. Martin, and R. H. Thomas. Surface elevation contours of Greenland and Antarctic ice sheets. 88(2):1589–1596, 1983. ISSN 0148-0227. doi: 10.1029/JC088iC03p01589.

H. J. Zwally, R. A. Bindschadler, J. A. Major, and A. C. Brenner. Ice measurements by geosat radar altimetry. *Johns Hopkins APL Technical Digest*, 8:251–254, 1987.

H. J. Zwally, R. A. Bindschadler, A. C. Brenner, J. A. Major, and J. G. Marsh. Growth of greenland ice sheet: measurement. *Science (New York, N.Y.)*, 246(4937):1587–1589, 1989. ISSN 0036-8075. doi: 10.1126/science.246.4937.1587.

H. J. Zwally, A. C. Brenner, J. A. Major, T. V. Martin, and R. A. Bindschadler. Satellite radar altimetry over ice. volume 1: Processing and corrections of seasat data over greenland. Technical report, 1990.

H. J. Zwally, M. B. Giovinetto, J. Li, H. G. Cornejo, M. A. Beckley, A. C. Brenner, J. L. Saba, and D. Yi. Mass changes of the greenland and antarctic ice sheets and shelves and contributions to sea-level rise: 1992–2002. *Journal of Glaciology*, 51(175):509–527, 2005.

H. J. Zwally, L. Jun, A. C. Brenner, M. Beckley, H. G. Cornejo, J. Dimarzio, M. B. Giovinetto, T. A. Neumann, J. Robbins, J. L. Saba, et al. Greenland ice sheet mass balance: Distribution of increased mass loss with climate

warming; 2003–07 versus 1992–2002. *Journal of Glaciology*, 57(201):88–102, 2011.

A Scientific papers

This appendix contains the two supplementary articles that is a part of this thesis.

A.1 Mass changes in Arctic ice caps and glaciers: implications of regionalizing elevation changes

The Cryosphere, 9, 1–12, 2015
www.the-cryosphere.net/9/1/2015/
doi:10.5194/tc-9-1-2015

The Cryosphere Open Access

Mass changes in Arctic ice caps and glaciers: implications of regionalizing elevation changes

J. Nilsson, L. Sandberg Sørensen, V. R. Barletta, and R. Forsberg

Department of Geodynamics, DTU Space, Technical University of Denmark, Elektrovej 327, 2800 Lyngby, Denmark

Correspondence to: J. Nilsson (jnils@space.dtu.dk)

Received: 22 October 2013 – Published in The Cryosphere Discuss.: 11 December 2013
Revised: 27 November 2014 – Accepted: 2 December 2014 – Published:

Abstract. The mass balance of glaciers and ice caps is sensitive to changing climate conditions. The mass changes derived in this study are determined from elevation changes derived measured by the Ice, Cloud, and land Elevation Satellite (ICESat) for the time period 2003–2009. Four methods, based on interpolation and extrapolation, are used to regionalize these elevation changes to areas without satellite coverage. A constant density assumption is then applied to estimate the mass change by integrating over the entire glaciated region.

The main purpose of this study is to investigate the sensitivity of the regional mass balance of Arctic ice caps and glaciers to different regionalization schemes. The sensitivity analysis is based on studying the spread of mass changes and their associated errors, and the suitability of the different regionalization techniques is assessed through cross-validation.

The cross-validation results shows comparable accuracies for all regionalization methods, but the inferred mass change in individual regions, such as Svalbard and Iceland, can vary up to 4 Gt a^{-1}, which exceeds the estimated errors by roughly 50 % for these regions. This study further finds that this spread in mass balance is connected to the magnitude of the elevation change variability. This indicates that care should be taken when choosing a regionalization method, especially for areas which exhibit large variability in elevation change.

1 Introduction

The most recent assessments from the Intergovernmental Panel on Climate Change (Vaughan et al., 2014) and the Snow, Water, Ice and Permafrost in the Arctic Assessment (AMAP, 2012) state that the mass loss from glaciers and ice sheets is a major contributor to sea-level rise. The use of satellite altimetry to determine the elevation change in the major ice sheets has been possible since the late 1980s and was pioneered by Zwally et al. (1987), Wingham et al. (1998) and others. In recent years this has been expanded to ice caps and glaciers using both satellite and airborne altimetry, in studies such as Gardner et al. (2011), Moholdt et al. (2010a, 2012), Abdalati et al. (2004) and Arendt et al. (2002, 2006).

The geodetic mass balance of glaciers or ice caps can be determined through the use of altimetry by measuring the temporal change in surface elevation of the glaciated area. This rate of change is then converted into volume and finally mass change by multiplying the rate of change by area and an assumed density scheme. Determining the regional rate of change in the entire glaciated area involves interpolation or extrapolation (referred to hereinafter as regionalization) of the elevation changes to unmeasured areas away from the satellite ground tracks. This regionalization might introduce a large uncertainty to the volume estimate, as the track coverage over individual ice caps and glaciers are usually limited.

The focus of this study is to determine the impact of different regionalization schemes on regional ice-mass balance estimates of Iceland, Svalbard, the Russian High Arctic and the Canadian Arctic (south and north). Studying the spread of mass change and their estimated errors allows us to judge the different regions' sensitivity to the regionalization procedure. A cross-validation allows us to identify more preferable regionalization schemes.

Published by Copernicus Publications on behalf of the European Geosciences Union.

2 Study areas and data

In this study, we focus on five regions in the Arctic: Iceland (ICEL), Svalbard (SVLB), the Russian High Arctic (RUS), Canadian Arctic North (CAN) and Canadian Arctic South (CAS). The glacier outlines for these areas have been obtained from the "Randolph Glacier Inventory" (RGI) (Pfeffer et al., 2014).

The regional mass changes have been estimated from elevation changes obtained from the Ice, Cloud, and land Elevation Satellite (ICESat) (Schutz et al., 2005) over the time period 2003–2009. ICESat carried the Geoscience Laser Altimetry System (GLAS), which operated from 2003 to 2009 and had a repeat cycle of 96 days with a 33-day sub-cycle. The system measured the range between the satellite and a surface on the Earth, derived from the delay time between the transmitted laser pulse and the received return echo. The average ground-track sample spacing was 172 m along-track, and the ground footprint was approximately 70 m in diameter. The ICESat elevation data are obtained from the National Snow and Ice Data Center (http://nsidc.org/data/icesat/index.html) in the form of the GLA06 L1B global surface elevation data product, product release (R33).

Digital elevation models (DEMs) with a resolution of 1 km (30 arcsec) for use in the elevation-dependent regionalization are available for the five areas. The GTOPO30 DEM is used for the areas of CAS, CAN and RUS. For SVLB and ICEL, DEMs from the National Geospatial-Intelligence Agency (NGA) are used. The GTOPO30 model is estimated to have vertical accuracies of 50–200 m (http://www1.gsi.go.jp/geowww/globalmap-gsi/gtopo30/gtopo30.html). The NGA DEMs have a similar accuracy, as the data partly have common roots.

To further estimate the quality of the topography models, we have compared them to 2003–2009 surface heights obtained from ICESat by interpolating the DEM's CE1 surface heights to the ICESat data locations using bilinear interpolation. We estimate the standard deviation of the difference between the DEM heights and the ICESat heights to judge their quality. For the GTOPO30 model we find an average standard deviation over all regions of ~ 65 m and for the NGA DEMs of ~ 45 m.

3 Data processing

In an initial step, the ICESat GLA06 product has been filtered using the quality flags and rejection parameters included in the product release. Several rejection criteria have been used in the data culling, e.g. data are only used if the flags indicated usable elevations (i_ElvuseFlg = 1) and only have one peak in the return signal (i_numPk = 1). Relevant data (i_satCorrFlg = 2) have been corrected with the provided saturation correction. Each elevation measurement has been corrected for the Gaussian centroid (GC) offsets according to Borsa et al. (2013). There exists an inter-campaign bias in the ICESat data Siegfried et al. (2011) and Hofton et al. (2013), but since this is still debated, we have not applied any bias correction in this study. The RGI glacier outlines have been used to extract only data over the glaciated areas of interest.

The ICESat ground tracks did not have perfect spatial repetition, and there could be large (up to 1°) offsets between the individual tracks from the main ground-track cluster. Tracks with large offsets have been edited out in order to produce more robust elevation change estimates. The ICESat repeat ground tracks are divided into 500 m segments to estimate surface elevation changes. The mean elevation change was estimated in each segment by least-squares regression if data from more than six campaigns were available. This method is described in detail in Sørensen et al. (2011) (referred to in that paper as the M3 method).

A cleaning procedure has been applied to the estimated elevation changes, in which elevation changes with an estimated standard deviation (estimated from the least-squares solution) outside the 95 % confidence interval of the regression errors are removed. Furthermore, a 10-point moving Hampel filter (Pearson et al., 2002) has been used to identify and remove outliers in the elevation changes. The filtering is applied in the elevation change versus elevation domain to ease outlier detection. The success of the screening was judged visually to avoid unnecessary rejection. As a last step, an along-track smoothing filter has been applied to the elevation change data. An unweighted five-point moving average filter with a corresponding physical filter distance of 2.5 km has been used. Smoothing is undertaken to remove high-frequency noise from the elevation change estimates, and to aid the fitting procedure for the extrapolation and surface fitting for the interpolation methods, which are described in Sects. 4.2.1 and 4.2.2.

4 Methods

This study uses four different methods that have been implemented to regionalize elevation change to partly unmeasured glaciated areas. The four methods can broadly be divided into two categories: interpolation and extrapolation methods. The fundamental difference between the two approaches is what main correlation dependency they use for the regionalization procedure.

The interpolation methods use the spatial correlation (horizontal) of the elevation changes to predict an elevation change value at a specific geographical location. While the extrapolation method uses the usually high altitudinal correlation of elevation change to model the elevation change at a specific elevation. The four different methods (referred to as M1–M4), based on interpolation and extrapolation, can be summarized as follows:

- M1: smooth surface fit,
- M2: spatial model,
- M3: hypsometric polynomial,
- M4: hypsometric elevation bins.

The methods introduced here will be explained in the following sections.

One of the main sources of uncertainty in the mass change estimation is the conversion to mass via a density assumption (Huss et al., 2013). A constant density of 900 kg m^{-3} is used in this study. This assumption has also been applied by others, such as Gardner et al. (2011) and Moholdt et al. (2010a, 2012), and has been used in this study to simplify comparisons to other studies and to ensure that the spread in the mass balance estimates is a result of the different regionalization schemes alone and not due to the density conversion.

4.1 Regionalization: spatial interpolation

The first regionalization method (referred to as M1) fits a smooth surface to the scattered elevation change estimates, with an along-track resolution of 500 m, using least-squares collocation (as implemented in the GRAVSOFT program GEOGRID; see Forsberg et al., 2008, and Moritz., 1978) onto a regular grid, with a grid spacing of 0.01° latitude and 0.025° longitude, corresponding to a resolution of $\sim$1 km. The glaciated area of these grids have then been extracted using the RGI glacier outlines.

The least-squares collocation interpolation uses a quadrant-based nearest-neighbour search to find the N_q closest points in every quadrant around the prediction point. The data points are then interpolated by applying a second-order Markov covariance model. The covariance length is found from the data and the correlation distance is input by the user to the GEOGRID program. The correlation length has been increased until the individual satellite ground tracks are not visible on the surface. This method create a smooth continuous surface between the individual ground tracks, that usually have large cross-track spacing.

Due to data processing and data editing there is a loss of spatial coverage and thus data gaps in the along-track elevation changes. The second regionalization method (referred to as M2) tries to improve this by re-sampling the along-track data location in every track from 500 to 100 m. This to fill in data gaps and increases the along-track resolution. New along-track elevation changes are then estimated from the entire elevation change data set using the following model:

$$\dot{h} = a_0 + a_1\Phi + a_2\lambda + a_3 h + \ldots + a_N h^N, \quad (1)$$

where $\dot{h}$ is the parametrized elevation change value, a_i are the model coefficients, h is the DEM elevation, N is the model order, Φ is the latitude and λ is the longitude. The model order used for each region is the same as described in Sect. 4.1.2 for the spatial extrapolation methods. The M2 approach was chosen because it takes into account the overall spatial pattern of the elevation changes instead of just the nearest neighbours, which can in some cases be situated far away due to large across-track distances.

For the five regions of interest in this study, the number of points in each quadrant is set to $N_\mathrm{q} = 5$, and a correlation length of 50 km gave a sufficiently smooth surface.

4.2 Regionalization: hypsometric extrapolation

The third regionalization method (M3) uses hypsometric averaging (Nuth et al., 2010; Moholdt et al., 2010a) for extrapolation of elevation change estimates to derive volume change. Hypsometric averaging is based on parametrizing elevation changes as a function of elevation using an external DEM, with the corresponding grid spacing as M1–M2. The glaciated area is divided into elevation bands or bins, and each band is assigned a representative elevation change value, estimated from the parametrized data set.

In M3, the elevation changes are parametrized by fitting a polynomial function to all the elevation change data, as in Nuth et al. (2010) and Moholdt et al. (2010a). The elevations are obtained from the glacier-masked DEMs for every region (see Sect. 2). Hypsometric averaging is then used to extrapolate the elevation changes regionally.

To determine the degree and the number of terms in the polynomial, we need a measure of how much variance the model is able to account for. The more variability that can be incorporated into the model, the better it will explain the underlying statistics of the measured data. We use the adjusted R^2 statistics as a measure of incorporated variance (see Moholdt et al., 2010a). The degree of the polynomial and the number of parameters are then increased until a convergence of this R^2 is reached. For all regions except Svalbard, a linear fit ($D = 1$) was sufficient to parametrize the relation. For Svalbard, a third-order polynomial ($D = 3$) fits the distribution best (as measured by R^2, as used by Moholdt et al., 2010a). An elevation bin range of 50 m was chosen for all regions, consistent with Gardner et al. (2011).

The fourth regionalization method (M4) also involves binning the elevation changes according to elevation (as in M3), but instead of estimating the centre bin elevation change from a continuous function we instead use the mean value of the elevation changes inside the bin. Elevation bins that do not contain any data are assigned a value from linear interpolation. DEM elevations which are not covered by the ICESat data (usually low and high elevations) are assigned a value from extrapolation of the linear function to these bins, estimated from the entire data set.

The Russian High Arctic was divided into three subregions (Novaya Zemlya, Franz Josef Land and Severnaya Zemlya) for the analysis when using regionalization methods M3 and M4, due to large geographical separation within this region.

4.3 Volume and mass change

To determine the regional volume change in the interpolated and extrapolated fields the estimated elevation changes are multiplied by their corresponding area. This procedure differs between the inter and extrapolation methods and is for that reason described below.

To estimate the volume change from the interpolation methods (M1–M2) each individual elevation change grid cell (pixel), $\dot{h}_i$, is multiplied with its corresponding area, A_p TS1, and summed as follows to obtain the regional volume change $\dot{V}$:

$$\dot{V} = \sum (\dot{h}_i) \cdot A_\mathrm{p}. \quad (2)$$

The volume change from the extrapolated elevation changes (M3–M4) are estimated in a slightly different way. Here the estimated elevation change for each bin or band is multiplied with the total area of each band, and summed as follows to obtain the regional volume change:

$$\dot{V} = \sum \left(\dot{h}(z) \cdot A(z)\right), \quad (3)$$

where $\dot{h}$ is the specific elevation change value assigned to the elevation band/bin z, which is defined as the centre or mid-elevation of that bin (i.e. 25 m if the bin range is 0–50 m). $A(z)$ represents the total area inside the elevation band/bin at the specific binned elevation z.

The regional mass change is then estimated by multiplying the volume change by a constant density of $900\,\mathrm{kg\,m^{-3}}$. This approach assumes that the mass changes are due to effects such as ice melt and dynamic thinning while ignoring effects like changes in accumulation rate and firn densification. This is a very simplified view and is not always valid, which makes it a large source of uncertainty.

Cross-validation TS2

A cross-validation scheme has been employed to assess the quality of the regionalized elevation change fields from the four different methods. As the individual elevation changes are highly correlated along-track, we perform a cross-validation scheme on entire ICESat tracks of elevation changes. The individual ground tracks are assumed to be uncorrelated, and the cross-validation is performed in the following manner:

1. Remove one of the ground tracks from the original data set.
2. Use M1–M4 to regionalize the elevation changes from the reduced data set.
3. Find the estimated elevation change values from the different methods at the locations of the removed ground track.
4. Compute the difference between the estimated and original elevation changes.
5. Compute the root mean square (rms) of the residuals.
6. Repeat the procedure for all available ground tracks.

This procedure will produce one rms value for each ground track and N_rms for each method. The mean rms, $\overline{\mathrm{rms}}$, of all the ground tracks is then used to judge the quality of the different regionalization schemes.

5 Error analysis

We base the error analysis on two main concepts – the standard deviation around the mean and the standard error of the data – following the approaches of Nuth et al. (2010) and Moholdt et al. (2010a). Several studies have been dedicated to quantifying the individual point measurement errors for ICESat over ice-covered regions. Brenner et al. (2007) found that the ICESat measurement error over ice sheets varied as a function of surface slope, ranging from 0.14 m at 0.1° up to 0.5 m at 1.2°. Regions such as Svalbard have a large range in surface slope, varying between 0 and 29° at most, with a mean slope of 4.1°. Therefore, we assume a conservative error of $\varepsilon_\mathrm{icesat} = 0.17\,\mathrm{m\,a^{-1}}$, coming from a measurement error of 1 m (Nuth et al., 2010) and a measurement period of 6 years. This error does not account for the inter-campaign bias CE2 in the ICESat data, which does not affect the spread of the regional mass balance.

To estimate the error from the elevation change estimation procedure, we use the standard deviation estimated from the least-squares solution of the elevation changes as a measure of how trustworthy the individual elevation change measurements are (Sørensen et al., 2011). ICESat elevation changes are highly correlated along-track due to distance being short between the measurements, compared to variations in the topography. In this study, we have estimated the correlation length from the semi-variogram of the elevation changes, and use the correlation length to spatially bin the elevation changes. The correlation lengths for the five regions are found to be ∼ 15 km for SVLB, ∼ 10 km for ICEL, ∼ 20 km for CAN, ∼ 20 km for CAS and ∼ 10 km for RUS. For more detailed work on this topic, please see Rolstad et al (2009). The bins are then assumed to be uncorrelated, and the total number of non-empty bins is used to estimate the standard error, $\varepsilon_{\mathrm{d}h/\mathrm{d}t}$, for all four methods M1–M4:

$$\varepsilon_{\mathrm{d}h/\mathrm{d}t} = \frac{\sigma_{\mathrm{d}h/\mathrm{d}t}}{\sqrt{N}}, \quad (4)$$

where N is the number of uncorrelated bins and $\sigma_{\mathrm{d}h/\mathrm{d}t}$ is the mean standard deviation of the elevation changes. Here, $\sigma_{\mathrm{d}h/\mathrm{d}t}$ has already been reduced by a factor of $1/\sqrt{N_\mathrm{s}}$ due to the along-track smoothing, with N_s being the size of the smoothing filter.

The least-squares collocation error associated with M1 and M2 is estimated by computing the standard deviation of the data around every prediction point according to Moritz. (1978). The mean value of these standard deviations is used as the interpolation error, and the standard error is computed in the same way as in the elevation change procedure:

$$\varepsilon_{\text{int}} = \frac{\sigma_{\text{int}}}{\sqrt{N}}, \tag{5}$$

where σ_{int} is the mean standard deviation from the collocation prediction of the data inside the glaciated area.

We quantify the parametrization error from the fitting of the polynomial function used in M2 and M3 by calculating the root-mean-square error (RMSE) between the original elevation change estimates and the predicted values:

$$\varepsilon_{\text{fit}} = \frac{\sigma_{\text{fit}}}{\sqrt{N-D}}, \tag{6}$$

where σ_{fit} is the RMSE between the original and predicted data, and $\sqrt{N-D}$ is the adjustment due to the degree of the polynomial. The extrapolation error, ε_{ext}, relevant for method M3, is quantified by the same approach as used in Nuth et al. (2010), with the extrapolation error being the root-sum-square (RSS) difference of the fitted error minus the elevation change error:

$$\varepsilon_{\text{ext}} = \sqrt{\varepsilon_{\text{fit}}^2 - \varepsilon_{\text{d}h/\text{d}t}^2}. \tag{7}$$

The extrapolation error for the mean binning method is referred to as the binning error, ε_{b}, not to be confused with ε_{ext}. This error is associated with M4 and is defined as the standard deviation inside every elevation bin, σ_{b}. The standard error is then calculated by assuming that the individual bins are uncorrelated:

$$\varepsilon_{\text{b}} = \frac{\sigma_{\text{b}}}{\sqrt{N}}, \tag{8}$$

The corresponding elevation change error, ε_{h} TS3, is then estimated as the RSS of the individual error sources as given in Table 1. The volumetric error, ε_{vol}, can then be estimated by multiplying the height error by the region's area CE3

$$\varepsilon_{\text{vol}} = \varepsilon_{\text{h}} \cdot A \tag{9}$$

We also include an error term, ε_{ρ}, to account for the simple density assumption used that ignores the fact that density is actually a function of space and time. The approach follows that of, Moholdt et al. (2010b)

$$\varepsilon_{\rho} = \frac{1}{2}(\rho_{\text{ice}} - \rho_{\text{firn}}), \tag{10}$$

where ρ_{ice} and ρ_{firn} are the densities of ice and firn, respectively. This error is applied to the entire glaciated region.

Table 1. The number of error terms present in each method. These error are then combined into a height error using RSS.

Method	Error terms
M1	$\varepsilon_{\text{icesat}}$, ε_{int}, $\varepsilon_{\text{d}h/\text{d}t}$
M2	$\varepsilon_{\text{icesat}}$, ε_{int}, $\varepsilon_{\text{d}h/\text{d}t}$, ε_{fit}
M3	$\varepsilon_{\text{icesat}}$, ε_{ext}, $\varepsilon_{\text{d}h/\text{d}t}$
M4	$\varepsilon_{\text{icesat}}$, ε_{b}, $\varepsilon_{\text{d}h/\text{d}t}$

Finally, we can estimate the mass balance error, $\varepsilon_{\text{mass}}$, as follows:

$$\varepsilon_{\text{mass}} = \sqrt{(\varepsilon_{\text{vol}} \cdot \rho)^2 + (\dot{V} \cdot \varepsilon_{\rho})^2}, \tag{11}$$

where $\dot{V}$ is the estimated volume change.

6 Results

The along-track rates of elevation change have been derived for the five regions: ICEL, SVLB, CAS, CAN and RUS. The elevation change results are shown in Fig. 1. The regions exhibit different patterns of rates and variability in the elevation changes. To clarify these differences, a histogram of the elevation changes for the different regions is shown in Fig. 2, and the associated mean elevation change rate, standard deviation, and minimum and maximum values are presented in Table 2. ICEL shows the largest mean rate and variability in elevation change of all five regions, while RUS and CAN show the lowest variability. SVLB exhibits its own unique behaviour, with a more complex pattern of elevation change; compared to the other areas, except for ICEL CE4, SVLB shows the lowest mean rate of elevation change at $-0.04\,\text{m}\,\text{a}^{-1}$, but the largest variability. The variability in the elevation changes found in the Canadian Arctic and the RUS is a factor of 2 lower than in ICEL and SVLB. The rate of elevation change is apparently a function of latitude, with lower-latitude regions like ICEL and CAS showing the largest mean rate of elevation change. This pattern is not as easily detected in the variability in the elevation change, seen in Table 2, where CAN and ICEL both show approximately the same magnitude of elevation change but a large difference in variability (63 %). Common for all five areas, though, is the negatively skewed distribution of elevation changes seen in Fig. 2.

The Arctic regions show a consistent pattern of large peripheral thinning and small changes in the interior regions of the ice caps (see Figs. 1 and 3). The thinning is mostly located in the low-elevation areas of the ice caps and glaciers ($h < 500$–$800\,\text{m}$), and becomes less negative as the elevation increases. This pattern has also been observed in both studies of ice sheets (e.g. Pritchard et al., 2009) and glaciers (Gardner et al., 2013; Bolsh et al., 2013). The lower elevations in every region show large variability in elevation change, which are clustered

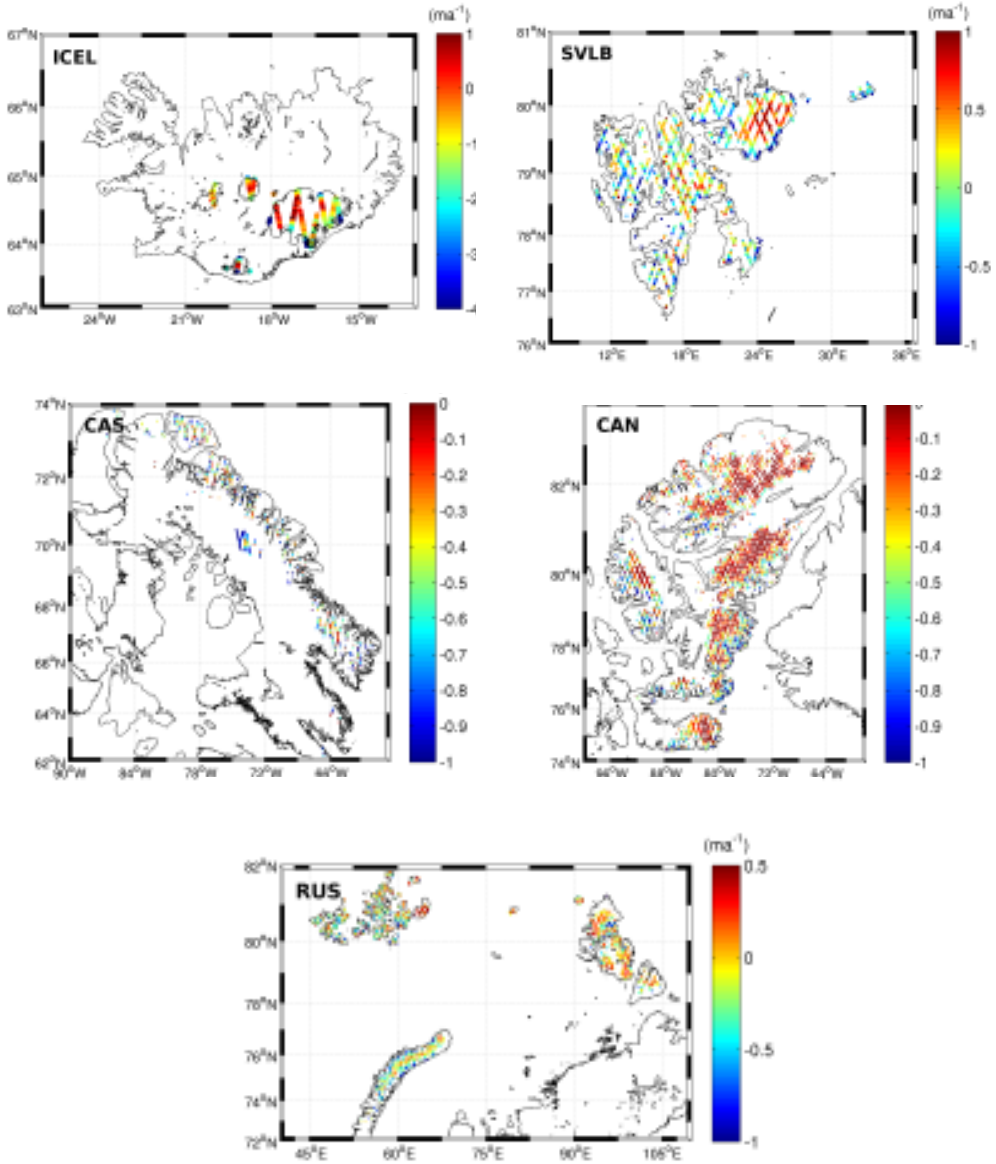

Figure 1. Spatial patterns of elevation changes of the five regions in the form of the satellite ground track coverage.

Table 2. ICESat point statistics of elevation change for the different Arctic regions. The values are in m a^{-1} for the statistics and km^2 for the area, and N is the number of observations.

Region	Mean	SD	Min	Max	Area	N
SVLB	−0.04	0.70	−6.70	2.20	33 673	4613
ICEL	−0.65	1.14	−6.20	1.79	10 989	851
CAN	−0.27	0.34	−3.00	1.44	103 990	18 022
CAS	−0.58	0.42	−3.75	1.88	40 601	3281
RUS	−0.13	0.34	−2.00	1.46	51 161	8797

around the coastal regions, in areas such as CAN and CAS.

Figure 3 shows the elevation change estimates plotted as a function of elevation, together with the estimated DEM hypsometry and the ICESat elevations averaged per 50 m elevation bin. Most regions in Fig. 3 show no evident or significant sampling bias when comparing the ICESat heights and the estimated DEM hypsometry. There are, however, some observed discrepancies in the ICESat sampling for the low elevations in both ICEL and RUS.

The mass changes estimated from all four methods and all five regions in this study are presented in Table 3, which also contains the estimated mass change error and the mean RMSE from the cross-validation procedure for each method. From Table 3 it can be seen that for regions such as CAN, CAS and RUS, only a small spread in their mass balance esti-

Table 3. Geodetic mass balance $\dot{m}$ from the four methods with their corresponding errors (σ), and their mean rms ($\overline{\text{rms}}$), maximum rms (rms_{max}) and minimum rms (rms_{min}) from the cross-validation procedure.

Region	Method	$\dot{m}$ [Gt a^{-1}]	σ [Gt a^{-1}]	$\overline{\text{rms}}$ [m a^{-1}]	rms_{max} [m a^{-1}]	rms_{min} [m a^{-1}]
Svalbard	M1	−3.3	2.5	0.57	3.45	0.17
	M2	−5.0	2.7	0.59	2.76	0.26
	M3	−2.5	1.6	0.59	4.10	0.18
	M4	−0.5	2.5	0.57	4.10	0.22
Iceland	M1	−7.8	1.9	1.21	4.62	0.18
	M2	−8.9	3.7	1.10	3.86	0.24
	M3	−10.9	2.7	1.03	3.25	0.40
	M4	−11.7	2.8	1.01	3.26	0.33
Canadian Arctic North	M1	−27.1	6.2	0.23	1.17	0.10
	M2	−25.4	5.8	0.27	1.18	0.12
	M3	−28.6	6.7	0.26	1.10	0.09
	M4	−28.6	7.9	0.25	1.03	0.10
Canadian Arctic South	M1	−22.0	5.7	0.39	2.46	0.15
	M2	−22.5	5.1	0.38	2.37	0.14
	M3	−22.9	5.3	0.37	2.52	0.11
	M4	−22.9	5.2	0.37	2.47	0.13
Russian High Arctic	M1	−7.1	2.0	0.25	0.79	0.04
	M2	−6.4	1.9	0.27	0.81	0.07
	M3	−7.7	3.1	0.28	0.88	0.10
	M4	−7.1	3.9	0.29	0.87	0.09

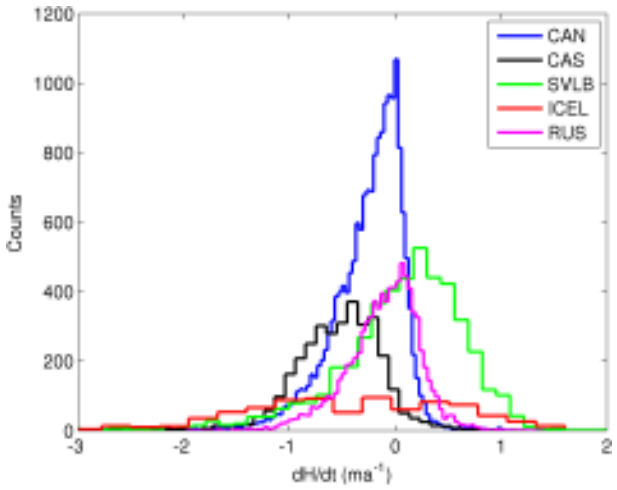

Figure 2. Histogram of elevation changes for the different Arctic regions. The Russian High Arctic (RUS) is treated as one region for visualization purposes.

mates is observed. For these three regions, the spread in mass balance estimates is well within the bounds of the estimated errors. For ICEL and SVLB, the spread of the estimated mass changes from the different methods is on the order of 50 % larger than the estimated mass change errors. The spread of the estimated mass changes for the different regions follows patterns seen in the elevation change variability (Table 2). Regions with high variability such as ICEL and SVLB show a much larger spread in the estimated mass changes than the areas with low elevation change variability.

The validity of the different regionalization schemes has been assessed though a cross-validation setup (Sect. 4.1.3). The results of the cross-validation are presented in Table 3, in the form of the mean, maximum and minimum rms for all four methods and regions. The mean RMSE follows the same pattern as detected in both the mass change estimates and elevation change variability, where areas associated with low elevation change variability and low spread in mass balance, such as CAN, CAS and RUS, show a much lower average rms (∼ 65 % lower) than ICEL and SVLB. ICEL shows on average the absolute highest RMSE and also the largest spread in rms between the different methods, as much as 20 %. For the other regions, the spread in the RMSE between the different methods show much better agreement, with observed differences of up to a few percent. The maximum and minimum values obtained from the cross-validation procedure show good agreement for most areas, such as CAN, CAS and RUS. For ICEL and SVLB, a larger spread is observed in these two parameters and follows in general the difference in mass balance, at least for SVLB.

Figure 4 shows the different spatial patterns obtained from the four regionalization procedures for ICEL. Here, the M3 and M4 methods show much larger negative elevation change values at lower elevations than the results based on M1 and

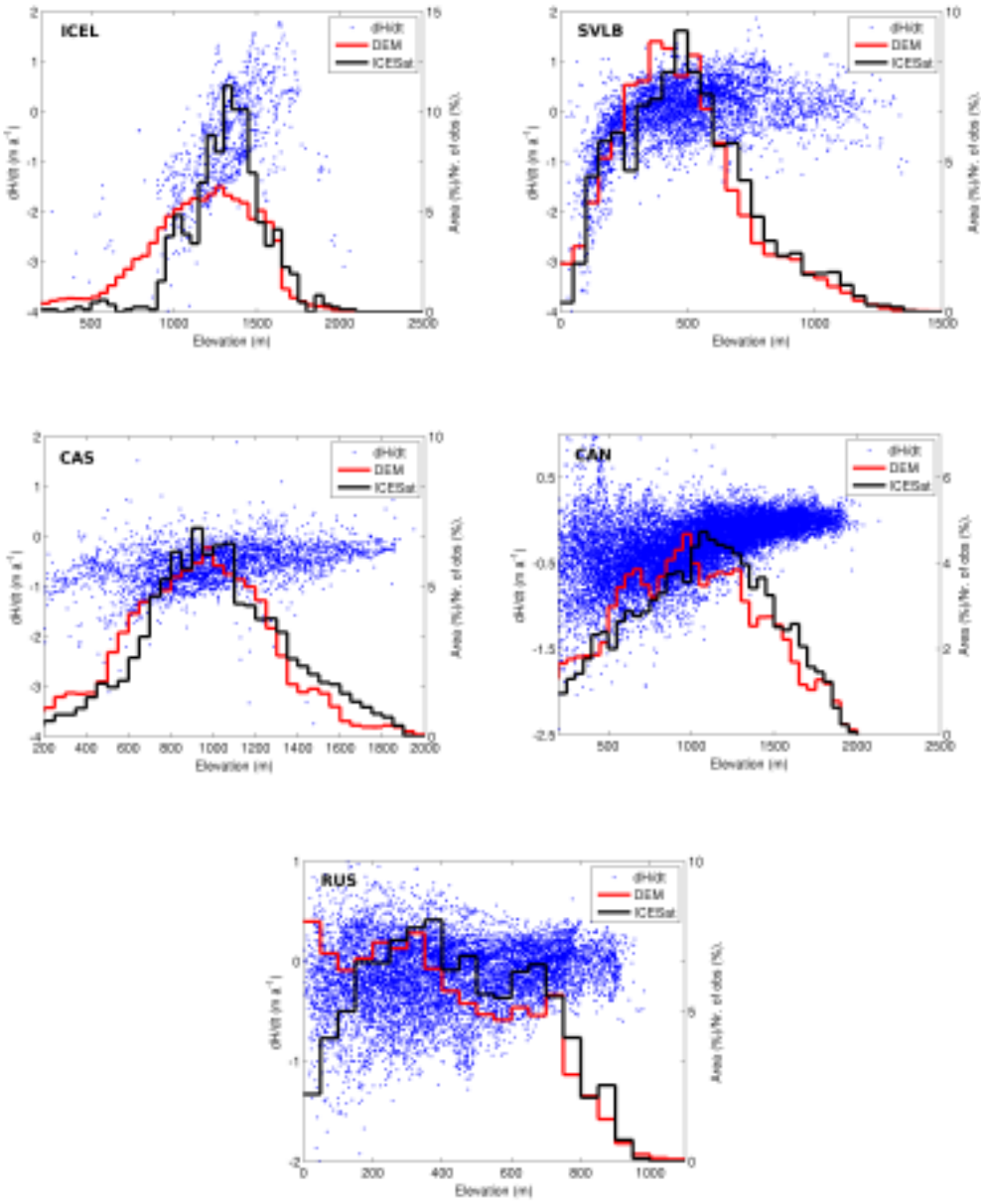

Figure 3. Elevation change (blue points) as a function of elevation for the different Arctic regions, which are used for the regional extrapolation. The black curve represents the density of ICESat's sampling and the red curve the DEM hypsometry, both per 50 m elevation bin.

M2. The more negative elevation change signal can also be detected in the estimated mass balance for M3 and M4, which is approximately 26 % more negative than for M1–M2.

7 Discussion

The large degree of variability seen in the lower elevations in Fig. 3 for most regions, especially RUS and CAN, indicates that complex spatial and temporal signals have been captured in the data (ice dynamics, ablation, snow accumulation, etc.). This variability is clustered into specific coastal areas in regions such as CAN and CAS, where most of the variability is located below $h < 500$–800 m, and in areas with drainage systems. Most of the more negative elevation changes ($\dot{h} < -1.5\,\mathrm{m\,a^{-1}}$), on the tail of the elevation change distribution, are also located in these low-elevation areas.

This type of low elevation variability (excluding sampling biases) might help to explain the observed difference between the interpolation and extrapolation methods, seen in Table 3. The extrapolation methods have proven to produce more negative values in these area ($h < 500$–800 m) than the

interpolation methods, because the interpolation and extrapolation regionalization schemes have two fundamental differences: (i) interpolation methods assume a spatial correlation of the elevation changes and (ii) extrapolation methods assume a vertical correlation in elevation of the elevation changes.

The interpolation approach would in theory (with satisfactory spatial coverage) capture the local spatial variability better than the extrapolation methods, as the extrapolation methods contain no spatial information. The extrapolation methods, on the other hand, make use of the usually high correlation to elevation (if the region is homogeneous enough) to produce a model that in principle is more representative of the lower elevations, given no sampling bias, because the interpolation methods might use data further away from the prediction point. These data might be located at higher elevations or may not be a good representation of the overall glacier-wide pattern, depending on how far away the data points are.

The main issue to consider for the interpolation methods is the spatial coverage of the data. If the spatial coverage is dense enough, the interpolation will be able to capture the spatial pattern of the region. The main issue to consider for the extrapolation methods is the size of the area used for the parametrization. If the area used for the parametrization is too large, important behaviour of the elevation change pattern might not be accounted for in the model. The differences between the interpolation and extrapolation methods can be reduced by dividing the extrapolation region into sub-regions before parametrization, or by including a spatial dependency in the parametrization model.

The effect of the amount of spatial coverage and homogeneity of a region can be exemplified by CAN and ICEL. CAN, for example, shows a very low spread in mass balance compared to its large size, while ICEL shows a much larger spread in mass balance. This is due to the spatial sampling of the CAN region being dense and the elevation change variability low, compared to ICEL. This has the effect that both the interpolation and extrapolation methods can capture both the spatial and altitudinal patterns of elevation change for CAN, in contrast to, for example CE5, ICEL with its low data density and large variability.

For most areas with a variability lower than $0.45\,\mathrm{m\,a^{-1}}$ (see Table 2), the impact of the regionalization schemes on the spread of the mass balance is small (on the order of a few percent), with a corresponding spread that falls within the mass balance error. However, for areas with much higher spatial variability and magnitude of elevation change, like ICEL and SVLB, the effect is much more prominent (Table 3). This is most certainly connected to the different types of climate regimes that the regions exhibit. Regions like CAN, CAS and RUS have a continental climate regime (dry and cold), while ICEL and SVLB are in a more maritime climate regime (wet and warm).

For ICEL, the observed difference of almost $4\,\mathrm{Gt\,a^{-1}}$ most probably arises from the low-elevation under-sampling, seen in Fig. 3, where the extrapolation methods are forced to produce more negative elevation changes. This is clearly seen in Fig. 4, where the lower elevations of Vatnajökull produced from the extrapolation methods are much more negative than their interpolation counterparts, and in the mass balance results, presented in Table 3. The estimated average mass balance for ICEL is $-9.8 \pm 2.8\,\mathrm{Gt^{-1}}$ CE6 (average of all methods) agrees well with the average contemporary mass loss of $-10 \pm 1.8\,\mathrm{Gt^{-1}}$ estimated by Björnsson et al. (2013) and Gardner et al. (2013) from glaciological measurements. However, there exists an average difference of roughly 25 % between the interpolation and extrapolation methods, where the average of the interpolation methods $-8.35\,\mathrm{Gt^{-1}}$ is more consistent with the results estimated by Gardner et al. (2013) of $-9 \pm 2\,\mathrm{Gt^{-1}}$, while the average of the extrapolation methods $-11.3\,\mathrm{Gt^{-1}}$ is more consistent with the results estimated by Björnsson et al. (2013) of $-11 \pm 1.5\,\mathrm{Gt^{-1}}$ CE7.

The difference between the M1–M2 and M3–M4 methods observed in SVLB (Table 3) are most probably due to large spatial variability in the region. The regional parametrization of SVLB might not fully capture the local elevation change pattern as well as the interpolation methods. This effect can be mitigated by applying a spatial dependency, or by dividing the area into sub-regions, as previously discussed. The division into sub-regions has previously been done by Moholdt et al. (2010a), using the M3 method and a $900\,\mathrm{kg\,m^{-3}}$ density, yielding a mass balance of $-3.7\,\mathrm{Gt\,a^{-1}}$. This is in good agreement with the estimated mass balance of $-4.15\,\mathrm{Gt\,a^{-1}}$ obtained from this study by averaging the M1–M2 methods.

The estimated mass changes for CAS and RUS are on the same order as previous studies. Gardner et al. (2011) found a estimated mass loss for CAS of $-24 \pm 6\,\mathrm{Gt\,a^{-1}}$, while Moholdt et al. (2012) found a mass loss of $-9.8 \pm 1.9\,\mathrm{Gt\,a^{-1}}$ for RUS. Both results are in good agreement with the results obtained from this study of CAS of $-22.6 \pm 5.3\,\mathrm{Gt\,a^{-1}}$ and RUS of $-7.1 \pm 2.7\,\mathrm{Gt\,a^{-1}}$ by averaging methods M1–M4. The estimated mass balance for CAN, however, shows a much larger difference of roughly $10\,\mathrm{Gt\,a^{-1}}$ compared to Gardner et al. (2011), who also used ICESat. This difference can mostly be explained by the fact that there was no inter-campaign bias included in the elevation change estimation procedure. The exclusion of the inter-campaign bias gave an average mass balance for CAN of roughly $-30\,\mathrm{Gt\,a^{-1}}$. This was further reduced down to $-27.4\,\mathrm{Gt\,a^{-1}}$ when the GC offset correction (Borsa et al., 2013) was applied. As the GC offset scales with area, smaller regions are less affected by the offset, while larger regions will show a much larger difference. This is also what is observed in this study when applying the GC offset correction. The size of the mass correction introduced by the trend in the GC offset can be estimated for CAN to roughly $1.9\,\mathrm{Gt\,a^{-1}}$ by assuming a maximum trend value of $2\,\mathrm{cm\,a^{-1}}$ and the area given in Table 2. This value agrees well with the observed value of roughly $2.6\,\mathrm{Gt\,a^{-1}}$,

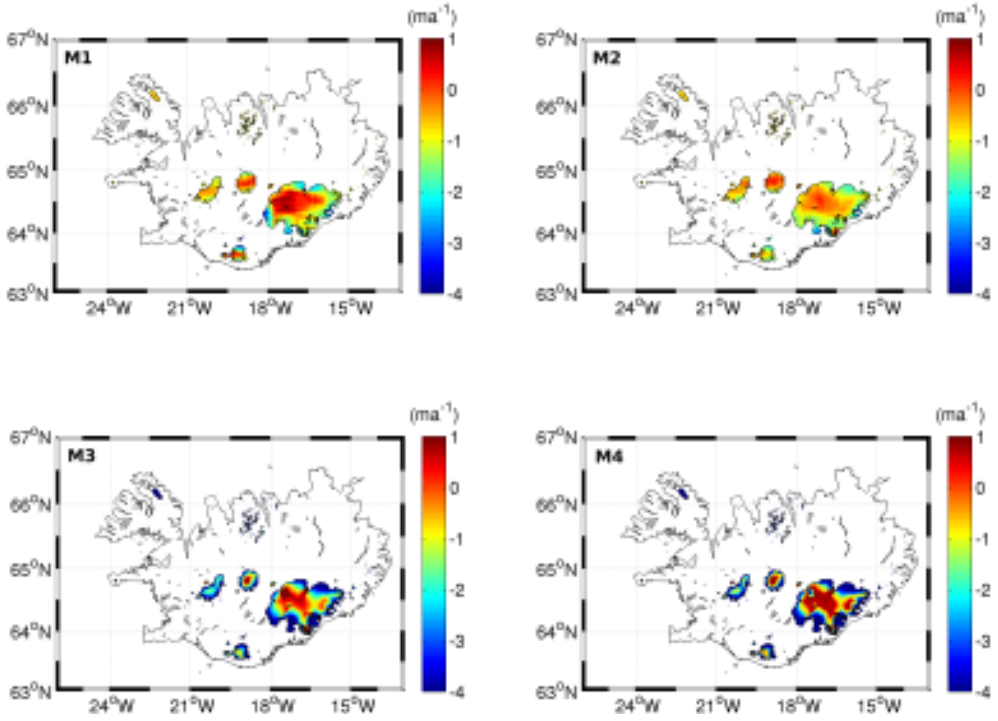

Figure 4. Regionalized elevation changes over Iceland from the M1–M4 methods showing the difference in estimated spatial patterns.

which makes the GC offset an important correction for large-scale mass balance studies using ICESat.

To determine whether the 1 km resolution is good enough to give realistic hypsometries, we made a comparison with the ASTER GDEM (http://gdem.ersdac.jspacesystems.or.jp) over Iceland. The ASTER GDEM was re-sampled at a 150 m resolution, to make it easier to handle; binned in 50 m elevation bands; and plotted against the NGA DEM for Iceland over the glaciated areas. Iceland was chosen because the largest discrepancies between the regionalization methods were found here, and also because it exhibits the largest rate of and variability in elevation change. Even though there exists an apparent sampling bias, the calculated mass changes using the ASTER GDEM (methods M3–M4) gave only a total difference of 2 %. Thus we believe that the 1 km DEMs are of sufficient quality and resolution to give realistic hypsometries.

The results of the cross-validation procedure, seen in Table 3, indicate that, given enough data sampling, the interpolation and extrapolation methods produce regionalized elevation change estimates of the same quality. Therefore, the interpolation methods described in this study can be used for future mass balance studies in these and other areas even with relatively sparse data sampling. This finding is in contrast to previous discussion, such as that of in Moholdt et al. (2010a), which states that the spatial sampling would usually be to sparse to allow for spatial interpolation, which is definitely true on a sub-regional basis.

Table 4. The final regional and total geodetic mass balance $\dot{m}$ estimated using the results from the cross-validation procedure and in situ comparison for Iceland, with corresponding error estimates (σ).

Region	$\dot{m}$ [Gt a^{-1}]	σ [Gt a^{-1}]	Methods
SVLB	−4.2	2.6	M1, M2
ICEL	−9.8	2.8	M1–M4
CAN	−27.4	6.7	M1–M4
CAS	−22.6	5.3	M1–M4
RUS	−7.1	2.7	M1–M4
Total	−71.1	9.7	

Using the estimated RMSEs from the cross-validation procedure, seen in Table 3, as a guide, a combined or final geodetic mass balance was computed, which can be seen in Table 4. The final mass balance and corresponding mass error for CAN, CAS and RUS were determined using the average value of all four methods. Both the RMSE and the estimated mass balance error showed good individual agreement with each other. The final mass balance for SVLB was computed from the M1–M2 method, as these two methods showed the smallest range in the RMSE even though all four methods on average showed the same mean RMSE. Determining the final geodetic mass balance for ICEL is somewhat more arbitrary, as the low density of data points makes the cross-validation more difficult. However, here the average of all methods was chosen to determine the final mass balance of

ICEL, as the average of M1–M4 shows the closest agreement with the average in situ-derived value of mass balance from Björnsson et al. (2013) and Gardner et al. (2013).

8 Conclusions

In this study, we have determined the impact of different regionalization schemes of elevation changes on the estimated mass balance of five different Arctic regions. These five regions consisted of the Canadian Arctic (north and south), the Russian High Arctic, Svalbard and Iceland. The estimated mass balance was then, in combination with a cross-validation procedure, used to determine how sensitive these regions are to different regionalization schemes of elevation change. Finally, we also estimated a mass balance budget for each region, using the results derived from the cross-validation procedure and the estimated mass errors.

The study found that the mean rates of and variability in elevation change varied extensively over the different areas in the Arctic. The rate of elevation changes showed a range of $0.6\,\mathrm{m\,a^{-1}}$ across the different regions, while the variability showed a corresponding range of $0.8\,\mathrm{m\,a^{-1}}$. Regions with large variability in elevation change showed a large spread in the estimated mass changes from the different methods, given the described setup. This spread was on average 50 % larger than the respective errors. For regions exhibiting low variability, the opposite was observed. Here, the spread of the mass changes lay well inside the estimated errors.

The statistics from the cross-validation procedure, in conjunction with the estimated mass balance results, indicate that the choice of regionalization method for regions with a variability of less than $0.5\,\mathrm{m\,a^{-1}}$ is negligible. However, if the variability exceeds $0.5\,\mathrm{m\,a^{-1}}$, caution and further analysis is required before choosing a method for mass balance studies. The results from the cross-validation further indicate that the interpolation and extrapolation methods are of the same quality for most areas. Hence the interpolation methods described in this study can also be used for mass balance studies of ice caps and glaciers with satisfactory results.

Acknowledgements. The authors would like to thank the different data contributors: the National Snow and Ice Data Center (NSIDC) for providing the ICESat data; the National Spatial-Intelligence Agency (NGA) for the Svalbard and Iceland DEM; the Ministry of Economy, Trade, and Industry (METI) of Japan and the United States National Aeronautics and Space Administration (NASA) for the ASTER GDEM; and the United States Geological Survey (USGS) for the GTOPO30 DEM. This publication is contribution no. 30 of the Nordic Centre of Excellence SVALI project "Stability and Variations of Arctic Land Ice", funded by the Nordic Top-level Research. We would like to thank the reviewers, especially Geir Moholdt, for their constructive comments and insights, which greatly improved this manuscript. This work was supported by funding from the ice2sea programme from the European Union 7th Framework Programme, grant number 226375. Ice2sea contribution number 175.

Edited by: E. Hanna

References

Abdalati, W., Krabill, W., Fredrick, E., Manizade, S., Martin, C., Sonntag, J., Swift, R., Thomas, R., Yungel, J., and Koerner, R.: Elevation changes of ice caps in the Canadian Arctic Archipelago, J. Geophys. Res., 109, F04007, doi:10.1029/2003JF000045, 2004.

AMAP: Arctic Climate Issues 2011: Changes in Arctic Snow, Water, Ice and Permafrost, SWIPA 2011 Overview Report,TS4, 2012.

Arendt, A., Echelmeyer, K., Harrison, W., Lingle, C., and Valentine, V.: Rapid Wastage of Alaska Glaciers and Their Contribution to Rising Sea Level, Science, 297, 382TS5, doi:10.1126/science.1072497, 2002.

Arendt, A. A., Echelmeyer, K., Harrison, W., Lingle, C., Zirnheld, S., Valentine, V., Ritchie, B., and Druckenmiller, M.: Updated estimates of glacier volume changes in the western Chugach Mountains, Alaska, and a comparison of regional extrapolation methods, J. Geophys. Res.-Earth Surf., 111, F03019, doi:10.1029/2005JF000436, 2006.

Bamber, J., Krabill, W., Raper, V., and Dowdeswell, J.: Anomalous recent growth of part of a large Arctic ice cap: Austfonna, Svalbard, Geophys. Res. Lett., 31, L12402, doi:10.1029/2004GL019667, 2004.

Björnsson, H., Pálsson, F., Gudmundsson, S., Magnússon, E., Adalgeirsdóóttir, G., Jóóhannesson, T., Berthier, E., Sigurdsson, O., and Thorsteinsson, T.: Contribution of Icelandic ice caps to sea level rise: Trends and variability since the Little Ice Age, Geophys. Res., 40, 1–5, doi:10.1002/grl.50278, 2013.

Bolch, T., Sandberg Sörensen, L., Simonsen, S. B., Mölg, N., Machguth, H., Rastner, P., and Paul, F.: Mass loss of Greenland's glaciers and ice caps 2003–2008 revealed from ICESat laser altimetry data, Geophys. Res. Lett., 40, 875–881, doi:10.1002/grl.50270, 2013.

Borsa, A. A., Moholdt, G., Fricker, H. A., and Brunt, K. M.: A range correction for ICESat and its potential impact on ice-sheet mass balance studies, The Cryosphere, 8, 345–357, doi:10.5194/tc-8-345-2014, 2014.

Brenner, A., DiMarzio, J. P., and Zwally, H. J.: Precision and Accuracy of Satellite Radar and Laser Altimeter Data Over the Continental Ice Sheets, IEEE Trans. Geosci. Remote Sens., 45, 321–331, doi:10.1109/TGRS.2006.887172, 2007.

Forsberg, R. and Tscherning, C. C.: An overview manual for the GRAVSOFT Geodetic Gravity Field Modelling Programs, available at: http://www.gfy.ku.dk/~cct/publ_cct/cct1936.pdf (TS6), 2008.

Gardner, A., Moholdt, G., Wouters, B., Wolken, G., Burgess, D., Sharp, M., Cogley, G., Braun, C., and Labine, C.: Sharply increased mass loss from glaciers and ice caps in the Canadian Arctic Archipelago, Nature, 357, 473TS7, doi:10.1038/nature10089, 2011.

Gardner, A., Moholdt, G., Cogley, J. G., Wouters, B., Arendt, A., Wahr, J., Berthier, E., Hock, R., Pfeffer, W. T., Kaser G., Ligtenberg, S. R. M., Bolch, T., Martin, J., Sharp, M. J., Hagen, J. O.,

van den Broeke, M. R., and Paul, F.: A Reconciled Estimate of Glacier Contributions to Sea Level Rise: 2003 to 2009, Science, 340, 852–857, doi:10.1126/science.1234532, 2013.

Hofton, M. A., Luthcke, S. B., and Blair, J. B.: Estimation of ICESat intercampaign elevation biases from comparison of lidar data in East Antarctica, Geophys. Res. Lett., 40, TS8, doi:10.1002/2013GL057652, 2013.

Huss, M.: Density assumptions for converting geodetic glacier volume change to mass change, The Cryosphere, 7, 877–887, doi:10.5194/tc-7-877-2013, 2013.

Jacob, T., Wahr, J., Pfeffer, W. T., and Swenson, S.: Recent contributions of glaciers and ice caps to sea level rise, LETTER, Nature, 483, TS9, doi:10.1038/nature10847, 2012.

Kaser, G., Cogley, J., Dyurgerov, M. B., Meier, M. F., and Ohmura, A.: Mass balance of glaciers and ice caps: Consensus estimates for 1961–2004, Geophys. Res. Lett., 33, L19501, doi:10.1029/2006GL027511, 2006.

Krabill, W., Abdalati, W., Fredrick E., Manizade, S., Martin, C., Sonntag, J., Swift, R., Thomas, R., Wright, W., and Yungel, J.: Greenland ice sheet: High elevation balance and peripheral thinning, Science, 289, TS10, 2000.

Moholdt, G., Nuth, C., Hagen, J. O., Kohler, J.: Recent elevation changes of Svalbard glaciers derived from ICESat laser altimetry, Remote Sens. Environ., 114, 2756–2767, 2010a.

Moholdt, G., Hagen, J. O., Eiken, T., and Schuler, T. V.: Geometric changes and mass balance of the Austfonna ice cap, Svalbard, The Cryosphere, 4, 21–34, doi:10.5194/tc-4-21-2010, 2010.

Moholdt, G., Wouters, B., and Gardner, A.: Recent mass change of glaciers in the Russian High Arctic, Geophys. Res., 39, L10502, doi:10.1029/2012GL051466, 2012.

Moritz, H.: Least Squares Collocation, Reviews of Geophysics and Space Physics, 16, 421–430, doi:10.1029/RG016i003p00421, 1978.

Nuth, C., Moholdt, G., Kohler, J., Hagen, J. O., and Kääb, A.: Svalbard glacier elevation changes and contribution to sea level rise, J. Geophys. Res., 115, F01008, doi:10.1029/2008JF001223, 2010.

Pearson, K. R.: Outliers in process modeling and identification, IEEE, Transa. Control Syst. Technol., 10, TS11, 2002.

Pfeffer, T.W., Arendt, A. A., Bliss, A., Bolch, T., Cogley, J. G., Gardner, A. S., Hagen, J. O., Hock, R., Kaser, G., Kienholz, C., Miles, E. S., Moholdt, G., Mölg, N., Paul, F., Radić, V., Rastner, P., Raup, B. H., Rich, J., Sharp, M. J.: The Randolph Consortium, J. Glaciol., 60, 221TS12, 2014.

Pritchard, H. D., Arthern, R. J., Vaughan, D. G., and Edwards, L. A.: Extensive dynamics thinning on the margins of the Greenland and Antartic ice sheets, Nature, 461, TS13, doi:10.1038/nature08471, 2009.

Rolstad, C., Haug, T., and Denby, B.: Spatially-integrated geodetic glacier mass balance and its uncertainty based on geostatistical analysis: application to the Western Svartisen ice cap, Norway, J. Glaciol., 55, 666–680, 2009.

Schutz, B. E., Zwally, H. J., Shuman, C. A., Hancock, D., and DiMarzio, J. P.: Overview of the ICESat Mission, Geophys. Res. Lett., 32, L21S01, doi:10.1029/2005GL024009, 2005.

Siegfried, M. R., Hawley, R. L., and Burkhart, J. F.: High-resolution ground-based GPS measurements show intercampaign bias in ICESat elevation data near summit, Greenland, IEEE, Geosci. Remote Sens., 49, TS14, 2011.

Sørensen, L. S., Simonsen, S. B., Nielsen, K., Lucas-Picher, P., Spada, G., Adalgeirsdottir, G., Forsberg, R., and Hvidberg, C. S.: Mass balance of the Greenland ice sheet (2003–2008) from ICESat data – the impact of interpolation, sampling and firn density, The Cryosphere, 5, 173–186, doi:10.5194/tc-5-173-2011, 2011.

Vaughan, D. G., Comiso, J. C., Allison, I., Carrasco, J., Kaser, G., Kwok, R., Mote, P., Murray, T., Paul, F., Ren, J., Rignot, E., Solomina, O., Steffen, K., and Zhang, T.: Observations: Cryosphere, in: Climate Change 2013: The Physical Science Basis. Contribution of Working Group I to the Fifth Assessment Report of the Intergovernmental Panel on Climate Change, edited by: Stocker, T. F., Qin, D., Plattner, G.-K., Tignor, M., Allen, S. K., Boschung, J., Nauels, A., Xia, Y., Bex, V., and Midgley, P. M., Cambridge University Press, Cambridge, UK and New York, NY, USA, 2013.

Wingham, D., Ridout, A., Scharroo, R., Arthern, R., and Shum, C. K.: Antartic elevation change from 1992–1996, Science, 282, TS15, 1998.

Zwally, H. J., Bindschadler, R. A., Major, J. A., and Brenner, A. C.: Ice measurements by Geosat radar altimetry, Johns Hopkins APL Technical Digest (ISSN 0270-5214), Vol. 8, April–June, 251–254, 1987.

Remarks from the language copy-editor

CE1 Is this referring to a singular DEM or DEMs (DEMs')?
CE2 Please check whether the correct noun; this seems incomplete.
CE3 Please check; "regional area" seems strange as phrasing.
CE4 Please check whether this reflects what is meant; previous placement was confusing.
CE5 Please check whether correct ("for example" (e.g.) seems more likely here than "that is" (i.e.)).
CE6 Should these following instances be Gt a^{-1}, or is this simply "per gigatonne"?
CE7 Please check; these "where" and "where" clauses do not make sense by themselves (only as part of a full sentence).
CE8 Please check; as above, such a part of a sentence cannot stand alone.

Remarks from the typesetter

TS1 What does subscript "p" stand for?
TS2 This enumeration had to be deleted because at least two sub-subsections would be required.
TS3 What does subscript "h" stand for?
TS4 Please give editors.
TS5 Please give full page range
TS6 Please give last access date.
TS7 Please give full page range.
TS8 Please give article number or page range.
TS9 Please give page range or article number.
TS10 Please give page range or article number and doi.
TS11 Please give page range or article number and doi.
TS12 Please give page range or article number and correct doi.
TS13 Please give article number or page range.
TS14 Please give page range or article number and doi.
TS15 Please give page range or article number and doi.

A.2 Greenland 2012 melt event effects on CryoSat-2 radar altimetry

Greenland 2012 melt event effects on CryoSat-2 radar altimetry

Johan Nilsson[1], Paul Vallelonga[2], Sebastian B. Simonsen[1], Louise Sandberg Sørensen[1], René Forsberg[1], Dorthe Dahl-Jensen[2], Motohiro Hirabayashi[3], Kumiko Goto-Azuma[3], Christine S. Hvidberg[2], Helle A. Kjær[2], and Kazuhide Satow[4]

Corresponding author: Johan Nilsson, DTU Space: (jnils@space.dtu.dk)

[1]DTU Space, National Space Institute

Technical Univeristy of Denmark, Lyngby,

Denmark

[2]Centre for Ice and Climate, Niels Bohr

Institute, University of Copenhagen, Juliane

Maries Vej 30, Copenhagen, Denmark

[3]National Institute of Polar Research,

10-3 Midori-cho, Tachikawa Tokyo,

190-8518, Japan

[4]Nagaoka National College of Technology,

888 Nishikatakai, Nagaoka, Niigata

940-8532, Japan

We use CryoSat-2 data to study elevation changes over an area in the interior part of the Greenland Ice Sheet during the extreme melt event in 2012. The penetration of the radar signal into dry snow depends heavily on the snow stratigraphy, and the rapid formation of refrozen ice layers can bias the surface elevations obtained from radar altimetry. We investigate the change in CryoSat-2 waveforms and elevation estimates over the melt event, and interpret the findings by comparing to in-situ surface and snow-pit observations from the North Greenland Eemian Ice Drilling Project camp. The investigation shows a major transition of scattering properties around the area, and an apparent elevation increase of 56 $\pm$ 26 cm is observed in the CryoSat-2 data. We conclude that this jump in elevation can be explained by the formation of a refrozen melt layer which raised the reflective surface, seen by CryoSat-2, and introduced a positive elevation bias across the region.

1. Introduction

The ESA CryoSat-2 satellite, launched in late 2010, carries a new type of radar altimeter especially designed for monitoring the changes of sea and land ice. The radar altimeter emits an electromagnetic pulse which is reflected by the Earth's surface and from the received power (dubbed the waveform), seen by the satellite, the surface height can be determined using a technique refereed to as retracking. The shape of the radar waveform, as a function of delay time, contains important information about the characteristics of the measured surface, which makes it possible to identify sudden and abrupt changes of the surface conditions of the ice sheet, such as i.e snow melt or heavy snowfall.

In the interior dry parts of the Greenland ice sheet snow is slowly transformed into ice within the top 50-100 meters of the ice sheet, commonly referred to as the firn column. The dielectric properties of this transformational stage vary, and differ from those of solid ice [*Huining et al.*, 1999; *Scott et al.*, 2006]. The difference in dielectric properties of snow, compared to ice, has the effect that signals at radar frequencies (Ku-band $\sim$13.6 GHz) will penetrate into the upper parts of the strata. This has the implication that the return signal does not necessarily originate from the snow-air interface, e.g. the physical surface, but instead from scatters within the upper parts of the snow layer [*Mätzler and Wegmüller*, 1987].

Repeated radar altimetry measurements of ice sheet surface topography have been widely used to monitor recent changes [*Khvorostovsky*, 2012; *Zwally et al.*, 2011; *Li and Davis*, 2008; *Johannessen et al.*, 2005]. There are challenges associated with using radar data to estimate the volume change of the Greenland ice sheet (GrIS) because of the

signal penetration into the snow, particularly the temporal and spatial changes of the penetration depth.

In July 2012, the GrIS experienced the most extensive melt event observed in recent time, during which 98.6% of the surface experienced melt on the 12th [*Nghiem et al.*, 2012]. Above average surface temperatures were observed across the ice sheet during a period of less than two weeks, after which the temperature returned to normal conditions *Hall et al.* [2013].

We expect that the 2012 melt event had a significant impact on derived CryoSat-2 data over the interior part of the GrIS, as proposed by *Forsberg et al.* [2013]. We hypothesize that the event led to an abrupt change in surface scattering properties in the dry snow zones due to the sudden formation of ice-layers near to the snow surface. The change in scattering properties seen from the Ku-frequency band would affect the inferred surface elevation of the ice-sheet and possibly introduce a regional elevation bias which could be misinterpreted as an actual elevation change of the GrIS, as also theorized by [*Scott et al.*, 2006]. To investigate the melt events effect on surface height retrieval from radar altimetry we analyse the CryoSat-2 level-2b intermediate (L2i) data product, provided by the European Space Agency (ESA), to determine whether an elevation bias was introduced into the product due to the 2012 melt event. Additionally, a detailed study of CryoSat-2 LRM level-1b (L1b) data, where additional information about the shape of the waveform was extracted than available in the L2i product, is undertaken around the area of the North Greenland Eemian Ice Drilling Project (NEEM) (located at 77.45°N and 51.06°W,

in north west Greenland), where in-situ data is available and used to validate and interpret the results derived from the processed CryoSat-2 L1b observations.

2. Data and methods

CryoSat-2 operates both in the low-resolution mode (LRM) and the interferometric synthetic aperture mode (SARin) over the GrIS. Here several types of CryoSat-2 data sets was used to study measurable effects on surface elevation changes at different spatial scales. Initially CryoSat-2 L2i data [*ACS Team and MSSL Team*, 2011] was used to assess ice sheet-wide elevation changes. A detailed description of the use of the CryoSat-2 L2i data are given in the supplementary material, however in essence the CryoSat-2 L2i data provides the user with the position and the elevation of the radar return. The CryoSat-2 L2i data contain little information about the scattering properties of the surface, which can be estimated from the radar waveforms parameters.

To date, the L2/L2i product only contains the backscatter and peakiness parameters, that can be used for the purpose of monitoring of the changes in the scattering properties of the surface. Hence, to obtain a more detailed study of the effects of abnormal weather conditions on surface height estimation, we additionally processed and analysed CryoSat-2 L1b data at different spatial scales (locally $\sim$25 km and regionally $\sim$300 km) around the NEEM-camp. In this process we estimated surface height and additional waveform parameters. In addition to the backscatter and the peakiness, the leading edge width and trailing edge slope was estimated from the waveforms. As mentioned previously these parameters can be used as proxies for monitoring changes in scattering properties of the measured surface [*Legresy and Rêmy*, 1997].

The backscatter (Bs) is controlled by the surface and volume echo and can be used to discriminate between different surface types [*Legresy and Rêmy*, 1997], where i.e. high backscatter would reveal a very smooth surface. The width of the leading edge waveform (LeW) is related to the micro-roughness of the small scale topography and surface penetration effects of the radar signal [*Legresy and Rêmy*, 1997]. A large leading edge width would be indicative of volume scattering of the signal in the upper parts of the firn, while a small leading edge would correspond to surface scattering. The trailing edge slope (TeS) of the waveform is mainly controlled by the ratio between volume and surface scattering, where a very high slope would reveal a very specular surface [*Legresy and Rêmy*, 1997]. The peakiness (PP) of the waveform is a statistical measure of how specular the waveform is and can be used to discriminate between different surface types [*Laxon*, 1994]. The derivation and definition of these parameters can as well be found in the supplementary material.

The procedure of processing the CryoSat-2 L1b data to produce accurate surface elevation estimates, is usually referred to as "retracking" and is necessary as the rise of the leading edge of the return signal is not located in the center of the range-gate window [*Davis*, 1997]. In this study the LRM L1b data was retracked using a 20% threshold retracker constructed to track the first peak of the waveform. The choice of retracking point is based on the requirements of robust and repeatable elevations [*Davis*, 1997]. For a regional analysis, data was collected for the months of June and August 2012 within a $3^\circ \times 3^\circ$ box centered around the NEEM site. Data below 2000 m elevation was excluded, to ensure predominant dry snow conditions prior to the melt event. For a local analysis,

CryoSat-2 20 Hz data within a radius of 0.2° around the NEEM site was collected, between the period of January 2011 to December 2013. The local and regional data where then compared to in-situ observations, obtained from the NEEM site, in the form of surface observations, weather data and snow-pit samples taken before, during and after the event. The regional analysis was performed to derive more robust statistics, as the spatial data coverage is usually quite sparse on local scales (∼20 km) and at monthly time intervals.

3. Results

Fig. 1 shows the difference in surface elevation between the months of May-June and August-September 2012 from the L2i dataset. The figure shows a clear positive surface increase in the dry snow zone and ablation in the coastal regions over the period of May-June and August-September 2012. The magnitude of the positive surface elevation increase in the dry snow (above 2000 m and north of 70° latitude) is 89 ± 49 cm for the reported period, with a local estimate at the NEEM site of 124 ± 51 cm in surface elevation change.

The analysis of the CryoSat-2 L1b data around NEEM also shows an overall increase in surface elevation, when comparing data prior and post the 2012 melt event. The regional analysis of L1b data, retracked with the 20% threshold, shows an average surface height increase of 56 ± 26 cm, that agrees well with the local analysis which shows a slightly lower average of 50 ± 37 cm at NEEM. Figure 2 shows the time series and histogram of the detrended surface elevations for the regional estimated change in elevation. In Fig. 2a a clear positive change in surface elevation can be detected at the time of the melt event

with a ∼42% larger magnitude than for the previous year. The signal persists over the 2013-2014 period, with the seasonal signal superimposed.

Fig. 3 shows histograms of the different waveform parameters and change in detrended elevations for the months of June and August. These histograms clearly indicate that there has been a major transition in the scattering properties, where the magnitude varies with the different parameters. Analysing the different parameters we find that the backscattering coefficient (Bs) and pulse peakiness (PP) parameters have increased in magnitude over the event by 4.5% and 33%, respectively. This is in contrast to the leading edge width (LeW) and trailing edge slope (TeS) parameters that have decreased in magnitude by 55% and 29%, respectively. The most prominent change can be observed in the PP and LeW parameters, which indicate that the surface has become more specular after the event. The increase in specularity is also followed by a prominent reduction in signal penetration depth and surface roughness, indicated by the decrease in the LeW parameter. This pattern can also be detected in the standard deviation of the elevation difference in the satellite crossover points. Comparing the months of June and August, the standard deviation of the elevation difference of the crossovers (June-August) was reduced from 26 to 18 cm, supporting a decrease in surface roughness seen by the Bs and PP parameters.

Analysing the time series in Fig. 4 the 2012 melt event can clearly be detected in the waveform data. Clear shifts can be detected in Fig. 4 at the time of the melt event, connecting the change in scattering properties to the observed change in elevation. Large signals or transitions can be seen in all four parameters, most evident in the LeW and TeS parameters. The TeS parameter shows the largest change, as seen in Fig. 4d, with

an difference in magnitude of 85%. This change is not observed in the histograms of the June-August comparison, as it can only be observed in the month of July and after which it quickly recovers. The Bs and LeW parameters show a clear anti-correlation post event, whereas the Bs decreases as the LeW increases, indicating a build up of a new snow cover at the NEEM site.

4. Validation

The NEEM site was manned during the 2012 melt event. Therefore, in-situ observations are available from the site to validate the measured CryoSat-2 data at that time. The observations indicate that the NEEM snow surface lowered in elevation between July 11 and July 18. The Greenland Climate Network (GC-NET) automatic weather station (AWS) [*Box and Rinke*, 2003] at the site recored daytime surface air temperatures above 0°C from July 10 to July 15 and rain was observed on July 11 and 13. The surface snow was compacted as a result, with the AWS indicating a decrease in surface snow height of 13 ± 3 cm, based on the July 5 - 10 versus the July 18 - 23 mean. The AWS data are confirmed by in-situ observations of snow surfaces having lowered by 10 to 15 cm around camp structures. It is inferred that the snow surface beneath the camp structures was not significantly compacted because they were not directly exposed to sunlight, rain and surface air temperatures.

A series of snow pits were sampled at NEEM between June 30 and July 29, documenting the extensive warming of the topmost 60 cm of the snow surface and the formation of several solid ice layers. Daily snow temperature measurements indicate that the upper 20 to 60 cm of the NEEM snowpack was at melting point (-0.3 ± 0.5 °C) between July

12 and July 16. The formation of ice layers as a result of the warming is evident in Fig. 5, where snow density is shown for snow pits sampled before and after the melt event. Pre-melt stable water isotopes δ^{18}O (Fig. 5) indicate summer and winter deposition strata [*Kuramoto et al.*, 2011]. The snow pit sampled on June 29 shows snow densities consistently less than 400 kgm^{-3} with higher densities corresponding to winter snow and lower densities corresponding to summer snow.

In contrast, the post-melting snow pit shows the formation of a thin ice layer at 29 cm depth and a thick ice layer at 76.5 cm depth below the post-melt snow surface. We note that the summer/winter density variations are retained in the post-melting snow pit, despite the occurrence of physical processes such as surface compaction, water percolation and ice layer formation. Several snow pits were sampled after the melt event, with ice layers usually present between 10 - 30 cm and 50 - 70 cm depth. These observations are in agreement with earlier reports from the site [*Nghiem et al.*, 2012] where ice layers were reported to have formed at approximately 5, 20 and 69 cm depth. We therefore attribute the range of ice layers to the range 50$\pm$30 cm below the post-melt snow surface.

The surface observations presented here can be compared to theoretical calculations of the Cryosat-2 signal penetration depth to investigate the magnitude of possible elevation bias due to ice layer formation. Dielectric signal penetration models estimate the penetration depth of a Ku-band radar into the dry snow zone, based on various assumptions for snow density, temperature, impurity content, imaginary permittivity and signal frequency. *Stiles and Ulaby* [1980] determined a signal penetration depth of approximately 100 cm in dry snow, with an order-of-magnitude reduction of penetration depth in wet snow or ice.

The snow pit observations pre and post event confirms the assumption of dry snow condition. Hence, the theoretical penetration depth should be valid for unstratified firn. From Fig. 5, it can be seen that the penetration depth calculated for dry snow includes summer and winter snow strata from calendar years 2012 and 2011. Following the melt event, the relatively dense (>500 kg m^{-3}) ice layers would present a strong dielectric discontinuity and hence strongly reflect Ku-band energy. Considering a surface elevation lowering of 13 $\pm$ 3 cm and the formation of ice layers in the range of 50 $\pm$ 30 cm below the post-melt snow surface, we can estimate the post-melt Ku-band penetration depth would have been elevated from a depth of approximately 100 cm (pre-melt) by 37 $\pm$ 31 cm. This positive change in penetration depth led to the apparent surface elevation increase observed in the CryoSat-2 data product.

5. Discussion

The rapid change in the surface conditions of the interior parts of the GrIS manifest itself as an apparent and sudden increase in surface elevation, as observed by CryoSat-2. The magnitude of this elevation bias is found to be 89 $\pm$ 49 when analysing L2i elevation data, which is reduced to 56 $\pm$ 26 cm when analysing the regional data derived from the L1b product around the area of NEEM. The increase in magnitude of the observed surface elevation can clearly be detected in the temporal signal of elevation change in the region around NEEM, as seen in Fig. 2, where both the histogram and time series of the change in elevation show the introduction of a positive elevation bias in the retracked L1b data. An elevation change of 56 cm would according to *Thomas et al.* [2008] correspond to a 336 Gt increase in mass of the GrIS in the areas above 2000 m in elevation, if it is

assumed to be caused by snowfall. Such large mass changes at these elevation are not physical plausible.

The waveform parameters, seen in Fig 3-4, indicates that the elevation bias has been introduced by a transition in scattering properties of the radar signal. In the dry snow zone of the GrIS, the melt event has changed the scattering regime from volume towards surface scattering, which can be explained by the formation of a strong internal reflective layer in the form of ice lenses within the upper most snowpack. The presence of such a surface was indeed confirmed by in-situ observations at NEEM (Fig. 5). The changed snow conditions at NEEM suggested an increase in altitude of the radar reflector of 37 $\pm$ 31 cm, which is in good agreement with the obtained CryoSat-2 results. The transition from volume to surface scattering is especially apparent in the LeW waveform parameter, where a dramatic reduction in the width of the leading edge is observed at the time of the melt event. This reduction of the width of the leading edge is synonymous to a decrease in the magnitude of the surface penetration of the signal, i.e a reduction in volume scattering.

The time series of the waveform parameters in Fig.4 show a clear signal, at the time of the melt event, in all four parameters. However, the behaviour and duration of the signals varies with the different parameter which are connected to the physical interpretations of the parameters. The Bs, PP and TeS parameters are for example especially sensitive to the specularity of the surface. Therefore abrupt spikes in these parameters would be expected when the surface becomes wet, as the smoothness of the surface increases. This behaviour is also observed in these parameters, as seen in Fig. 3-4, at the time of the melt event. These signals are expected to be short lived as the cm-scale surface roughness will

increase when the surface refreezes, reducing the scattered power. The LeW parameter however is expected to be more long lived, as it is more governed by surface penetration effects.

Analysing the waveform parameters over time, Fig. 4, its found that the melt event signal in the LeW parameter is more stable, as expected, compared to the other three parameters. It shows a distinct decrease at the time of the event and can be seen to increase linearly as new snow is deposited on the surface. This behaviour is also noted in the Bs parameter, where a linear decrease is observed post the event anti-correlated with the LeW parameter. This anti-correlation is expected as the surface roughness and surface penetration will increase with new snow deposition. The behaviour of these parameters increases the confidence that we are in fact measuring real and physical signals in our waveform parameters. However, from the Bs, PP and TeS parameters alone its not clear if the melt event signal is short or long lived. The LeW-parameter on the other hand provides support of the notion that the elevation bias would be more long lived. This as the reflective ice layer would be the dominate scatterer until enough snow have been deposited to bury the ice layer below the maximum penetration depth of the signal. This is also what we observe in the time series of the elevation change in Fig. 2a, where at the time of the melt event the magnitude of the elevation change signal increases twofold and persist for a duration of approximately one year, superimposed on the yearly cycle.

The scattering parameters clearly indicate a change in the reflective surface, and attempts to derive surface elevation changes needs to incorporate such changes. *Flament and Rêmy* [2012] proposed a least-squares model for the bias correction of a changing

reflective surface. However, the ESA CryoSat-2 L2i product does not currently give sufficient information to undertake such efforts and the intermediate L2i data only partly gives the information needed. It also not clear if this type of approach would give the desired results, this as the model is derived to account for rapid and spurious changes around the mean value of the waveform parameters. We have here shown that the signal is not spurious but instead long lived and thus the least squares model might not be capable to account for this type of signal.

Another possible approach could be to apply a bias correcting scheme, defined from the pre-post melt event height data. Caution is advised when interpreting or using this derived elevation bias, estimated here in this study, for adjustments of elevation change time series, as the bias is not only spatially variable but also directly proportional to the retracking correction applied. This is clearly evident when analysing the L2i and L1b data, where the difference at NEEM is roughly 60% between the two data sets. The use of different retracking thresholds can easily introduce variations of 70 cm, as observed in this study when determining the optimal retracking threshold. Hence knowledge of the retracker and its applied retracking correction is important when trying to account for these types of events. The melt event does however provide an interesting opportunity to investigate the retracker dependent surface penetration on a continental wide scale. This has previously only been possible using airborne laser data or other non-contemporary satellite missions, such as ICESat.

Detecting these types of events in radar altimetric data is of great importance for determining their usability. From the case study around NEEM, we suggest that the

LeW and TeS parameters could be used to detect these types of major event in radar altimetry data, as they clearly show the largest measurable change (see Fig. 4 c,d). The TeS parameter is here of extra interest as it can be used to detect melt water on the ice sheet surface, giving a very precise timing of the event. This is due to that water with a smooth surface is very specular, which makes the trailing edge slope extremely sharp. Once the refreezing process has begun the surface roughness will increase and thus the absolute magnitude of the TeS signal will be lowered, as seen in Fig. 4d.

Our recommendations for the use of the Cryosat-2 L2 product, for now, is to flag measurements subject to abnormal melt conditions such as the 2012 melt event, and wait for dry snow conditions to reoccur. This challenges the application of radar altimetry to study elevation changes of ice sheets in a warming climate, such findings are also relevant to locations in Antarctica where the equilibrium line altitude is rapidly increasing.

6. Conclusion

The 2012 record melt introduced into the CryoSat-2 data products a significant ice sheet wide elevation bias in the GrIS dry snow zone (Fig. 1). In the proximity of the NEEM site the elevation change bias was found to be 56 $\pm$ 25 cm, obtained from a detailed analysis of processed Cryosat-2 L1b data presented in this study. This is in contrast to the ESA L2i derived elevation change bias, which was found to be 89$\pm$49 cm for the same area.

Theoretical modelling of radar penetration depth in conjunction with in-situ measurement were able to explain the bias as non mass related. The bias was explained by the introduction of ice layers in the upper firn layers, which acts as strong reflectors for the radar signal emitted by CryoSat-2, and transforms the scattering regime from volume

to near surface scattering. Detailed analysis of the waveform parameters confirms this interpretation, where an abrupt change in the magnitude of all four waveform parameters is observed at the time of the melt event.

The estimated magnitude of the elevation change bias also showed a clear relation to the applied retracker correction. Hence, information about the applied retracking correction is of large importance when trying to account for these types of events, as the size of the correction has an direct effect on the magnitude of the elevation bias. Despite the induced bias in elevation time series of the GrIS, the 2012 melt event provide an unique opportunity to study the radar penetration depth in the interior part of ice sheets and evaluate retracker dependencies in relation to altimetry derived mass balance studies.

Acknowledgments. This publication is contribution number 47 of the Nordic Centre of Excellence SVALI, Stability and Variations of Arctic Land Ice, funded by the Nordic Top-level Research Initiative (TRI). NEEM is directed and organized by the Center of Ice and Climate at the Niels Bohr Institute and US NSF, Office of Polar Programs. It is supported by funding agencies and institutions in Belgium (FNRS-CFB and FWO), Canada (NRCan/GSC), China (CAS), Denmark (FIST), France (IPEV, CNRS/INSU, CEA and ANR), Germany (AWI), Iceland (RannIs), Japan (NIPR), Korea (KOPRI), The Netherlands (NWO/ALW), Sweden (VR), Switzerland (SNF), United Kingdom (NERC) and the USA (US NSF, Office of Polar Programs). CryoSat-2 L1b and L2i data are available from the European Space Agency via download at (www.earth.esa.int). NEEM snow pit data are available from (www.iceandclimate.nbi.ku.dk/data).

References

ACS Team, and MSSL Team (2011), CRYOSAT ground segment, instrument processing facility l2, l2 products format specification, *European Space Agency*, *CS-RS-ACS-GS-5123*.

Box, J. E., and A. Rinke (2003), Evaluation of Greenland ice sheet surface climate in the HIRHAM regional climate model using automatic weather station data, *Journal of Climate*, *16*, 1302–1319, doi:10.1175/1520-0442-16.9.1302.

Davis, C. H. (1997), A robust threshold retracking algorithm for measuring ice-sheet surface elevation change from satellite radar altimeters, *IEEE Transactions on Geoscience and Remote Sensing*, *35*(4), doi:10.1109/36.602540.

Flament, T., and F. Rêmy (2012), Dynamic thinning of antarctic glaciers from along-track repeat radar altimetry, *Journal of Glaciology*, *58*(211), doi:10.3189/2012JoG11J118.

Forsberg, R., L. Sørensen, J. Levinsen, and J. Nilsson (2013), Mass loss of greenland from grace, icesat and cryosat, *Proceedings of the CryoSat Workshop, Dresden, ESA Special Publication 717, Paper S6-4*.

Hall, D. K., J. C. Comiso, N. E. DiGirolamo, C. A. Shuman, J. E. Box, and L. S. Koenig (2013), Variability in the surface temperature and melt extent of the greenland ice sheet from modis, *Geophysical Research Letters*, *40*(10), 2114–2120, doi:10.1002/grl.50240.

Huining, W., J. Pulliainen, and M. Hallikainen (1999), Effective permittivity of dry snow in the 18 to 90 ghz range, *Progress In Electromagnetic Research*, *24*, 119–138, doi:10.1163/156939399X00727.

335 Johannessen, O. M., K. Khvorostovsky, M. W. Miles, and L. P. Bobylev (2005), Re-
336 cent ice-sheet growth in the interior of greenland, *Science*, *310*(5750), 10131016, doi:
337 10.1126/science.1115356.

338 Khvorostovsky, K. S. (2012), Merging and analysis of elevation time series over green-
339 land ice sheet from satellite radar altimetry, *Geoscience and Remote Sensing, IEEE*
340 *Transactions on*, *50*(1), 23–36, doi:10.1109/TGRS.2011.2160071.

341 Kuramoto, T., K. Goto-Azuma, M. Hirabayashi, T. Miyake, H. Motoyama, D. Dahl-
342 Jensen, and J. P. Steffensen (2011), Seasonal variations of snow chemistry at neem,
343 greenland, *Annals of Glaciology*, *52*(58), 193–200, doi:10.3189/172756411797252365.

344 Laxon, S. (1994), Sea ice altimeter processing scheme at the eodc, *International Journal*
345 *of Remote Sensing*, *15*.

346 Legresy, B. L., and F. Rêmy (1997), Altimetric observations of surface characteristics of
347 the antarctic ice sheet, *Journal of Glaciology*, *43*(144).

348 Li, Y., and C. H. Davis (2008), Decadal mass balance of the greenland and antarctic
349 ice sheets from high resolution elevation change analysis of ERS-2 and envisat radar
350 altimetry measurements, *Geoscience and Remote Sensing Symposium, IGARSS 2008.*
351 *IEEE International*, *4*(IV-339), doi:10.1109/IGARSS.2008.4779727.

352 Mätzler, C., and U. Wegmüller (1987), Dielectric properties of fresh-water ice at microwave
353 frequencies, *Phys. D: Appl. Phys*, *20*, 1623–1630.

354 Nghiem, S. V., D. K. Hall, T. L. Mote, M. Tedesco, M. R. Albert, K. Keegan,
355 C. A. Shuman, N. E. DiGirolamo, and G. Neumann (2012), The extreme melt
356 across the greenland ice sheet in 2012, *Journal of Glaciology*, *54*(185), 203–212, doi:

doi:10.1029/2012GL053611.

Scott, J. B. T., P. Nienow, D. Mair, V. Parry, E. Morris, and D. J. Wingham (2006), Importance of seasonal and annual layers in controlling backscatter to radar altimeters across the percolation zone of an ice sheet, *Geophysical Research Letters*, *33*, L24,502, doi:doi:10.1029/GL027974.

Stiles, W. H., and F. T. Ulaby (1980), Dielectric properties of snow, nasa contract, *Tech. Rep. CR 166764*, rep.,CR166764,43 pp.

Thomas, R., C. Davis, E. Frederick, W. B. Krabill, Y. Li, S. Manizade, and C. Martin (2008), A comparison of greenland ice-sheet volume changes derived from altimetry measurements, *Geophysical Research Letters*, *39*, L20,502, doi: 10.3189/002214308784886225.

Zwally, H., L. Jun, A. Brenner, M. Beckley, H. Cornejo, J. Dimarzio, M. Giovinetto, T. Neumann, J. Robbins, J. Saba, and et al. (2011), Greenland ice sheet mass balance: Distribution of increased mass loss with climate warming 2003-2007 versus 1992-2002, *Journal of Glaciology*, *58*(201), 88102, doi:10.3189/002214311795306682.

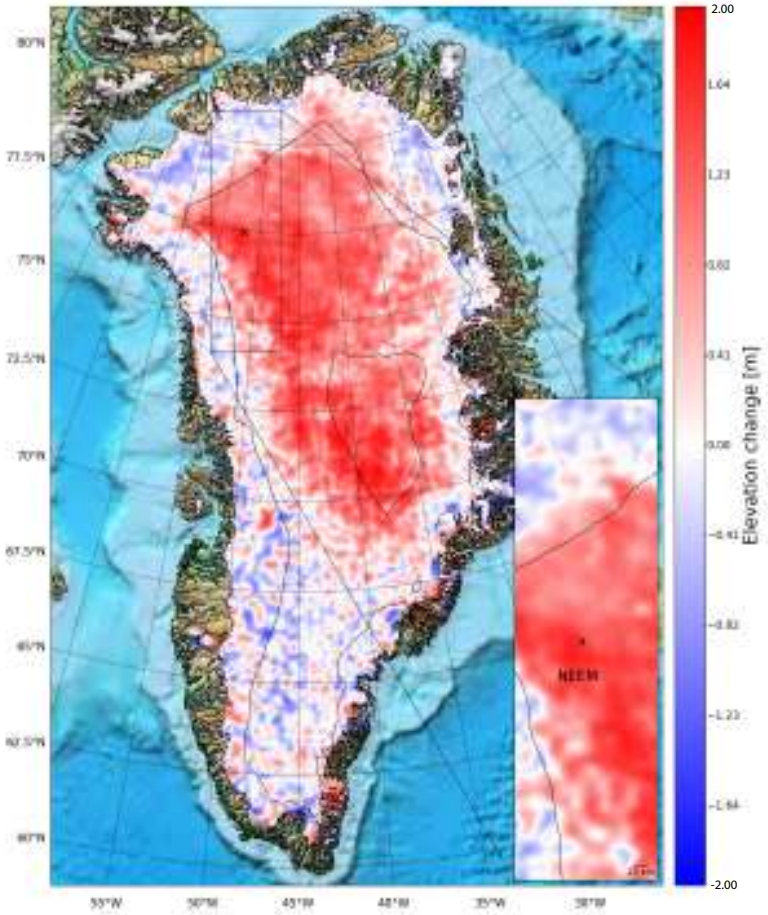

Figure 1. Surface elevation difference between May-June and August-September CryoSat-2 L2i data. The difference in surface elevation show a clear positive surface increase in the dry snow zone and ablation in the coastal regions. Black lines indicate the 2000 and 3000 m elevation contours.

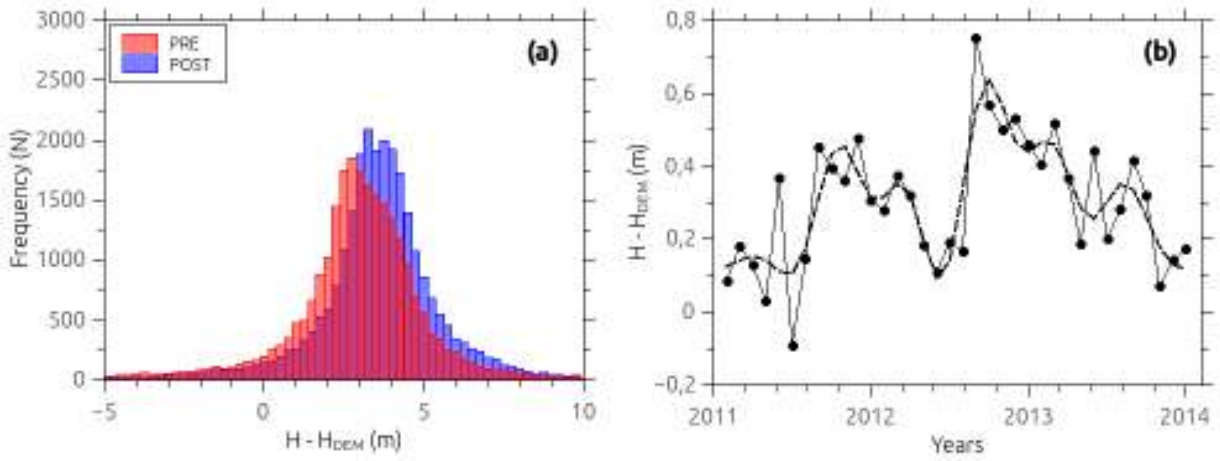

Figure 2. Histogram **(a)** (June and August 2012) and surface elevation change time series **(b)** (2011-2014) of de-trended surface elevations estimated regionally around the NEEM site using the elevations produced from the CryoSat-2 L1b product. Both figures show a clear positive change in surface elevation at regional scale at the time of the melt event. The dashed line in **(b)** is a smoothed version of the elevation change time series.

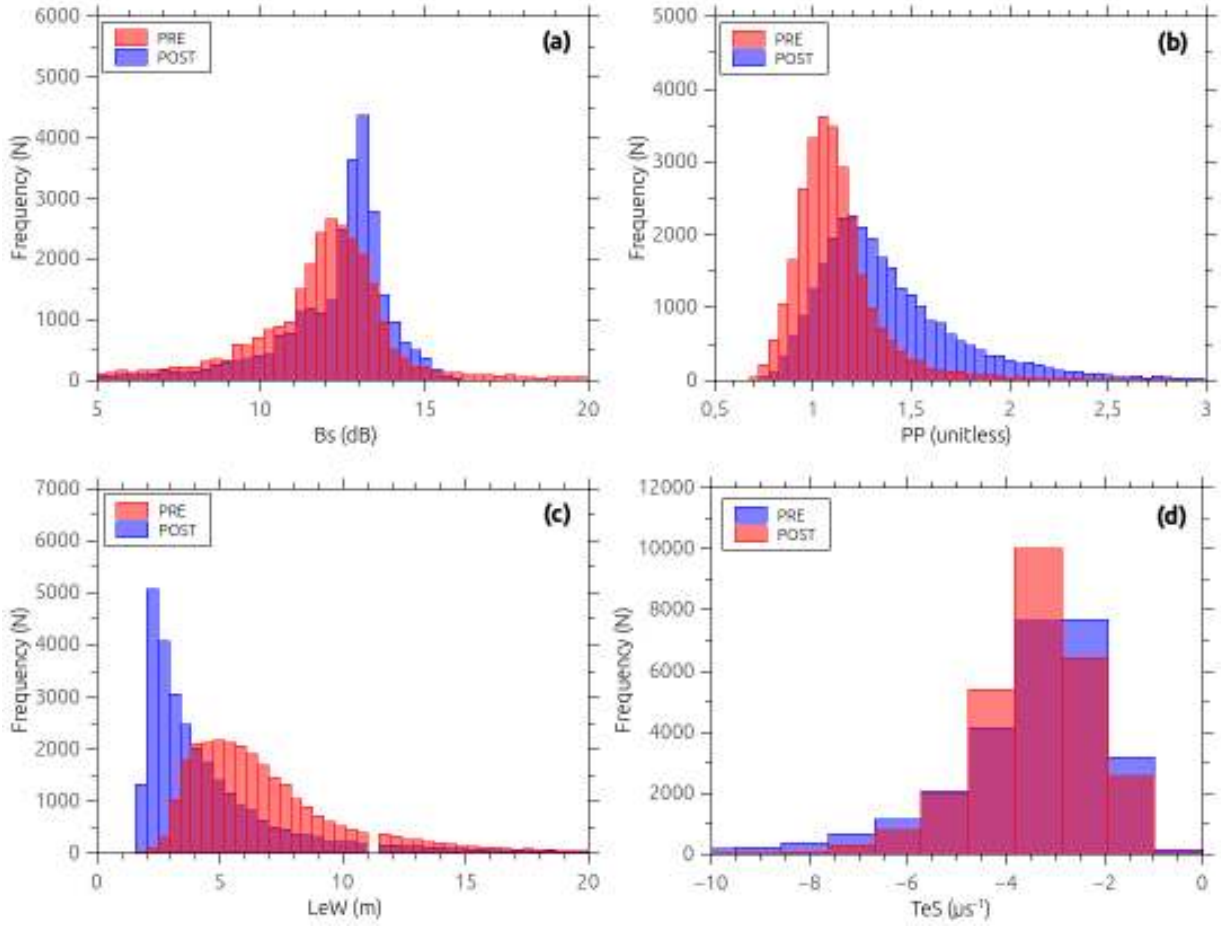

Figure 3. Histograms of the backscattering coefficient **(a)**, pulse peakiness **(b)**, leading edge width **(c)** and the trailing edge slope **(d)** estimated from the regional analysis. Three of the four waveform parameters demonstrate a clear change in magnitude between the month of June and August 2012, except the TeS parameter.

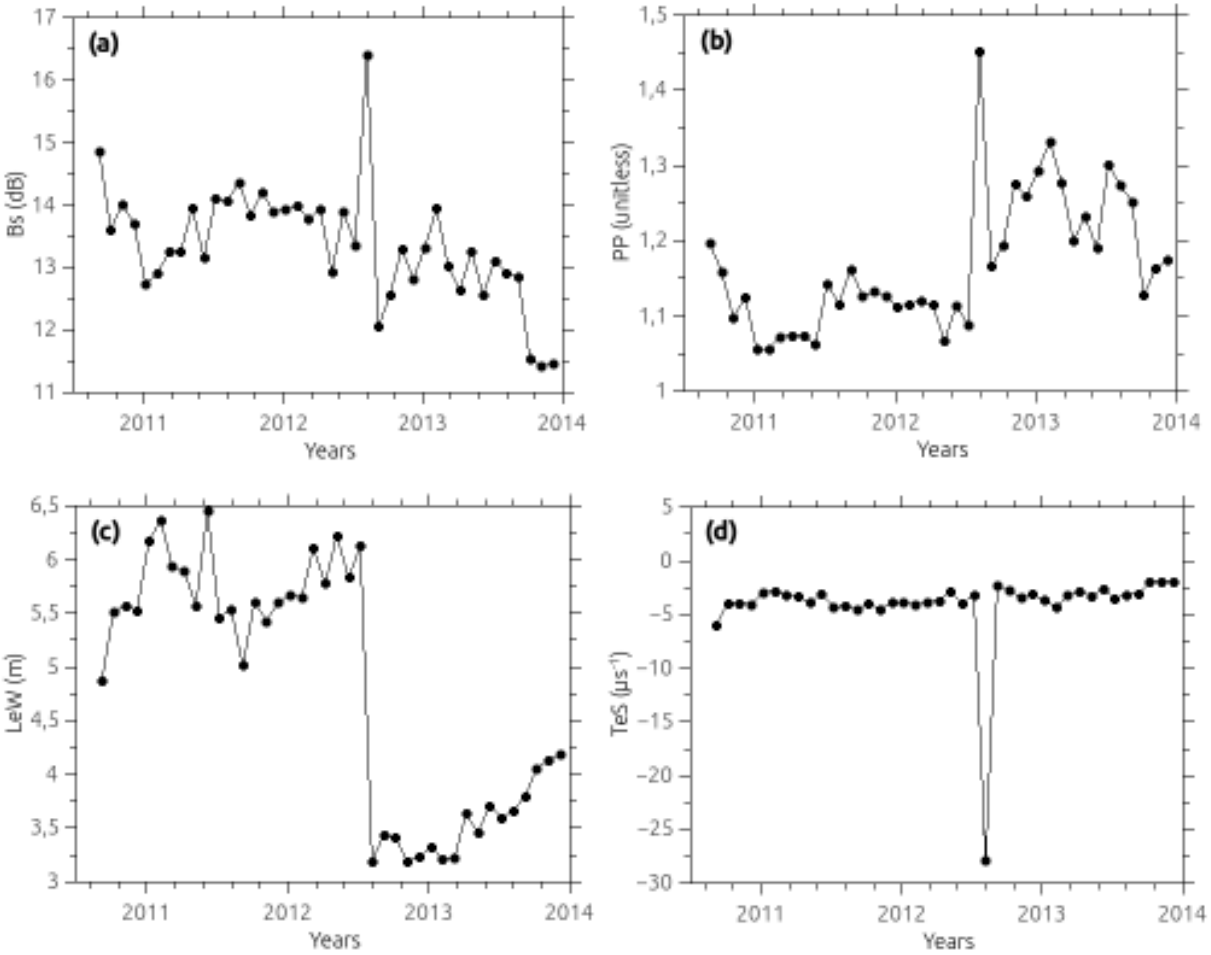

Figure 4. Time series of the backscattering coefficient **(a)**, pulse peakiness **(b)**, leading edge width **(c)** and trailing edge slope **(d)** estimated using a radius of $\sim 0.2°$ around the NEEM site. This using the elevations produced from the CryoSat-2 L1b product. The four waveform parameters all show clear change in magnitude at the time of the melt event.

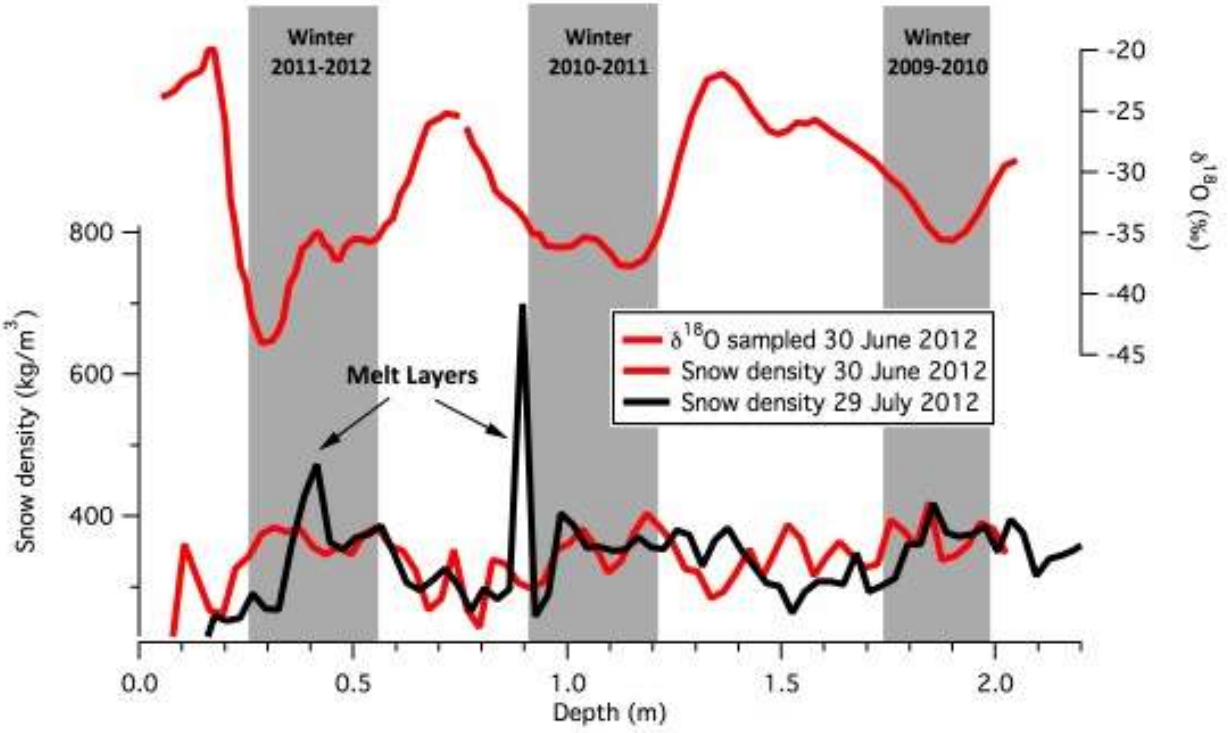

Figure 5. Density and oxygen isotope measurements from two snowpits sampled at NEEM site before and after the July 2012 melt event. The presence of ice layers after the melt event are clearly demonstrated by densities greater than 400 kgm^{-3}. Winter snow deposition layers were determined by oxygen isotope ratios and are indicated by gray bars. Note that the July 29 density profile depths have been corrected for the 13 cm lower post-melting surface.

B Posters

This appendix contains a representative selection of posters relevant for the work done in this thesis, which have been presented at various conferences around the world.

Changes of the Arctic Ice Caps from ICESat and GRACE
A study of mass balance

Johan Nilsson[1], Louise Sørensen[1], Valentina Barletta[1] and René Forsberg[1]

[1]DTU Space - National Space Institute, Technical University of Denmark, Building 327, Elektrovej, 2800 Kgs. Lyngby, Denmark.

jnils@space.dtu.dk

DTU Space
National Space Institute

SVALI

Introduction

The Arctic ice caps are the main contributors to near future sea level rise. To quantify the spatial pattern and rate of the mass change is of fundamental importance to understand their future implications for socity. With the introduction of satellite remote sensing new opportunities to address these issues have opened up.

To quantify the mass change of the Arctic ice caps their change in elevation was measured during the period **2003-2009**. This was done using **"Ice, Cloud, and land Elevation Satellite" (ICESat)**. Which was then independently compared to **"Gravity Recovery and Climate Experiment" (GRACE)** derived solutions for the same time and regions (except Alaska).

Previous studies in these regions have mostly used one or the same family of methods to derive the regional mass balance. Due to the usual poor spatial coverage of both airborne and spaceborne methods over glaciers the mass balance results (from altimetry) are usually very sensitive to the method used. So the focus of this study have been to reduce this effect. This was done by incorporating several different more independent methods to attain a more reliable mass balance estimate.

For this study the Arctic ice caps were divided into five regions (excluding Greenland): **Svalbard, Iceland, Canadian Arctic North and South (Ellesmere and Baffin Island) and Alaska**.

ICESat Mission

GRACE Mission

Estimating Mass Change

The height changes are estimated by the **repeat-track** method. This method divides the tracks into 500 m segments and in every segment a plane is fitted to the observations.

$$h_{ij} = \begin{pmatrix} A_{ij} \\ B_{ij} \\ \alpha_{ij} \\ \beta_{ij} \\ \left(\frac{dh}{dx}\right)_{ij} \\ \left(\frac{dh}{dy}\right)_{ij} \end{pmatrix} (t, 1, \cos(\omega t), \sin(\omega t), (x - x_0), (y - y_0))$$

where $A_{ij} = \left(\frac{dh}{dt}\right)_{ij}$ is the surface elevation change, $\left(\frac{dh}{dx}\right)_{ij}$ is the along-track slope, $\left(\frac{dh}{dy}\right)_{ij}$ is the cross-track slope, B_{ij} is an estimation of the underlying topography, $(x - x_0)$ and$(y - y_0)$ is the centroid of the area which is spanned by the observations in the segment, α and β are the amplitudes of the seasonal function.

These parameters are then estimated by a least square solution $\hat{x} = [A^T A]^{-1} A^T y$. The height changes are then interpolated into a regular space grid **(1-by-1 km)** and extracted by a glacier mask.

$$\left(\frac{dM}{dt}\right) = \sum \left(\frac{dh}{dt}\right) \cdot A_{pix} \cdot \rho \qquad (1)$$

$$\left(\frac{dM}{dt}\right) = \sum \left(\frac{dh}{dt}(h) \cdot A(h)\right) \cdot \rho \qquad (2)$$

To obtain mass changes we need to apply a density conversion scheme: This is done by using a ELA-like procedure. Where all positive dh/dt are assumed to be accumulation and will be given density of firn **(500 kg m^{-3})**. All negative dh/dt are assumed to be due to ablation and given the density of ice **(900 kg m^{-3})**

References

[1] L. Sørensen, S.B Simonsen, K. Nielsen, P. Lucas-Picher, G. Spada, G. Adalgeirsdottir, R. Forsberg, C.S Hvidberg: Mass balance of the Greenland ice sheet (2003-2008) from ICESat data - the impact of interpolation, sampeling and firn density. The Cryospehere, 5, 173-186. doi:10.5194/tc-5-173-2011, 2011.

[2] S. Luthcke, A. Arendt, D. Rowlands, J. McCarthy, C. Larsen: Recent glacier mass changes in the Gulf of Alaska region from GRACE mascon solutions. Journal of Glaciology, Vol. 54, No. 188, 2008.

Estimating Regional Mass Change

To derive the regional mass balance four methods where used divided into two families: Interpolation and Extrapolation.

- **Ordinary Kriging** (1)
- **Ordinary Kriging - Elevation Paramtrization** (1)
- **Hypsometric Averaging - Polynomial** (2)
- **Hypsometric Averaging - Median** (2)

To determine the optimum method for the different regions we used the statistical criteria applied to the elevation change distribution:

$$\mu_s = \min(|\mu_o - \mu_m|) \qquad (3)$$

where (μ_s) is the mean shift, (μ_o) original mean and (μ_m) mean of method.

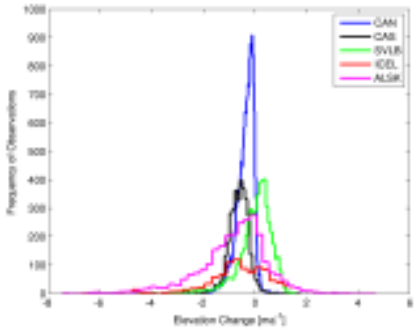

Histogram of elevation changes for the different regions

Region	Area [km^2]	$\dot{V}$ [km^3 a^{-1}]	$\dot{V}_A$ [m a^{-1}]
Svalbard	33 673	-2.3	-0.07
Iceland	10 989	-11.9	-1.1
CAN	103 990	-40.6	-0.4
CAS	40 601	-28.1	-0.7
Alaska	84 926	-99.5	-1.1

The total glaciated area (Area), mean volume change ($\dot{V}$) and the area averaged mean volume change ($\dot{V}_A$).

Elevation Changes of the Arctic Regions (2003-2009)

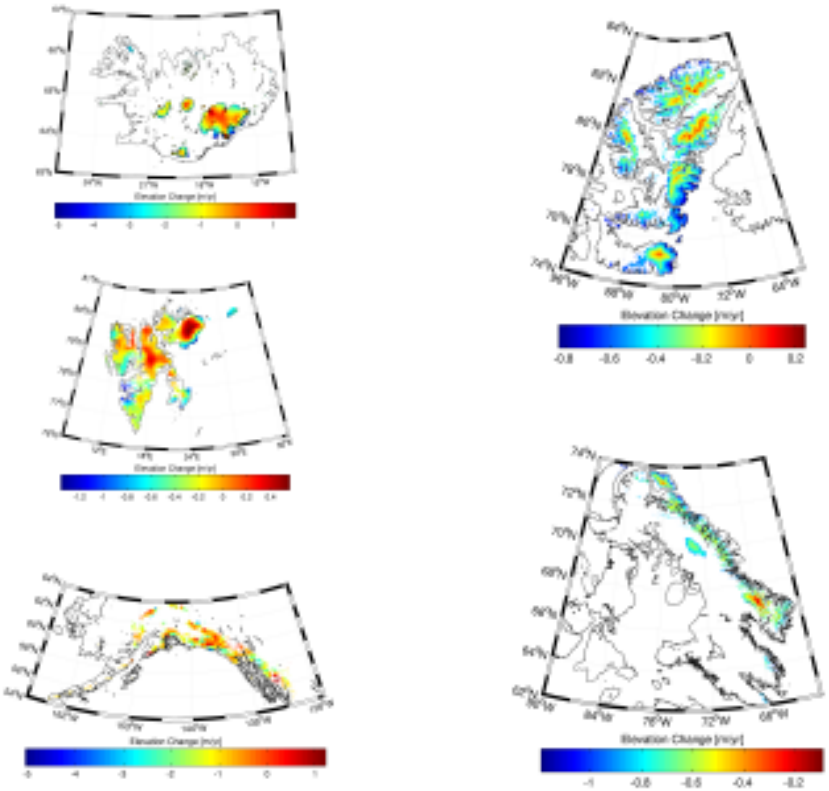

Results and Comparison

- All four methods show mass balance convergence for regions with stable climatic conditions (uniform dh/dt), such as the Canadian Arctic.
- Areas with a more maritime climate, such as Iceland and Svalbard, shows a larger mass balance range (in order of the error estimates).
- In general hypsometric averaging and Kriging methods have a tendency to over and underestimate the mass balance. Compared to the original distribution.

Region	ICESat	Range	GRACE
Svalbard	-4.5 ± 2	2	-1.7 ± 1.5
Iceland	-11 ± 2.5	4	-4.0 ± 3
CAN	-37 ± 8	3	-42 ± 10
CAS	-25 ± 5	1	-25 ± 8
Alaska	-90 ± 21	50	-84 ± 5

*Mass change estimates in **Gta**$^{-}$1 from ICESat and GRACE. The Alaska GRACE estimate is taken from [2]*

Conclusions

- The type of climatic regime of the region/area has a large impact on the mass balance estimates from the different methods.
- In general both interpolation and extrapolation should be used to derive mass balance (especially for regions with high dh/dt variability).
- Regions with a continental climate regime are less sensitive to the choice of methods to derive regional mass balance. This generally due to their more uniform spatial pattern of elevation change.
- A optimum method can be chosen using the statistical criteria of minimum shift for most regions. Under the assumption that the spatial coverage is large enough to resolve the glaciated areas of the region.
- For regions with high variability (elevation change) the mean value of several or all methods is more representative of the original distribution. This due to the negative and positive shifting introduced by the two families.

DTU Space
National Space Institute

Retrieving improved multi-temporal CryoSat-2 elevations over ice caps and glaciers - A case study of Barnes ice cap

Johan Nilsson[1] and David Burgess[2]

Introduction

The CryoSat-2 mission was launched in late 2010 to observe the changes in the Earth's cryosphere and in contrast to other previous satellite altimetry missions, this mission is expected to monitor the elevations of small ice caps and glaciers due finer spatial sampling and mapping of across-track echos by interferometry. In this study we explore the possibility to derive accurate estimates of elevation and elevation changes from SARin L1B data in the Canadian Arctic, using an newly developed SARin processor. The accuracy of our L1B processing has so far been determined over Barnes ice cap and been compared to ESA processed L2 elevations and ICESat elevation changes.

Data and Processing

An in-house developed SARin L1B processor was used to derive surface elevations over Barnes ice cap in the Canadian Arctic using the ESA L1B product for 2010-2014. The re-tracking algorithm in the processor is specifically built to track the first return in the power waveform. Phase noise is then reduced by filtering of the Interferogram and phase ambiguities are corrected using an external DEM (CDED).
NASA airborne ATM data from April 2011 was used to validate the SARin processor and the derived surface elevations were then compared to ESA processed CryoSat-2 L2 for accuracy comparison. Elevation changes for 2010-2014 were later estimated and compared to ICESat derived changes from 2003-2009.

Elevation change methods

Elevation change rates over Barnes ice cap were determined using three independent methods

(1) Reference/Repeat track method, fitting of ridgid planes (RT)
- $dH = a(x - x_0) + b(y - y_0) + (dh/dt)(t - t_0) + c(b - b_0)$

(2) Crossover method (XO)
- $dH = H_2 - H_1$

(3) Elevation residual method (HD)
- $dH_{21} = dH_2 - dH_1$ where $dH_{1,2} = H - DEM$

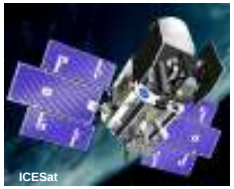

Accuracy of CryoSat-2 compared to ATM

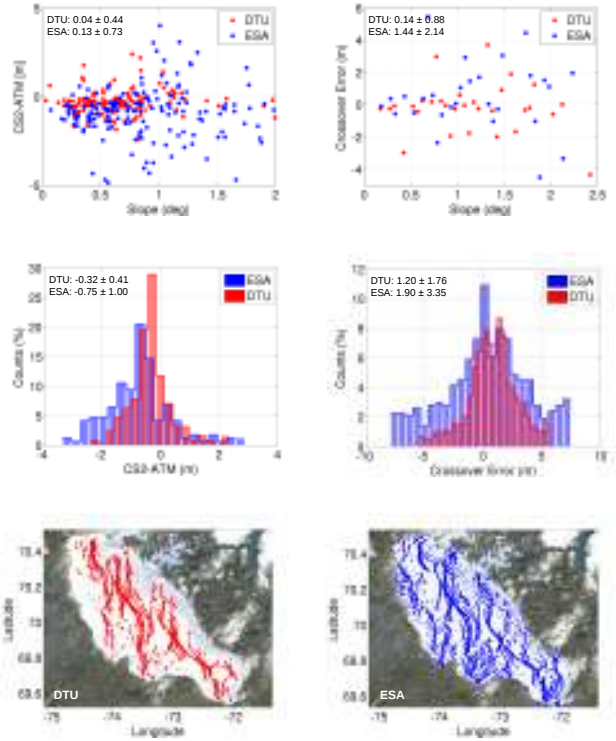

Accuracy of the CryoSat-2 (CS-2) SARin processor was determined using NASA ATM data from April 2011 with CryoSat-2 data from Feb-June 2011. The crossover error (re-tracking+orbit errors) was determined using a dt < 30 days. CS2 SARin data shows very small A/D biases on the cm level.

Elevation changes from CryoSat-2 and ICESat

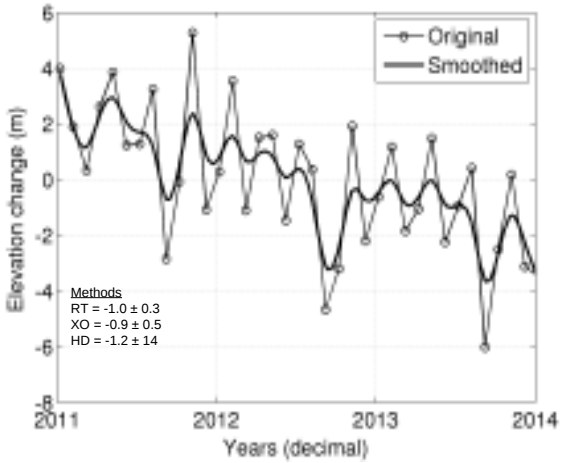

Monthly time series of elevation change estimated from CryoSat-2 (DTU) elevations, using the (HD) method.

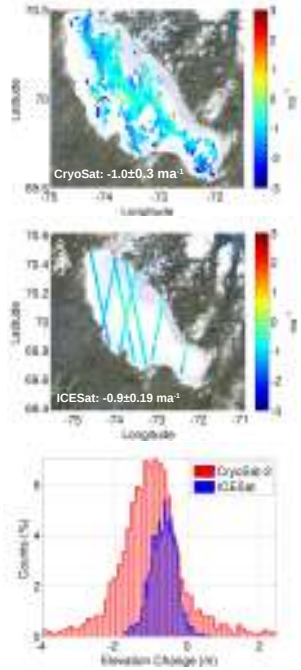

ICESat and CryoSat-2 elevation changes from 2003-2009 and 2010-2014 respectively, using the RT method

Conclusions

- The new SARin processor show an overall improvement in accuracy compared to the current ESA SARin L2 processor.
- Elevation changes obtained from CryoSat-2 show good agreement with ICESat derived elevation change rates for Barnes.
- Trends and seasonal signals can be detected using CS-2 observations over smaller ice caps and glaciers.
- Phase noise and phase ambiguities are the main governing factors in the overall accuracy of CS-2 SARin observations.

Acknowledgment

The author would like to thank Dr. Laurence Gray (University of Ottawa) for the use of his geocoding algorithm and his overall help during the development of this SARin processor. Further we would like to thank the NSIDC and NASA for delivering the ICESat and ATM data, and ESA for their L1B and L2 data products.

[1]DTU Space, National Space Institute, Technical University of Denmark, Elektrovej Bygning 327, 2800 Kgs. Lyngby, Denmark, Email: jnils@space.dtu.dk
[2]Geological Survey of Canada, Ottawa, Ontario, K1A 0E8, Canada, Email: david.burgess@nrcan-rncan.gc.ca

DTU Space
National Space Institute

Greenland Ice Sheet elevation changes estimated from Cryosat-2 observations from 2010-2014

Johan Nilsson[1], Louise Sandberg Sørensen[1], Rakia Meister[1], Valentina R. Barletta[1,2] and René Forsberg[1]

Introduction

The CryoSat-2 mission was launched in late 2010 to observe the changes in the Earth's cryosphere and in contrast to other previous satellite altimetry missions, this mission is expected to monitor the elevations of small ice caps and glaciers due finer spatial sampling and mapping of across-track echos by interferometry. In this study surface elevation changes of the Greenland Ice Sheet have been estimted from 2010-2014 using the LRM and SARIN-mode of CryoSat-2 (CS2) mission. The resulting elevation changes where then compred to elevation changes obtain from the ICESat (2003-2008), ENVISAT (2006-2010) and the GRACE (2003-2013) missions. The accuracy and precision of the estimated elevation and elevation changes where then compared to IceBridge ATM-derived elevations and elevation changes (2011-2013)

Elevation and Elevation change

An in-house developed SARin and LRM L1B processor was used to derive surface elevations over the entire Greenland Ice Sheet, using the ESA L1B product for 2010-2014. The re-tracking algorithms in the processor are especially built to track the first return of the power waveform. Phase noise in the SARIN-mode is reduced by filtering of the Interferogram and phase ambiguities are corrected using an external DEM. The LRM data are further corrected for the slope-induced error using an external DEM.

The surface elevation changes are estimated using a linear model, taking into account: topography, ice sheet scattering conditions (waveform parameters) and several biase. The coefficiants of the model are found by a least-squares solution.

$$H = H_0 + a_1 dx + a_2 dy + a_3 dxdy + a_4 dx^2 + a_5 dy^2 + \frac{dH}{dt} dt + a_6 C + a_7 B + a_8 \cos(wt) + a_9 \sin(wt)$$

where the (C) parameter contains the correction due to changes in scattering properties (i.e waveform parameters) and (B) is the corrections for several different biases. The description of the waveform parameters and the height retrival can be seen in Fig. (1)

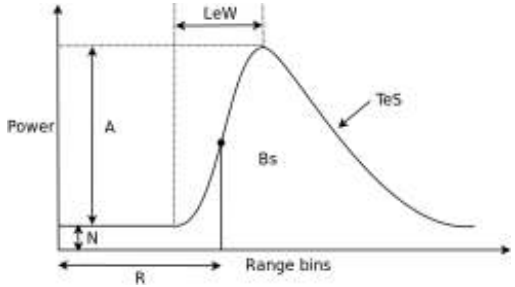

Fig (1): Schematic view of a radar altimetric waveform, depicting the estimated range (R) to the surface and the waveform shape parameters (Bs, LeW, TeS), which are used to correct for spurious changes in elevation caused by changes in the ice sheets scattering regime.

Elevation changes Greenland Ice Sheet

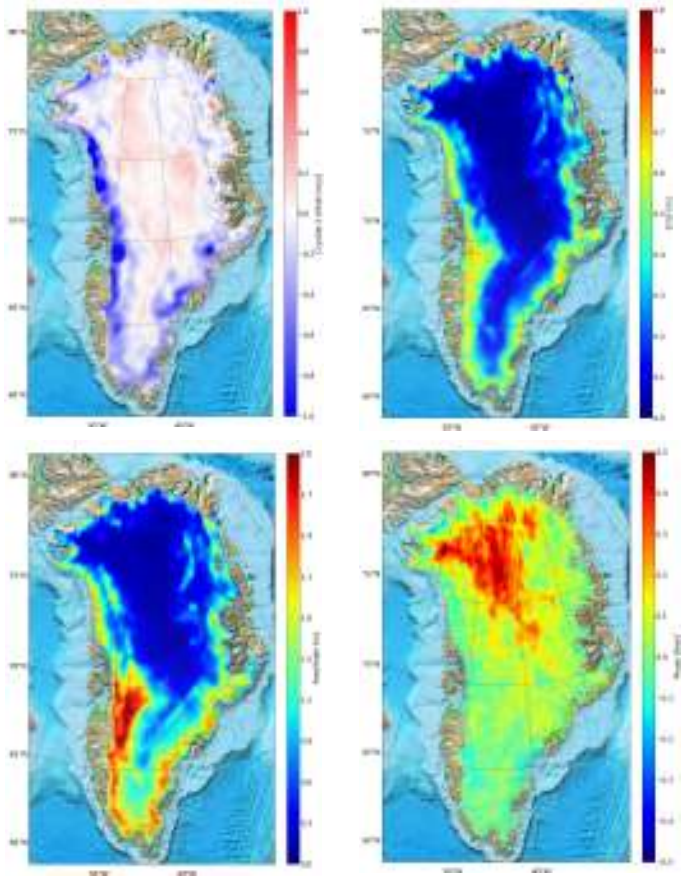

Accuracy and Precision from ATM

NASA airborne ATM data from April 2011-2013 was used to validate the SARIn and LRM processor derived surface elevations, using a gridded CryoSat-2 DEM-product from 2010-2014. The accuracy and precision of the estimated elevation changes was determined using ATM-derived elevation changes from 2011-2013. The CryoSat-2 elevations and elevation changes where interpolated to the ATM-data using bilinear interpolation.

CryoSat-2 generated DEM height compared to ATM height point data.

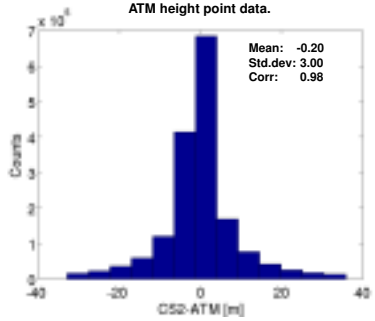

CryoSat-2 gridded dH/dt compared to ATM dH/dt point data.

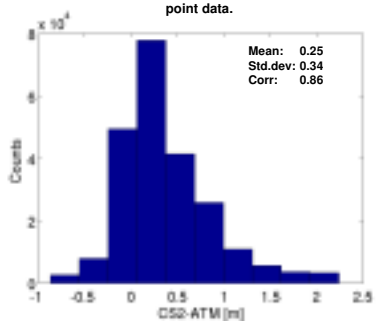

Comparison

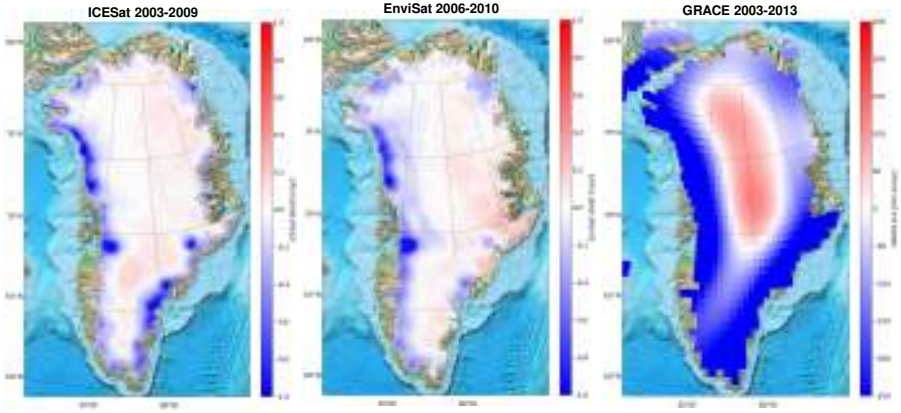

[1]DTU Space, National Space Institute, Technical University of Denmark, Elektrovej Bygning 327, 2800 Kgs. Lyngby, Denmark, Email: jnils@space.dtu.dk
[2]Ohio State University, Columbus, Ohio, United States of America

DTU Space
National Space Institute
Technical University of Denmark

Elektrovej 327
DK-2800 Kgs. Lyngby

Tel +45 4525 9500
Fax +45 4525 9575

http://www.space.dtu.dk